NASA TECHNICAL NOTE

NASA TN D-5615

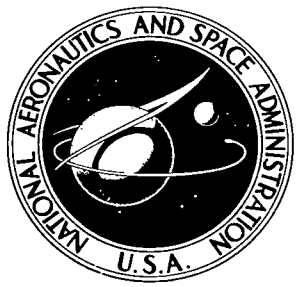

NASA TN D-5615

RADIO BLACKOUT ALLEVIATION AND PLASMA DIAGNOSTIC RESULTS FROM A 25 000 FOOT PER SECOND BLUNT-BODY REENTRY

by Norman D. Akey and Aubrey E. Cross

Langley Research Center
Langley Station, Hampton, Va.

NATIONAL AERONAUTICS AND SPACE ADMINISTRATION • WASHINGTON, D. C. • FEBRUARY 1970

1. Report No. NASA TN D-5615	2. Government Accession No.	3. Recipient's Catalog No.
4. Title and Subtitle RADIO BLACKOUT ALLEVIATION AND PLASMA DIAGNOSTIC RESULTS FROM A 25 000 FOOT PER SECOND BLUNT-BODY REENTRY		5. Report Date February 1970 6. Performing Organization Code
7. Author(s) Norman D. Akey and Aubrey E. Cross		8. Performing Organization Report No. L-6866 10. Work Unit No. 730-01-00-01-23
9. Performing Organization Name and Address NASA Langley Research Center Hampton, Va. 23365		11. Contract or Grant No. 13. Type of Report and Period Covered Technical Note
12. Sponsoring Agency Name and Address National Aeronautics and Space Administration Washington, D.C. 20546		14. Sponsoring Agency Code

15. Supplementary Notes

Appendix A by Thomas G. Campbell
Appendix B by Fred B. Beck
Appendix C by W. Linwood Jones, Jr.

16. Abstract

On October 19, 1967, RAM C-I was launched from the NASA Wallops Station aboard a four-stage Scout vehicle. The threefold purpose of the flight experiment was to determine the effectiveness of water injection as a communications blackout suppressant on a spacecraft entering the earth's atmosphere at earth-orbital velocities of about 25 000 ft/sec (7620 m/sec), to test the effectiveness of an X-band high-frequency telemetry system in reducing blackout time, and to make electrostatic probe measurements of flow-field characteristics. Water injection reduced the radio-frequency signal attenuation caused by the plasma surrounding the RAM C-I at altitudes between 260 000 and 135 000 ft (79.2 and 41.1 km). The electrostatic probe measurements were made continuously during the portion of the flight from 290 000 to 200 000 ft (88.4 to 61.0 km) and were used to infer electron density distributions in the plasma sheath. The X-band (9210 MHz) telemetry signal was received down to 144 000 ft (43.9 km), approximately 120 000 ft (36.6 km) after VHF blackout. Other transmission frequencies were 225.7 MHz, 259.7 MHz, and 5700 MHz.

17. Key Words Suggested by Author(s) Reentry communications Plasma diagnostics Blackout alleviation Material injection Electrostatic (Langmuir) probes	18. Distribution Statement Unclassified – Unlimited

19. Security Classif. (of this report) Unclassified	20. Security Classif. (of this page) Unclassified	21. No. of Pages 93	22. Price* $3.00

*For sale by the Clearinghouse for Federal Scientific and Technical Information
Springfield, Virginia 22151

CONTENTS

RADIO BLACKOUT ALLEVIATION AND PLASMA DIAGNOSTIC RESULTS FROM A 25 000 FOOT PER SECOND BLUNT-BODY REENTRY

By Norman D. Akey and Aubrey E. Cross
Langley Research Center

SUMMARY

On October 19, 1967, RAM C-I was launched from the NASA Wallops Station aboard a four-stage Scout vehicle. The threefold purpose of the flight experiment was to determine the effectiveness of water injection as a communications blackout suppressant on a spacecraft entering the earth's atmosphere at earth-orbital velocities of about 25 000 ft/sec (7620 m/sec), to test the effectiveness of an X-band high-frequency telemetry system in reducing blackout time, and to make electrostatic probe measurements of flow-field characteristics. Water injection reduced the radio-frequency signal attenuation caused by the plasma surrounding the RAM C-I at altitudes between 260 000 and 135 000 ft (79.2 and 41.1 km). The electrostatic probe measurements were made continuously during the portion of the flight from 290 000 to 200 000 ft (88.4 to 61.0 km) and were used to infer electron density distributions in the plasma sheath. The X-band (9210 MHz) telemetry signal was received down to 144 000 ft (43.9 km), approximately 120 000 ft (36.6 km) after VHF blackout. Other transmission frequencies were 225.7 MHz, 259.7 MHz, and 5700 MHz.

INTRODUCTION

Disruption of communications with a spacecraft traveling at a high velocity through the earth's atmosphere is due to the plasma (ionized gas) formed about the spacecraft by aerodynamic heating. The dominant chemical kinetic processes in the plasma play an important role in determining the degree of electromagnetic interference and vary as the velocity and bluntness of the reentering spacecraft. For a given body bluntness, three velocity regimes can be considered (ref. 1). The low-velocity regime centers about 18 000 ft/sec (5486 m/sec) and singular molecular ionization is the important chemical kinetic factor. The medium-velocity region centers about 26 000 ft/sec (7925 m/sec) and atomic ionization and charge transfer processes become important. The high-velocity

regime is above 30 000 ft/sec (9144 m/sec) and the atomic ionization, photoionization, and electron-impact ionization processes and multiple-charged ions are all important.

In the Langley Research Center Project RAM (Radio Attenuation Measurements), plasma characteristics and radio interference alleviation techniques have been studied and tested in both ground facilities and flights. Results are documented in part in references 1 to 17; other pertinent information is given in references 18 to 24. Previous RAM flight experiments have included water injection during reentry at 18 000 ft/sec (5486 m/sec) from a hemisphere-cone body (ref. 11) and at 24 000 ft/sec (7315 m/sec) from a Gemini spacecraft (ref. 17).

RAM C-I, a hemisphere-cone probe with a 6-in. (15.24 cm) nose radius, was launched from the NASA Wallops Station on October 19, 1967, aboard a Scout vehicle and had a nominal reentry velocity of 25 000 ft/sec (7620 m/sec). During payload reentry, two techniques for alleviating blackout were tested (water injection and X-band signal transmission) and electrical characteristics of the plasma sheath were measured.

Water was injected into the flow field from the spacecraft as a means of reducing radio signal attenuation during reentry. Water injection into the flow field utilizes the water droplets as recombination surfaces for positive ions and free electrons. Theoretical and experimental background for both the mechanism and mechanics of liquid injection may be found in references 10 to 14.

An X-band (9210 MHz) telemetry system was used as a means of reducing the radio blackout period. This telemetry system transmitted a microwave carrier which was above the critical plasma frequency during a large portion of the reentry. A discussion of this technique may be found in references 1 and 5.

Plasma positive ion density was measured as a function of standoff distance from the spacecraft surface at a fixed body station by using an electrostatic probe fin. From these measurements, electron density concentrations in the flow field of the spacecraft were inferred.

The effectiveness of the two blackout alleviation techniques and the plasma-sheath diagnostic measurements are presented in this report. Also included are a description of the RAM C-I VHF telemetry antenna systems in appendix A by Thomas G. Campbell, a discussion of the design and development of C-band and X-band antennas in appendix B by Fred B. Beck, and an interpretation of RAM C-I electrostatic probe data in appendix C by W. Linwood Jones, Jr.

DESCRIPTION OF PAYLOAD

General Characteristics

A four-stage solid-fuel Scout (Scout S-159) was the launch vehicle for the RAM C-I. (See fig. 1.) The payload and the fourth stage were spin stabilized at three revolutions per second just prior to fourth-stage ignition. A protective heat shield for the payload and fourth-stage motor was ejected during coasting flight between second-stage burnout and third-stage ignition.

The payload configuration (fig. 2) had a 6-in.-radius (15.24 cm) hemispherical nose followed by a 9° half-angle cone. The overall length of the payload was 51 in. (129.5 cm). The cone base diameter was 24 in. (61.0 cm) and the weight at launch was 267 lb (121.1 kg). The heat protection material covering the hemisphere nose was a charring ablator. The material was selected (ref. 25) in order that the integrity of the water injection nozzles, drilled through the material, would be maintained during ablation. The afterbody was covered with teflon.

The two major systems onboard the RAM C-I were the experiment system and the instrumentation system. The experiment system consisted of (1) water injection mechanism, (2) X-band telemetry, and (3) electrostatic probes. The instrumentation system included various sensors, payload performance instruments, a tape recorder, and two VHF telemeters. Figure 2, a cutaway drawing of the payload, shows the relative location of the various components. All instrumentation performance was nominal and is not discussed in this report.

A perspective sketch of the RAM C-I and coordinates of the important functional parts are given in table I. Indicated in the sketch are the respective locations (three) of the water injection nozzles, the VHF and X-band telemetry antennas, the C-band beacon antenna, and the electrostatic and thermocouple probe fins. One water injection site was in the stagnation region and the other two were located diametrically at the points of tangency between the hemisphere and cone section. Two 259.7-MHz VHF cavity-backed slot antennas, for the real-time telemetry system, were also located diametrically, aft of and in line with the water injection sites. The real-time 259.7-MHz VHF telemetry link used a 5-W FM transmitter. A 225.7-MHz VHF antenna, also excited by a 5-W FM transmitter, was just forward of the payload base. The 225.7-MHz system was also used as a telemetry link transmitting the same data as the 259.7-MHz system but with a 45-sec delay. This delayed telemetry was accomplished by a continuous loop tape recorder in the payload which stored real-time information for 45 sec before transmittal and supplied the data after the payload emerged from blackout. A detailed description of the two VHF telemetry antenna systems is given in appendix A.

The 9210-MHz X-band telemetry antenna system was a four-horn array. The X-band horns were positioned at 90° intervals on the periphery of the payload with a 30° offset from the slot antennas. The 5700-MHz C-band beacon antenna was located behind the 225.7-MHz VHF antenna. The C-band and X-band antenna systems are discussed in appendix B. The two retractable fins were diametrically positioned at the aft end of the payload and in line with the water injection sites. One fin contained eight electrostatic probes for measuring the plasma ion current. The other fin was equipped with three thermocouples for correlation of the fin leading-edge heating. Both fins were retracted at 176 000 ft (53.6 km) during reentry for payload stability considerations. Detailed descriptions of the two onboard blackout alleviation systems and the flow-field diagnostic experiment are presented in the following sections.

Water Injection System

The water injection system was designed to provide a programed variation of flow rates and jet velocities in order to place specific amounts of water throughout part of the radio-frequency (RF) attenuating layer of the flow field. The experiment was designed so that flow rate levels for the water injection system would provide for electron density reductions in the RF attenuating layer of the flow field, which varies with altitude.

The water injection system is shown in block diagram form in figure 3(a). It consists basically of a gas pressurizing system, a water reservoir, 11 solenoid valves, and an electronic programer. Prior to separation of the payload from the fourth stage, the system conditions were as follows: the nitrogen supply bottle was sealed off from the pressure reservoir by the supply valves; the water reservoir, which held 4.2 lb (1.905 kg) of water, was sealed from the gas side by the neoprene bladder and from the other side by the water dump valve; the water lines to the solenoid valves were empty and all of the valves were closed. When the payload had descended to an altitude of 410 000 ft (125.0 km), a command signal from Bermuda initiated the electronic programer action. Ten sec later two solenoid valves were opened to allow the water supply lines to the solenoid valves to be bled down to the ambient pressure, which was essentially vacuum. The valves were then closed and the water dump valve was opened to allow the water to fill the lines. The water pressure at that time was 2 psia (13.79 kN/m^2) due to the initial condition in the pressure reservoir. The cycling of the solenoid valves was then begun with the sequencing shown in figure 3(b). As shown, a cycle of the valves consisted of 7 pulses and the cycle was repetitive every 4 sec. The valve-on times were 230 msec and the valves were opened at 0.5-sec intervals. Valves 5, 6, and 7 (at stagnation injection site) were consecutively opened and allowed increasingly larger amounts of water to be injected into the flow field. Next, the pairs of valves from the side locations (valves 1, 2, 3, and 4) were consecutively opened and also provided increasing flow rates.

Figure 4 shows the orifice configurations for the various flow rates. All orifices were 0.018 in. (0.4577 mm) in diameter and the increase in flow rate was accomplished by increasing the number of orifices used. To increase both the rate of flow and the penetration of the injection into the flow field as a function of decreasing altitude, the two pressure supply valves were opened by the programer, one at 250 000 ft (76.2 km) and the other at 176 000 ft (53.6 km). The gas from the nitrogen supply bottle was thus fed through the valve orifices at a predetermined rate and thereby the head pressure on the water was increased as the payload descended. The resultant flow rates as obtained from flight data are given in table II, with the altitude noted for the start of each pulse. (Cycle 1 had no flow due to a slow fill rate in the lines.)

X-Band Telemetry System

A block diagram of the X-band telemetry system which was used to demonstrate the effectiveness of higher transmission frequencies in reducing blackout time, is shown in figure 5. All input data transmitted by this system were also transmitted by the VHF telemetry links. Each of the 60 input channels was commutated 15 times per second by a solid-state electronic commutator-encoder. The outputs from the encoder were pulse position modulated (PPM) to the X-band transmitter and pulse duration modulated (PDM) to the VHF transmitter. The X-band transmitter had a peak power output of 500 W with a pulse width of 1.0 μsec and a pulse repetition frequency of 1800 pulses per second. The power was divided and transmitted through a four-horn antenna array (described in appendix B) providing a symmetrical radiation pattern about the payload. Since the payload was spin stabilized during reentry, a symmetrical pattern would allow signal-strength interpretations of RF attenuation effects independent of vehicle spin motions.

Electrostatic Probe Experiment

The electrostatic probe experiment was designed to measure the positive ion density profiles through and beyond the flow-field boundary layer of the plasma surrounding the spacecraft as a function of distance normal to the payload surface. The leading-edge dimension of the probe was designed to be free molecular for altitudes above 180 000 ft (54.9 km). The probe body was designed to extend through the peak or maximum plasma density region of the flow field so that an experimental determination of peak density as a function of altitude could be made. Measurements were made at a fixed body station on the aft portion of the spacecraft.

The exterior physical configuration of the electrostatic probe fin, a sectional view of the leading edge, and standoff dimensions of the ion collectors are given in figure 6(a). The probe was essentially a rake consisting of eight individual sensors which were made from iridium strips. The sensors, or ion collectors, extended 0.010 in. (0.254 mm)

beyond the wedge-shaped leading edge. Larger iridium pieces mounted parallel to the leading edge on both sides of the wedge functioned as electron collectors. Iridium was used because of its high melting temperature, high electronic work function, and negligible oxidation property. The 0.010-in. radius of the beryllium oxide leading edge was followed by a 60° wedge, and the entire probe configuration was swept back at a 45° angle with respect to the payload surface.

Each ion collector was electrically insulated with beryllium oxide, which was used because of its high temperature insulation properties. The two electron collectors on either side of the wedge were electrically common. Referenced to the electron collectors, a fixed bias of -5.0 V was applied to all ion electrodes so that in the presence of a plasma the positive ions were collected. The resultant ion current on each of the eight probes was commutator sampled and then conditioned by a logarithmic amplifier for telemetering. The logarithmic amplifier had a current range from 10^{-7} A to 10^{-3} A; this current range corresponded to an electron density range from 10^{8} electrons/cm^3 to 10^{12} electrons/cm^3.

When immersed in a flowing plasma, the collectors appear to the charged particles to be 0.010-in.-diameter (0.254 mm) cylindrical wires due to the directed ion velocity; therefore, a modified cylindrical probe theory can be used in the interpretation (ref. 15). The basic theory and a sample calculation of the data reduction procedure for interpretation of the electrostatic probe data are given in appendix C. Although only positive ions are measured by the electrostatic probes, electron densities can be inferred because equal distribution of the electrons and positive ions is assumed.

Thermocouple Probe

The purpose of the thermocouple probe was to determine the altitude at which insulation degradation for the electrostatic probes began. The thermocouple probe fin was mounted on the payload diametrically opposite the electrostatic probe fin. Both the thermocouple and electrostatic probes were in line with the water injection sites to insure similar heating environments.

The geometry of the thermocouple probe fin shown in figure 6(b) was the same as that of the electrostatic probe fin. Instead of electrodes, however, three thermocouples were imbedded 0.025 in. (0.635 mm) from the leading edge of the wedge as shown in the sectional view of the probe leading edge. The thermocouples were platinum-platinum 13 percent rhodium and were located 0.787, 1.575, and 2.36 in. (2, 4, and 6 cm) from the payload surface. The useful measurement range of the thermocouples was from 0° F to 3100° F (255° K to 1978° K).

RESULTS AND DISCUSSION

Trajectory and Tracking

RAM C-I was launched from the NASA Wallops Station at 17:33:00 GMT on October 19, 1967, on an azimuth of 109°. The launch vehicle flew a suborbital trajectory and reached an apogee of 750 000 ft (229 km) prior to driving the payload back into the atmosphere at a flight-path angle of -15°. Maximum payload velocity was 25 165 ft/sec (7670 m/sec). Reentry was north of Bermuda, the primary tracking station. Midway through the data period the payload was 100 n. mi. (185.2 km) from the island. The RAM C-I ground track is shown in figure 7.

The variation of altitude and velocity with time for the reentry is shown in figure 8. The indicated events are the command signal from Bermuda which started the programer at 410 000 ft (125.0 km), fourth-stage separation from the payload at 360 000 ft (109.7 km), beginning of water injection at 273 000 ft (83.2 km), retraction of the two probe fins at 176 000 ft (53.6 km), and water cutoff at 110 000 ft (33.5 km). A detailed payload velocity history during reentry from 500 000 ft (152.4 km) down to 20 000 ft (6.10 km) in 5000-ft (1.524 km) altitude increments is given in table III.

Backup tracking was provided by the USNS Twin Falls Victory shown in figure 7. VHF telemetry coverage was provided by Bermuda, the USNS Twin Falls Victory, the USNS Range Recoverer, NASA aircraft 432 and 438, and an Eastern Test Range (ETR) aircraft. The X-band telemetry receiving stations were located at Bermuda.

Continuous trajectory data were obtained at the Bermuda radar installation by the AN/FPS-16 and AN/FPQ-6 radars. Figures 9(a) and 9(b) show portions of the smoothed radar signal-strength data obtained. The FPS-16 radar was in the beacon track mode initially with the FPQ-6 radar operating in the skin track mode. As the payload beacon signal was first attenuated by the reentry plasma at 195 000 ft (59.4 km), the skin track return signal was enhanced. When the FPS-16 radar lost the beacon signal at 180 000 ft (54.9 km), the FPQ-6 radar continued tracking in the skin track mode. The skin return signal remained enhanced until the payload velocity decreased; this decrease caused a reduction of the plasma which, in turn, reduced the skin return signal and allowed the beacon signal to again be received upon emergence from blackout. Detailed C-band beacon track records are given in figure 9(c). A separate study of the tracking radar results has been made and is documented in reference 16.

Signal Blackout

Onset and emergence of signal blackout for the RAM C-I reentry are shown in figure 10. The payload velocity at the onset of blackout was about 25 000 ft/sec (7620 m/sec) for all frequencies. The first signal attenuated was the 259.7 MHz VHF

telemetry from the two slot antennas, followed by the 225.7 MHz VHF signal, the 5700 MHz C-band signal, and the 9210 MHz X-band signal. Table IV gives the altitudes for blackout of the various signal frequencies at the different receiving stations. The altitude at onset of attenuation and the altitude at emergence from blackout are also included.

X-Band Telemetry

The X-band telemetry system provided real-time data for two-thirds of the time period that the VHF telemetry signal was blacked out. The X-band signal did not black out until 144 000 ft (43.9 km) as compared with 260 000 ft (79.2 km) for the VHF signal (fig. 10). The blackout velocity was about the same for both signal frequencies, approximately 25 000 ft/sec (7620 m/sec). These results obtained with the X-band telemetry system show a significant improvement in operational time and altitude range for spacecraft reentering the earth's atmosphere.

Water Injection

The effect of water injection on the two VHF telemetry signals, 225.7 MHz and 259.7 MHz, is shown in figures 11 to 15. The received signal strength in decibels is plotted above the noise level as a function of altitude for the five VHF telemetry stations. Signal-strength recovery during the prime data period can be compared with the water injection rates given in table II. Injection was from 273 000 ft (83.2 km) down to 111 000 ft (33.8 km) for a range of flow rates from 0.01 lb/sec to 1.55 lb/sec (4.54 g/sec to 703 g/sec). The last effect of water injection on VHF signal was noted at an altitude of approximately 150 000 ft (45.7 km). When the experiment was designed, it was expected that the largest water injection flow rate from the side (flow rate 4) would provide recovery throughout the entire altitude range of injection. Experimentally, however, only marginal recovery was observed for VHF signal down to 150 000 ft (45.7 km). At altitudes above 200 000 ft (61.0 km), water effects are relatively good.

The signal-strength records (figs. 11 to 15) have been faired to partially eliminate antenna pattern and payload spin effects, which are not readily known nor easily analyzed. For comparison, an unfaired telemetry record of the signal strength received at Bermuda is shown in figure 14(b). Recovery spikes at the beginning and end of the injection pulses are sometimes quite large. It is not known whether these spikes are due to optimum water penetration at these particular instances which allows maximum free-electron quenching or are due to a disruption of the flow field caused by the injected water stream. A spiking phenomenon was also observed during the water injection experiment on Gemini 3 (ref. 17).

The X-band recovery levels are shown in figure 16 and water injection effects were observed down to 129 000 ft (39.3 km). The effect of water injection was observed in the radar cross section of the payload and wake as a variation of intensity of the signal received by the skin track C-band radar. These data are evaluated in reference 16.

VHF antenna transmission characteristics are shown in figures 17(a) and (b). Figure 17(a) shows the effect of water injection on the forward and reflected power levels for the 259.7-MHz VHF system, a sharply tuned narrow-bandwidth slot antenna. During injection the reflected power is reduced and the forward power is increased; this indicates that the effects of the plasma on electromagnetic absorption and reflection are being reduced during the presence of water in the flow field. Figure 17(b) shows the forward and reflected power levels for the 225.7-MHz system, a broadly tuned wide-bandwidth ring antenna. Figure 17(c) shows forward and reflected power levels for the X-band system. An analysis of these power measurements (VSWR) will contribute to an improved understanding of the flow field.

The electrostatic probe data presented in the next section indicate that the attenuating layer of the flow field surrounding RAM C-I extended beyond the ends of the probes. Thus, it is likely that the water was not distributed far enough into the flow field to reduce the outer levels of the electron density so that the propagation of the signal through the flow field was possible.

Electrostatic Probe

Approximately 1 sec, corresponding to an altitude change of from 237 000 ft (72.2 km) to 231 000 ft (70.4 km), of the electrostatic probe data is shown in figure 18 where the collected ion current is plotted as a function of altitude. The eight ion collectors are sampled consecutively with one sweep of the eight collectors requiring about 0.026 sec. Thus, an ion distribution profile is obtained in 26 msec, which represents about 8 percent of one revolution of the payload. An in-flight calibration of the electronic system occurs after each three sweeps. The calibration levels are indicated in the figure (100%, 75%, 50%, 25%, 0% of full scale) and correspond to the scale markings on the ordinate axis.

The effects on the current distributions of flow rates 3 and 4 of water injection cycle 3 are also shown in figure 18. Flow rate 3 reduces the ion currents by approximately 1 decade, whereas the larger flow rate 4 reduces the ion currents by approximately 2 decades. The currents returned to their preinjection values very quickly when injection was stopped.

A history of electron density computed from measurements of probes 1, 5, and 8 is presented in figure 19. From a comparison of the curve slopes an insight into electron-density distribution rates may be gained. A gradual increase in electron density for

probes 1 and 5 is noted from 280 000 ft to 267 000 ft (85.3 km to 81.4 km), with a greater increase in density from 267 000 ft to 257 000 ft (81.4 km to 78.3 km). The buildup of electrons between 267 000 ft and 257 000 ft corresponds to the beginning of complete signal loss from the 259.7-MHz forward VHF slot antennas and to the initial attenuation of the 225.7-MHz aft VHF ring antenna. Critical electron densities for the 259.7- and 225.7-MHz frequencies are 8.2×10^8 and 6.3×10^8 electrons/cm^3, respectively. Below 257 000 ft, electron density curves derived from all probes indicate only a gradual increase in magnitude. However, from 280 000 ft to 257 000 ft (85.3 km to 78.3 km), probe 8 curve shows an almost constant rate of increase in density and has a greater slope than those for probes 1 and 5; this indicates that peak or maximum electron density moves in an outboard to inboard direction since the standoff distance from the payload surface of probes 1, 5, and 8 is increasing as shown in figure 6(a).

Water injection and spacecraft motions, such as yawing, pitching, spinning, and coning, complicate the analysis of the electron density distribution rates. Figure 19 indicates that the probe density measurements include payload motion effects as evidenced by the null occurring during a period of no injection between cycle 2 and cycle 3 of the water injection (255 000 ft (77.7 km)). This null is certainly not attributable to injection. Likewise, the nulls occurring during injection cycle 2 are most likely due to payload motion effects. These effects are shown by the difference between the deep null during flow rate 2 and a mild depression during flow rate 3, although flow rate 3 is the larger of the two. A 3-rps oscillatory variation of electron density, which is not readily apparent from the figure, is definitely present in the measured density fluctuations. This variation is most likely due to the fact that the payload is at an angle of attack (unsymmetrical flow field about payload) while spinning at a 3-rps rate through the flow field. The probes, which are fixed on the payload, are therefore measuring a varying electron density at the spin rate because of the asymmetry.

During injection cycle 3, the sequential increase in flow rates are readily seen as corresponding decreases in electron density. Distribution profiles during the side injection portion of cycle 3 are shown in figure 20. The curve labeled "No flow" represents the average distribution during the no-injection periods of injection cycle 3. The data points for each profile represent instantaneous interpolations of electron density from plots such as those in figure 19. If a calculation of the attenuation change at VHF is made by applying plane-wave—homogeneous-plasma slab theory in increments to the electron density profile changes in figure 20 for flow rates 2, 3, and 4, there is good agreement between the resultant integral attenuation change and the observed attenuation change of figures 11 to 15.

Effects on electron density during one stagnation sequence of water injection occurring over a 1947-ft (593 m) altitude range is shown in figure 21. Almost a 2-decade

change in electron density due to water injection is observed. Injection began at 226 690 ft (69.1 km) and actually stopped at 225 250 ft (68.7 km).

A family of electron density profiles during no injection over an altitude range from 280 000 to 185 000 ft (85.3 to 56.4 km) is shown in figure 22. The profile at an altitude of 280 000 ft corresponds to the beginning of the electrostatic probe data period. (At altitudes of 195 000 ft (59.4 km) and 185 000 ft (56.4 km), the outermost collectors have saturated the measuring system.) The profiles inferred from the electrostatic probe measurements indicate a much thicker boundary layer than that used as the design criterion. From the general slope of the profiles, the outer edge of the boundary layer appears to be beyond a standoff distance of 7 cm.

Thermocouple Probe

A knowledge of the aerodynamic heating on the probe is necessary for valid probe current interpretation. Thermocouple probe data for the RAM C-I are presented in figure 23. Data from thermocouples 7, 8, and 9 show a small initial increase in heating. Thereafter data from thermocouple 9 indicate a sharp rise in heating commencing at about 230 000 ft (70.1 km) and the heating rate of thermocouple 8 changes abruptly at about 204 000 ft (62.2 km). Electrostatic probe data are considered to be useful only for comparative purposes and not for absolute values once the local probe temperature exceeds 1000° F (811° K) due to probable thermal degradation of the beryllium oxide insulator. Finally, at 189 500 ft (57.8 km), data from thermocouple 7 also indicate an abrupt rise in heating rate. Effects of water injection can also be seen in figure 23, particularly for altitudes below 210 000 ft (64.0 km).

CONCLUDING REMARKS

A reentry flight experiment has been conducted with the RAM C-I at about 25 000 ft/sec (7620 m/sec) to determine the reduction in radio-frequency signal attenuation due to injection of water into the plasma sheath surrounding the RAM C-I and to measure plasma properties by using electrostatic probes. From the data obtained, the following remarks can be made:

1. Water injection into the plasma surrounding the payload reduced the attenuation of signals radiated from the RAM C-I at frequencies of 225.7 MHz, 259.7 MHz, 5700 MHz, and 9210 MHz.

   Effects of water injection were observed on signal-strength measurements down to 150 000 ft (45.7 km) for the VHF frequencies and to 130 000 ft (39.6 km) for the X-band frequency.

Signal recovery levels due to water injection did not meet the design estimates apparently because the attenuating portion of the flow field was thicker than expected, as evidenced by the electrostatic probe measurements at altitudes above 200 000 ft (61.0 km).

Both VHF and X-band VSWR measurements show plasma effects on the antennas, and a change in the effects during water injection is observed.

2. The X-band telemetry system provided real-time data during two-thirds of the time period that the VHF signal was blacked out at a reentry velocity of about 25 000 ft/sec (7620 m/sec) and thereby confirmed the worth of high-frequency transmission as a means of reducing the time interval of communications blackout.

The X-band signal was received to a 115 000-ft (35.0 km) lower altitude than were the VHF signals. The blackout altitudes were 260 000 ft (79.2 km) for VHF and 144 000 ft (43.9 km) for X-band frequency.

3. Electrostatic probes were effective in measuring the plasma properties.

Preliminary data reduction indicated that the region of high electron density in the flow field was thicker than expected.

During the period of valid electrostatic probe measurements, good agreement was obtained between the measured levels of electron density and the VHF signal attenuation data, both with and without water injections.

The effects of vehicular motion on the plasma density levels were also observed.

Langley Research Center,
National Aeronautics and Space Administration,
Langley Station, Hampton, Va., October 28, 1969.

TABLE I.- POSITION OF FUNCTIONAL PARTS ON THE RAM C-I CONFIGURATION

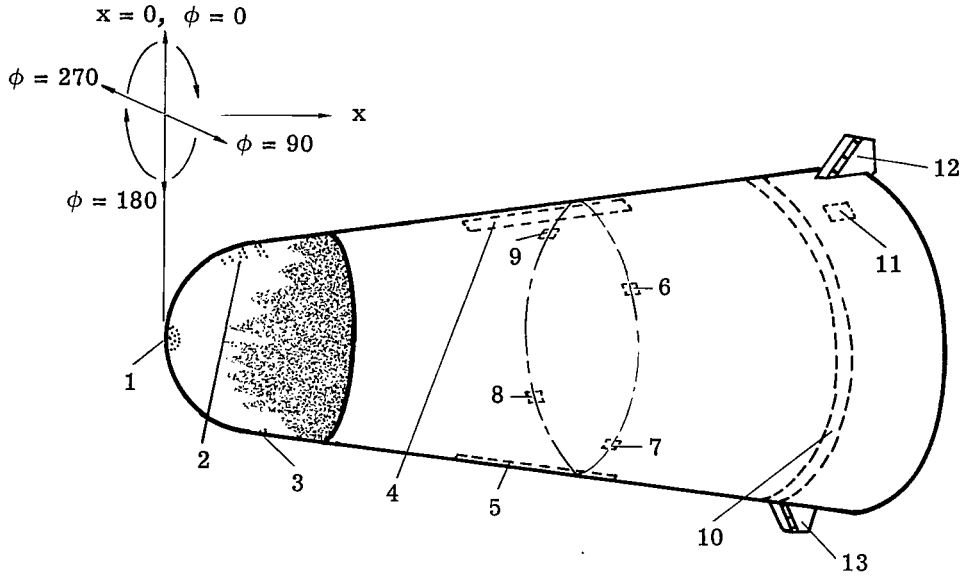

Number	Part Function	x, in.	x, (cm)	ϕ, deg (a)	x/D (b)
	Water injection nozzle:				
1	Stagnation	0	(0)	---	0
2	Lateral	6.0	(15.2)	0	.48
3	Lateral	6.0	(15.2)	180	.48
	Antenna:				
4	VHF slot (259.7 MHz)	29.6	(75.2)	0	2.36
5	VHF slot (259.7 MHz)	29.6	(75.2)	180	2.36
6	X-band horn (9210 MHz)	32.6	(82.8)	60	2.60
7	X-band horn (9210 MHz)	32.6	(82.8)	150	2.60
8	X-band horn (9210 MHz)	32.6	(82.8)	240	2.60
9	X-band horn (9210 MHz)	32.6	(82.8)	330	2.60
10	VHF ring (225.7 MHz)	43.0	(109.2)	---	3.42
11	C-band horn (5700 MHz)	46.6	(118.4)	30	3.71
	Probe:				
12	Electrostatic	48.6	(123.4)	0	3.87
13	Thermocouple	48.6	(123.4)	180	3.87

[a]Center-line location of parts.

[b]Nose diameter D is 12.56 in. (31.90 cm).

TABLE II.- RAM C-I WATER INJECTION FLOW RATES

Cycle	Valve for –		Flow rate		Altitude	
	Stagnation injection	Side injection	lb/sec	kg/sec	ft	km
1	5		0	0		
	6		0	0		
	7		0	0		
		1	0	0		
		2	0	0		
		3	0	0		
		4	0	0		
2	5		0	0	278 908	85.0
	6		0	0	275 639	84.0
	7		.03	.014	273 027	83.2
		1	.01	.004	269 115	82.0
		2	.04	.018	265 866	81.0
		3	.10	.045	262 616	80.0
		4	.15	.068	259 363	79.0
3	5		0.02	0.009	252 861	77.1
	6		.07	.032	249 598	76.1
	7		.14	.064	246 328	75.1
		1	.06	.027	243 048	74.1
		2	.14	.064	239 771	73.1
		3	.40	.181	236 486	72.1
		4	.66	.299	233 205	71.1
4	5		0.04	0.018	226 690	69.1
	6		.12	.054	223 442	68.1
	7		.24	.109	220 185	67.1
		1	.08	.036	216 915	66.1
		2	.21	.095	213 635	65.1
		3	.55	.249	210 348	64.1
		4	.89	.404	207 054	63.1
5	5		0.05	0.023	200 490	61.1
	6		.15	.068	197 236	60.1
	7		.28	.127	193 982	59.1
		1	.10	.045	190 724	58.1
		2	.24	.109	187 462	57.1
		3	.65	.295	184 202	56.1
		4	1.01	.458	180 943	55.2
6	5		0.06	0.027	174 451	53.2
	6		.18	.082	171 212	52.2
	7		.36	.163	167 968	51.2
		1	.13	.059	164 722	50.2
		2	.32	.145	161 466	49.2
		3	.90	.408	158 199	48.2
		4	1.42	.644	154 937	47.2
7	5		0.07	0.032	148 484	45.2
	6		.23	.104	145 267	44.3
	7		.43	.195	142 058	43.3
		1	.15	.068	138 864	42.3
		2	.35	.159	135 684	41.4
		3	.98	.444	132 511	40.4
		4	1.55	.703	129 532	39.5
8	5		0.08	0.036	123 137	37.5
	6		.24	.109	120 058	36.6
	7		.43	.195	117 010	35.7
		1	.15	.068	113 987	34.7
		2	.35	.159	110 986	33.8
		3	0	0		
		4	0	0		

TABLE III.- ALTITUDE, VELOCITY, AND TIME OF RAM C-I REENTRY TRAJECTORY

Altitude		Velocity		Time from lift-off, sec
ft	km	ft/sec	m/sec	
500×10^3	152.4	23 004	7012	355.98
495	150.9	23 279	7095	356.83
490	149.4	23 567	7183	357.64
485	147.8	23 875	7277	358.42
480	146.3	24 166	7366	359.19
475	144.8	24 476	7460	359.98
470	143.2	24 696	7527	360.77
465	141.7	24 816	7564	361.57
460	140.2	24 872	7580	362.34
455	138.7	24 866	7579	363.11
450	137.2	24 863	7578	363.87
445	135.6	24 872	7580	364.64
440	134.1	24 892	7587	365.40
435	132.6	24 902	7590	366.18
430	131.1	24 920	7596	366.95
425	129.5	24 926	7597	367.73
420	128.0	24 916	7594	368.49
415	126.5	24 914	7594	369.25
410	125.0	24 924	7597	370.00
405	123.4	24 941	7602	370.75
400	121.9	24 965	7609	371.52
395	120.4	24 982	7614	372.30
390	118.9	24 971	7611	373.08
385	117.3	24 967	7610	373.85
380	115.8	24 969	7610	374.61
375	114.3	24 973	7612	375.37
370	112.8	24 986	7616	376.14
365	111.2	24 991	7617	376.92
360	109.7	24 996	7619	377.70
355	108.2	25 008	7622	378.47
350	106.7	25 019	7626	379.23
345	105.2	25 029	7629	379.99
340	103.6	25 024	7627	380.75
335	102.1	25 031	7629	381.52
330	100.6	25 037	7631	382.29
325	99.1	25 026	7628	383.07
320	97.5	25 025	7628	383.86
315	96.0	25 042	7633	384.63
310	94.5	25 065	7640	385.39
305	93.0	25 098	7650	386.14
300	91.4	25 094	7649	386.88
295	89.9	25 087	7646	387.64
290	88.4	25 074	7642	388.40
285	86.9	25 082	7645	389.17
280	85.3	25 095	7649	389.93
275	83.8	25 103	7651	390.70
270	82.3	25 094	7649	391.46
265	80.8	25 096	7649	392.23
260	79.2	25 113	7654	393.00
255×10^3	77.7	25 121	7657	393.77
250	76.2	25 135	7661	394.54
245	74.7	25 164	7670	395.30
240	73.2	25 143	7664	396.07
235	71.6	25 131	7660	396.83
230	70.1	25 139	7662	397.59
225	68.6	25 148	7665	398.36
220	67.0	25 165	7670	399.13
215	65.5	25 156	7668	399.89
210	64.0	25 145	7664	400.65
205	62.5	25 123	7657	401.41
200	61.0	25 102	7651	402.18
195	59.4	25 115	7655	402.94
190	57.9	25 108	7653	403.71
185	56.4	25 076	7643	404.48
180	54.9	25 064	7640	405.25
175	53.3	25 034	7630	406.02
170	51.8	25 009	7623	406.79
165	50.3	24 967	7610	407.56
160	48.8	24 923	7596	408.32
155	47.2	24 829	7568	409.09
150	45.7	24 752	7544	409.86
145	44.2	24 663	7517	410.64
140	42.7	24 532	7477	411.42
135	41.4	24 384	7432	412.20
130	39.6	24 157	7363	412.99
125	38.1	23 882	7279	413.80
120	36.6	23 563	7182	414.61
115	35.0	23 202	7072	415.43
110	33.5	22 763	6938	416.26
105	32.0	22 176	6759	417.12
100	30.5	21 455	6539	418.00
95	29.0	20 446	6232	418.91
90	27.4	19 483	5938	419.87
85	25.9	18 226	5555	420.87
80	24.4	16 697	5089	421.96
75	22.9	14 935	4552	423.16
70	21.3	12 942	3945	424.51
65	19.8	10 624	3238	426.12
60	18.3	8 000	2438	428.22
55	16.8	5 706	1739	430.88
50	15.2	3 441	1049	434.69
45	13.7	1 906	581	440.26
40	12.2	890	271	448.98
35	10.7	721	220	459.34
30	9.1	785	239	467.88
25	7.6	744	227	475.40
20	6.1	907	276	484.45

TABLE IV.- SIGNAL BLACKOUT HISTORY

Station	Signal frequency, MHz	Altitude at beginning of attenuation		Altitude at signal blackout		Altitude at emergence from blackout	
		ft	km	ft	km	ft	km
Bermuda	225.7	267 000	81.4	257 000	78.3	77 000	23.5
	259.7	280 000	85.3	262 000	79.9	74 000	22.6
	5700	195 000	59.4	181 000	55.2	75 000	22.9
	9210	182 000	55.5	144 000	43.9	72 000	21.9
NASA aircraft 438	225.7	274 000	83.5	256 000	78.0	87 000	26.5
	259.7	273 000	83.2	263 000	80.2	79 000	24.1
USNS Range Recoverer	225.7	279 000	85.0	260 000	79.2	78 000	23.8
	259.7	280 000	85.3	267 000	81.4	70 000	21.3

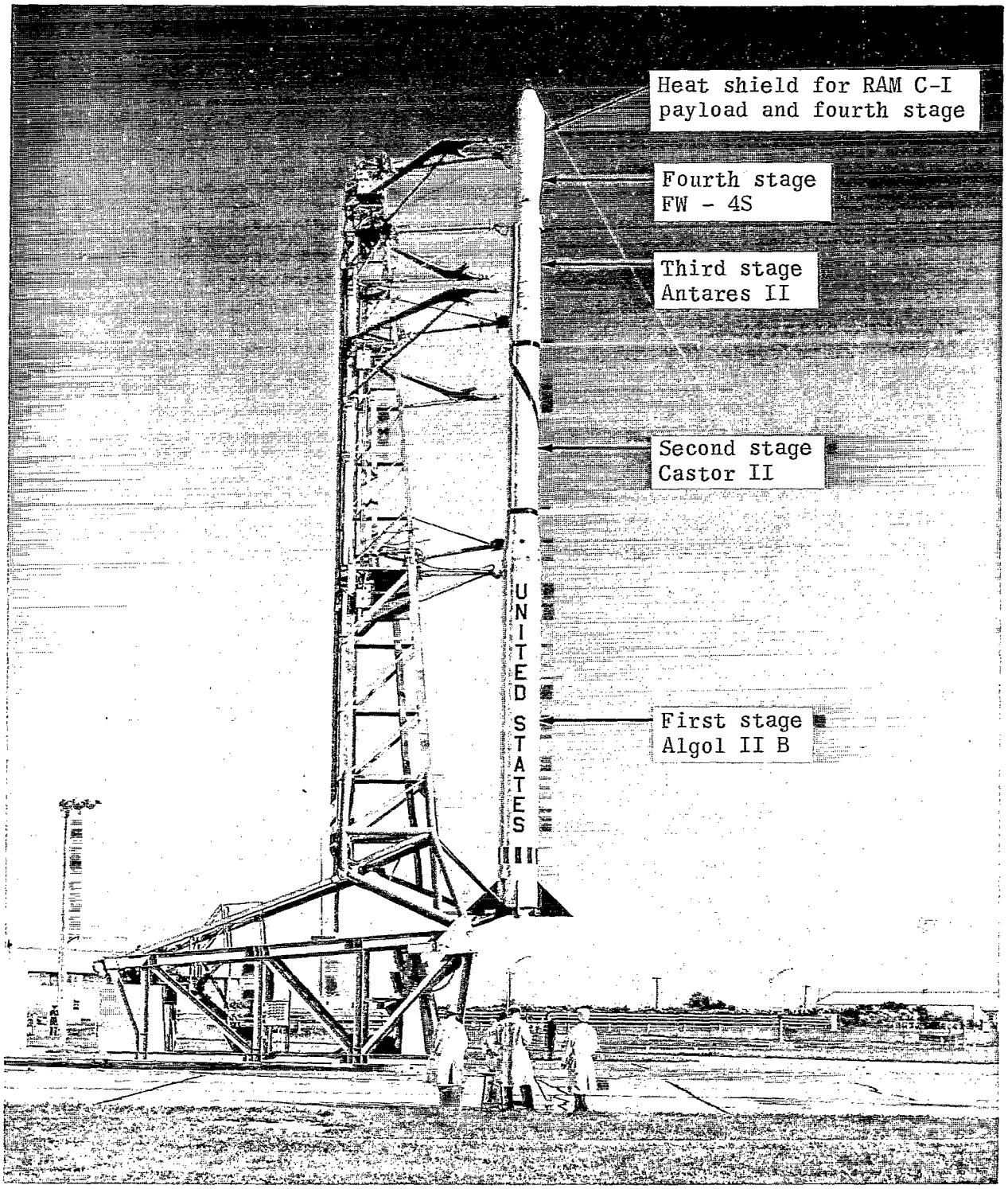

Figure 1.- RAM C-I on launch pad. L-67-220

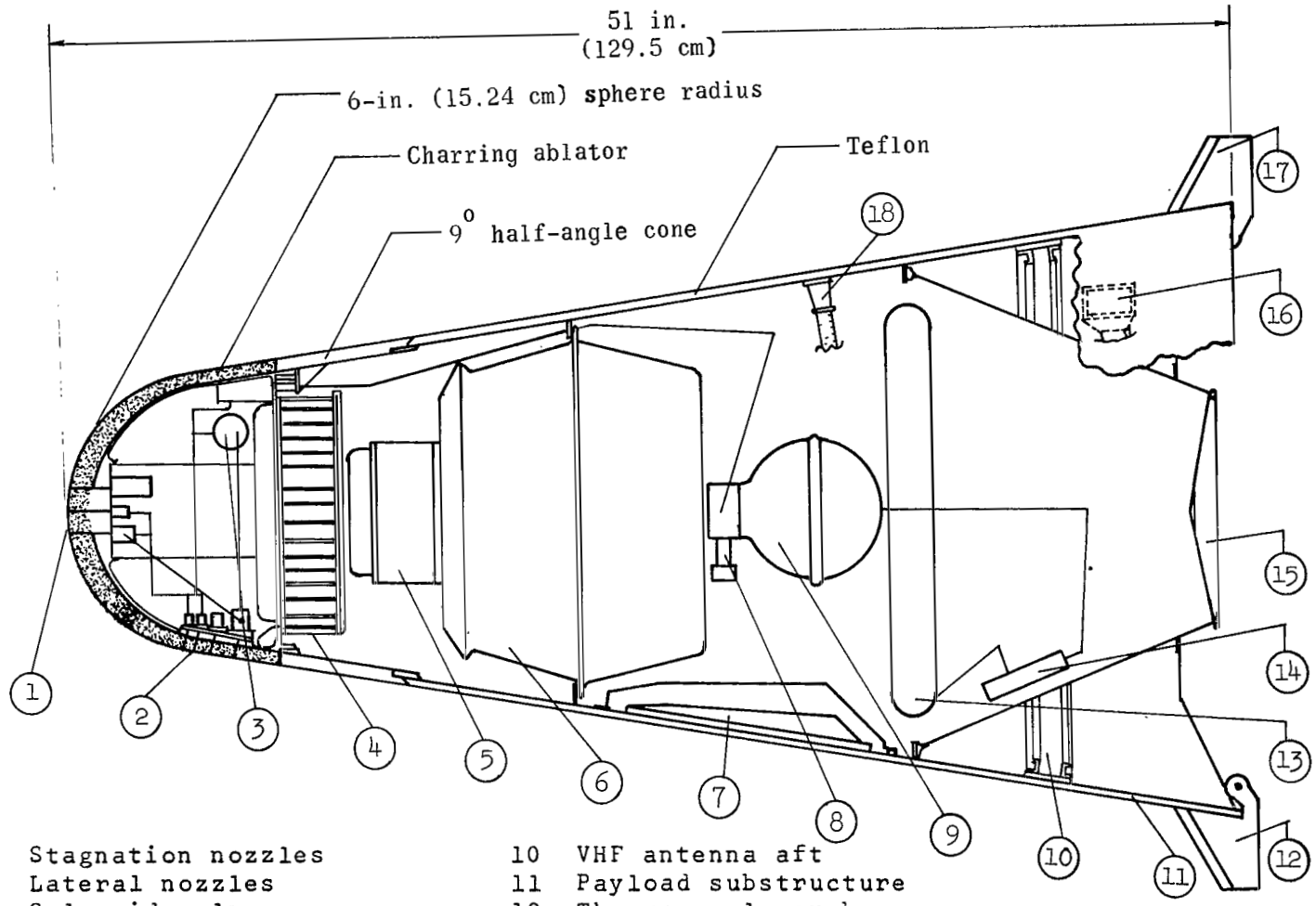

1	Stagnation nozzles	10	VHF antenna aft
2	Lateral nozzles	11	Payload substructure
3	Solenoid valves	12	Thermocouple probe
4	Power supply	13	Nitrogen supply
5	Tape recorder	14	Regulator
6	Telemetry package	15	Payload to Scout transition
7	VHF antenna forward	16	C-band antenna
8	Squib valve	17	Electrostatic probe
9	Material addition storage	18	X-band antenna

Figure 2.- RAM C-I configuration showing experiment and instrumentation systems.

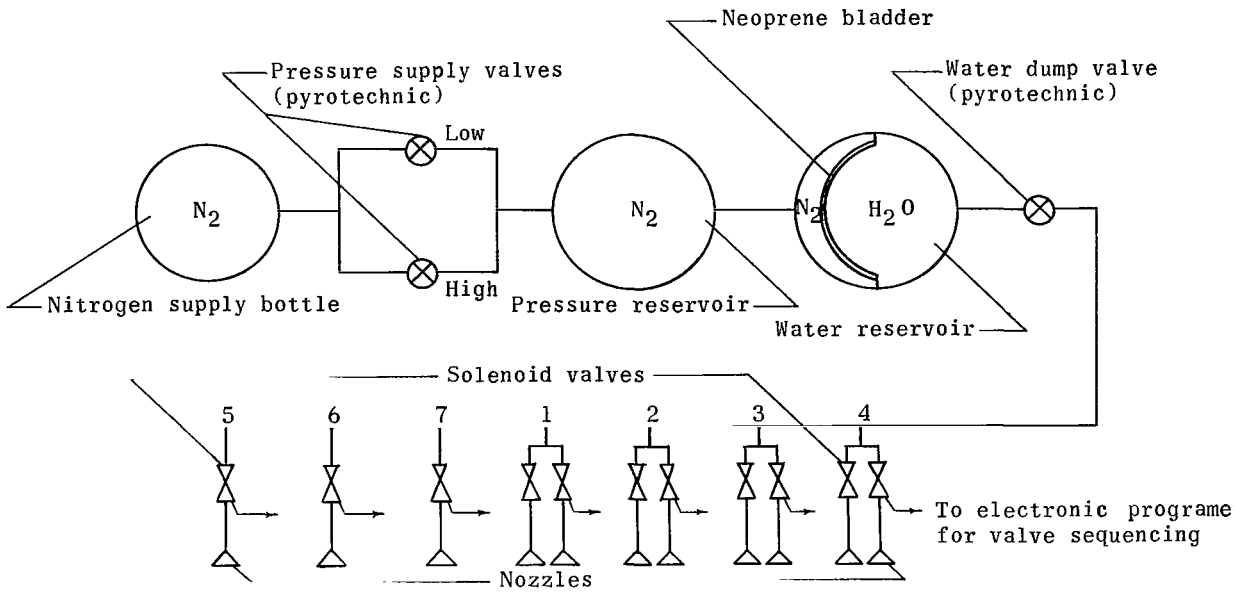

(a) Water injection system.

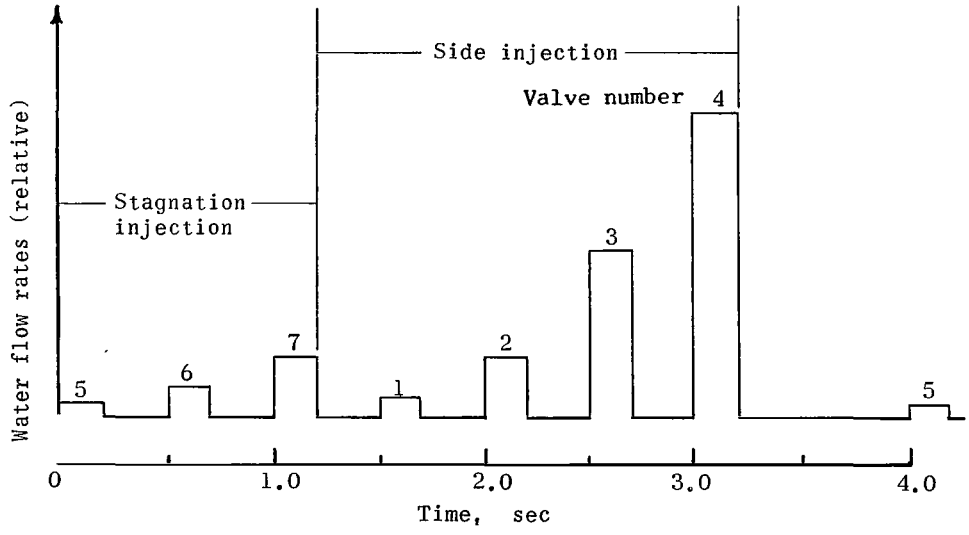

(b) Water injection cycle.

Figure 3.- Block diagram of the RAM C-I water injection system and a typical water injection cycle.

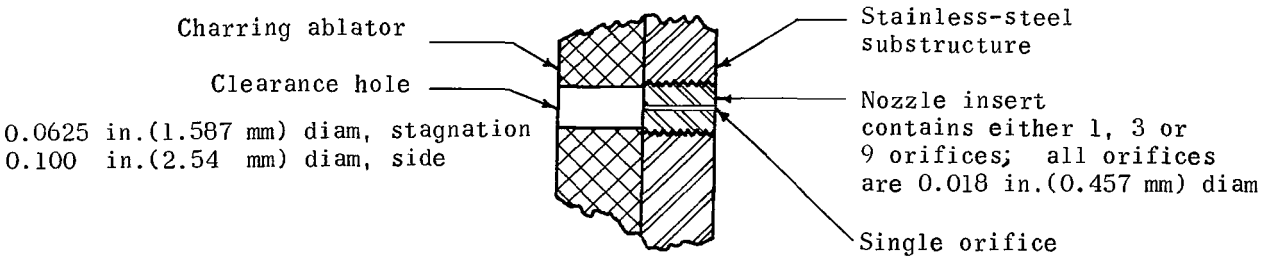

(a) Sectional view of typical nozzle insert with single orifice.

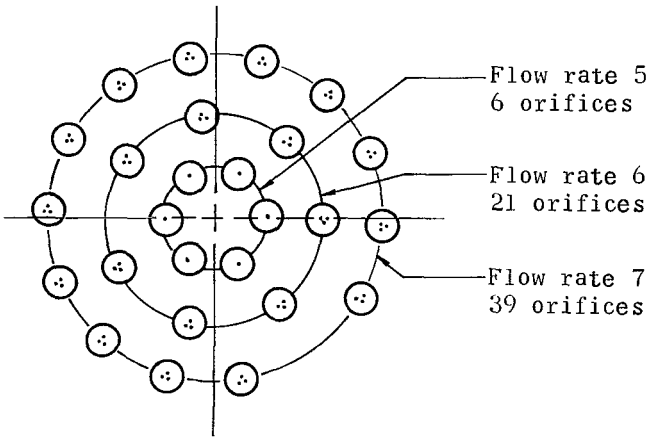

(b) Stagnation injection orifice layout.

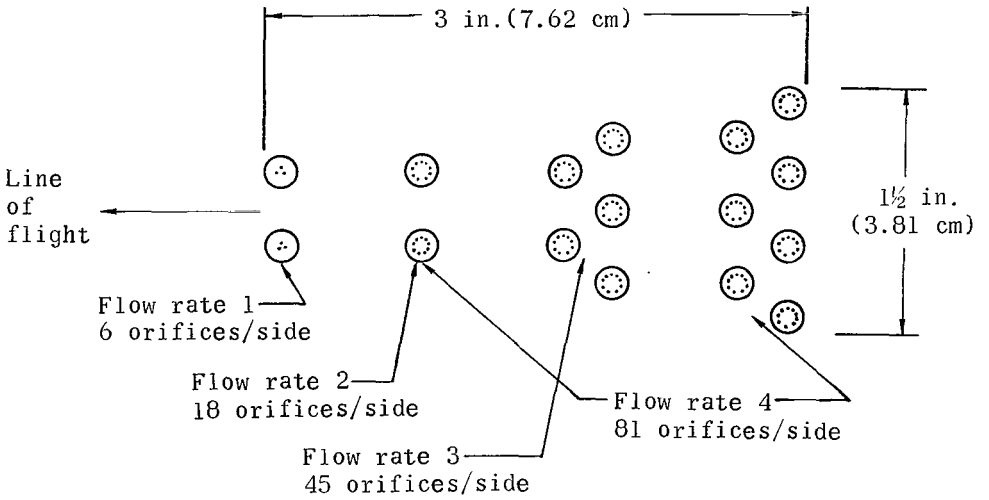

(c) Side injection orifice layout.

Figure 4.- Orifice configurations for the water injection system.

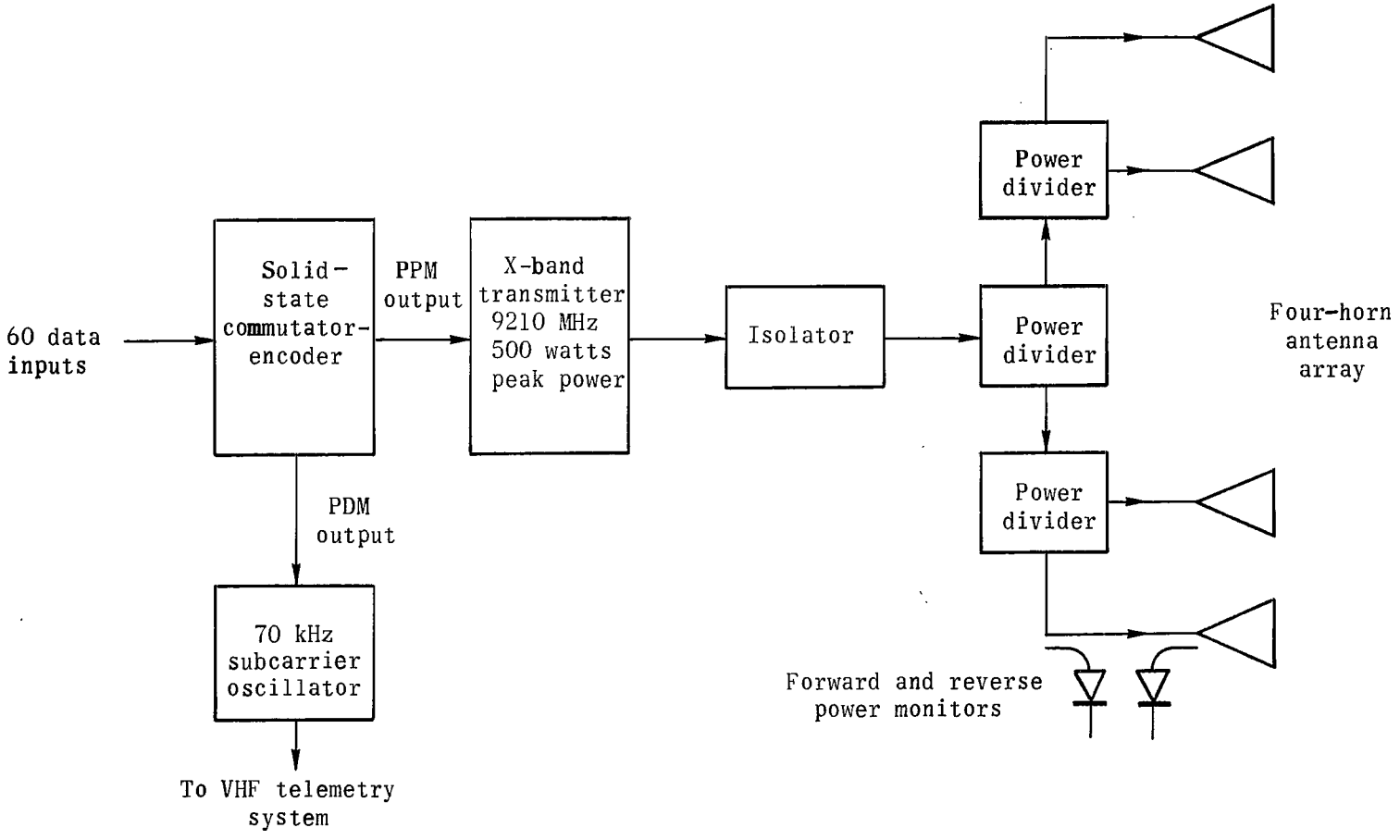

Figure 5.- Block diagram of X-band telemetry system.

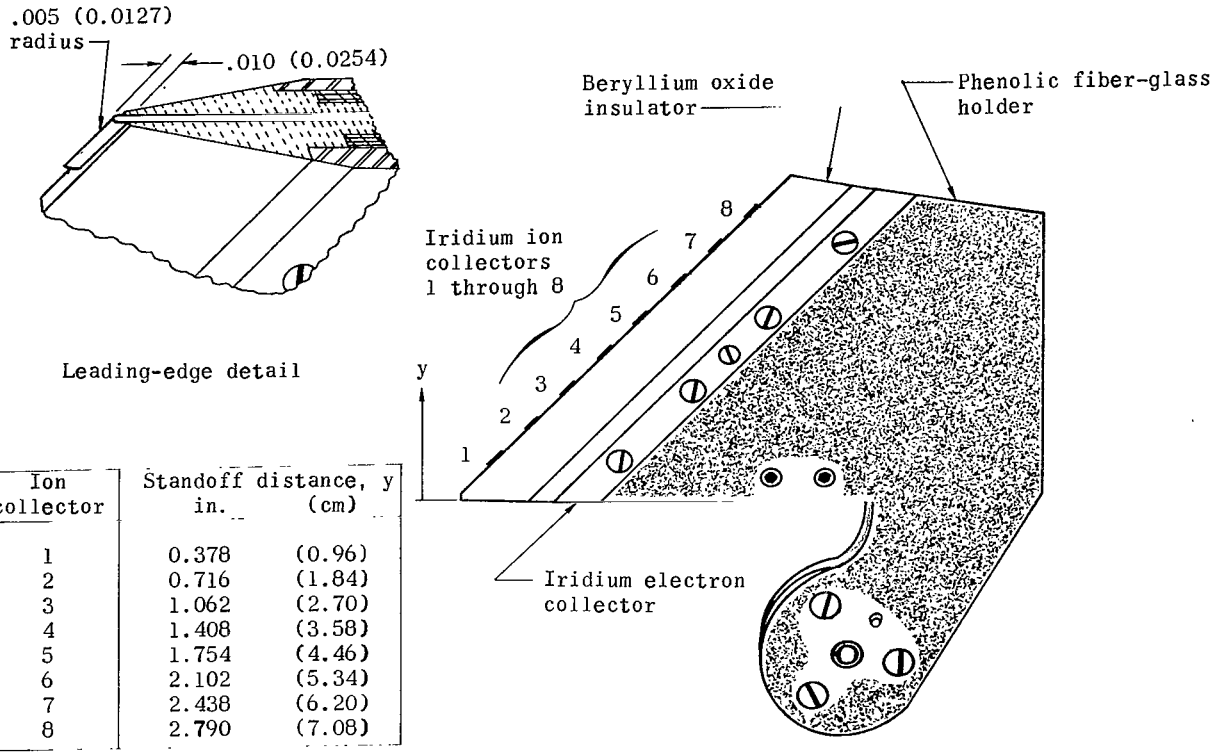

Ion collector	Standoff distance, y in.	(cm)
1	0.378	(0.96)
2	0.716	(1.84)
3	1.062	(2.70)
4	1.408	(3.58)
5	1.754	(4.46)
6	2.102	(5.34)
7	2.438	(6.20)
8	2.790	(7.08)

(a) Electrostatic probe configuration.

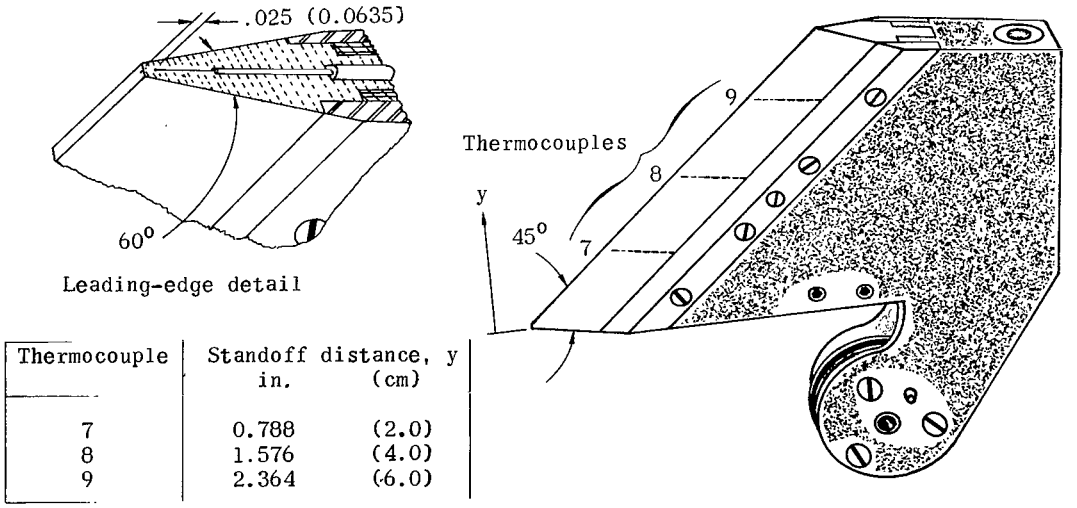

Thermocouple	Standoff distance, y in.	(cm)
7	0.788	(2.0)
8	1.576	(4.0)
9	2.364	(6.0)

(b) Thermocouple probe configuration.

Figure 6.- Body configurations of the electrostatic and thermocouple probes. All linear dimensions are in inches (centimeters).

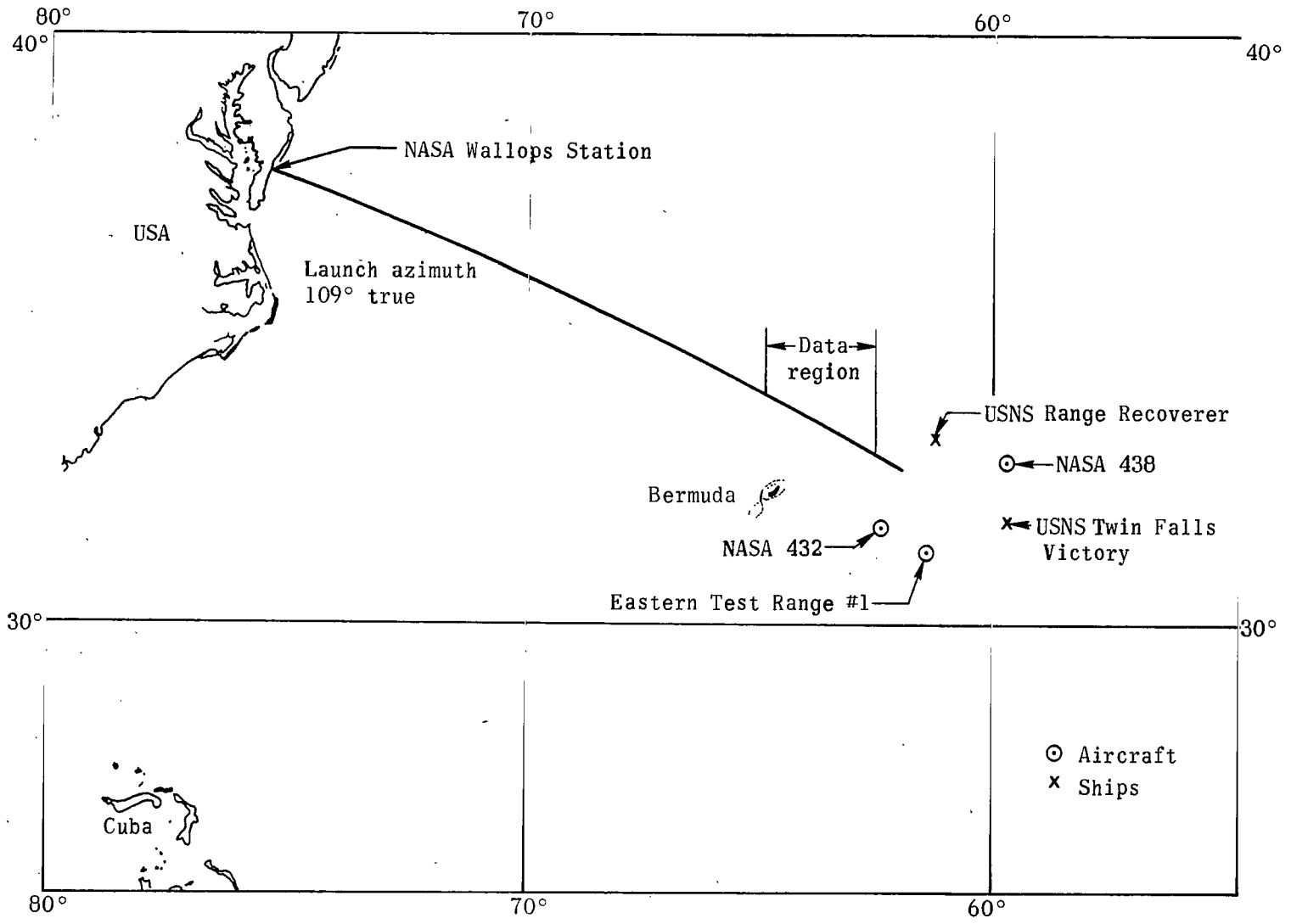

Figure 7.- RAM C-I ground track with relative locations of tracking ships and aircraft.

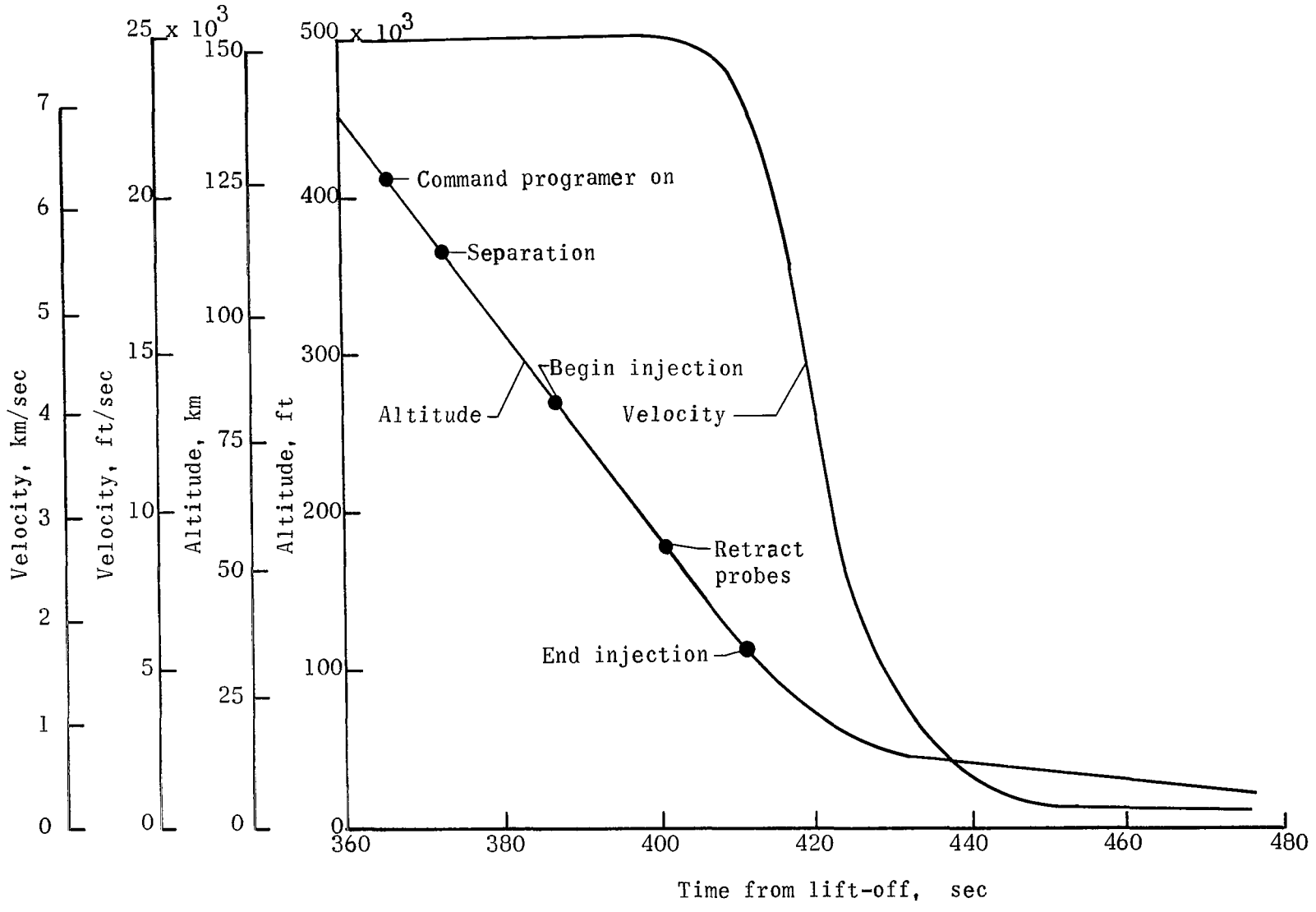

Figure 8.- RAM C-I reentry trajectory.

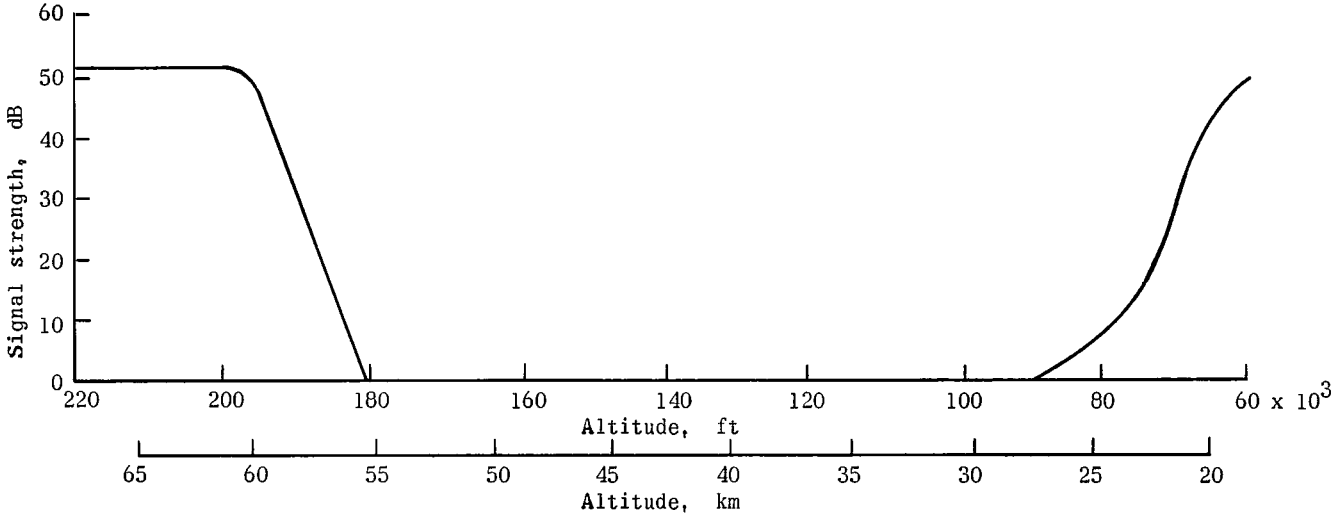

(a) AN/FPS-16 C-band radar. (Automatic beacon tracking; smoothed AGC data.)

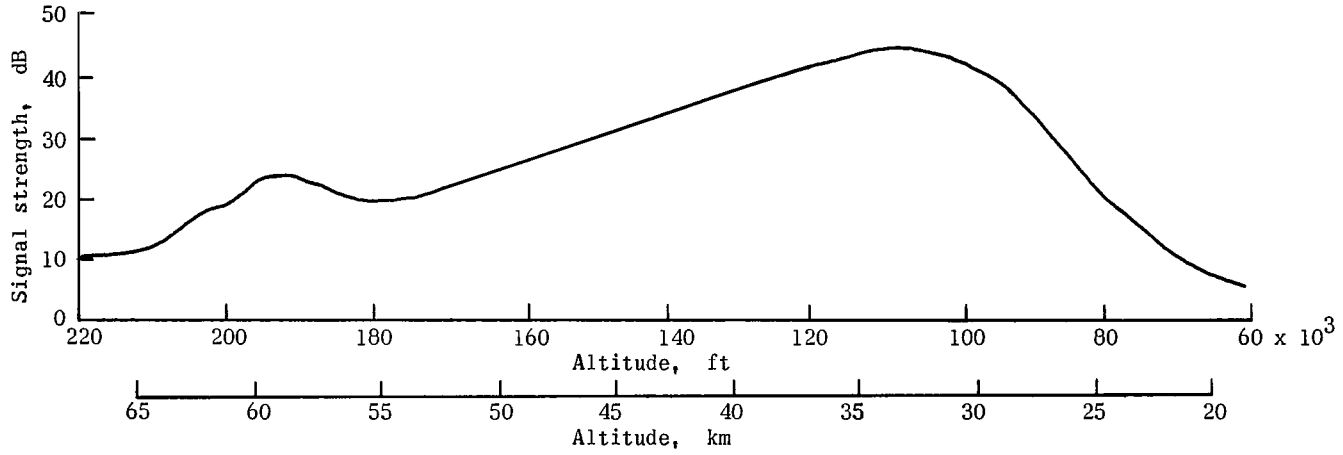

(b) AN/FPQ-6 C-band radar. (Automatic skin tracking; smoothed AGC data.)

Figure 9.- Strength of C-band radar signals received at Bermuda.

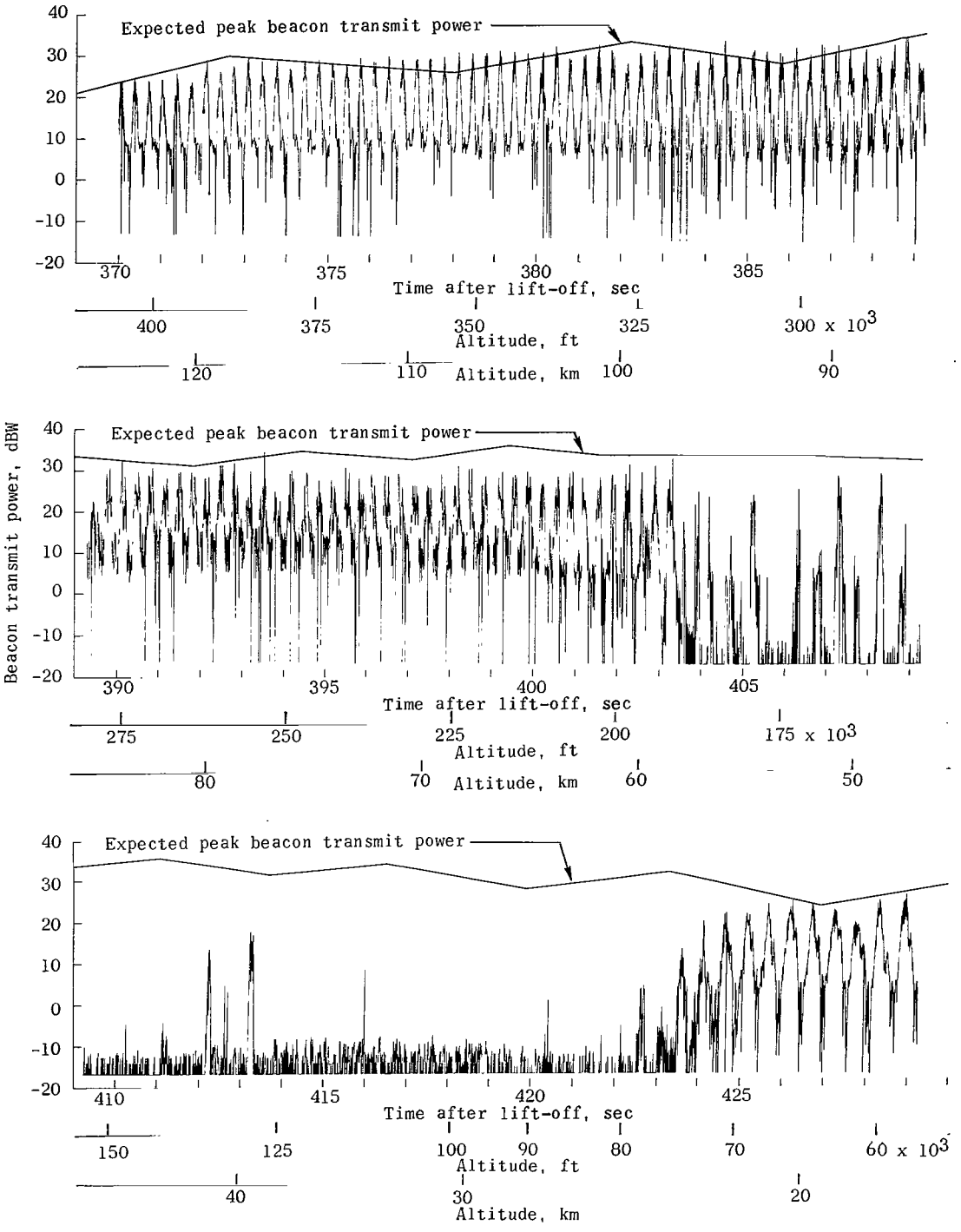

(c) Detailed beacon signal strength.

Figure 9.- Concluded.

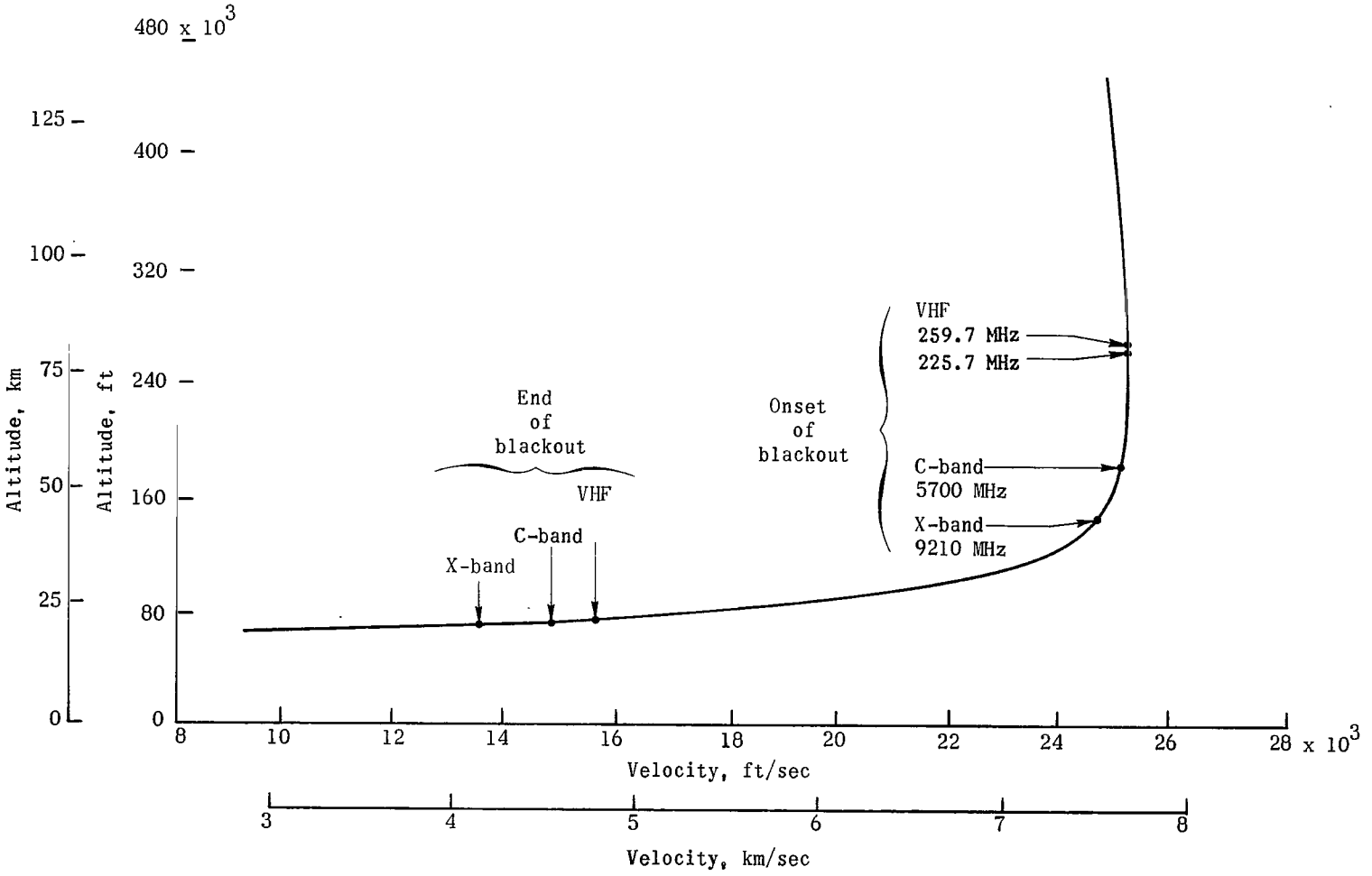

Figure 10.- RAM C-I altitude-velocity reentry profile showing onset and end of RF signal blackout.

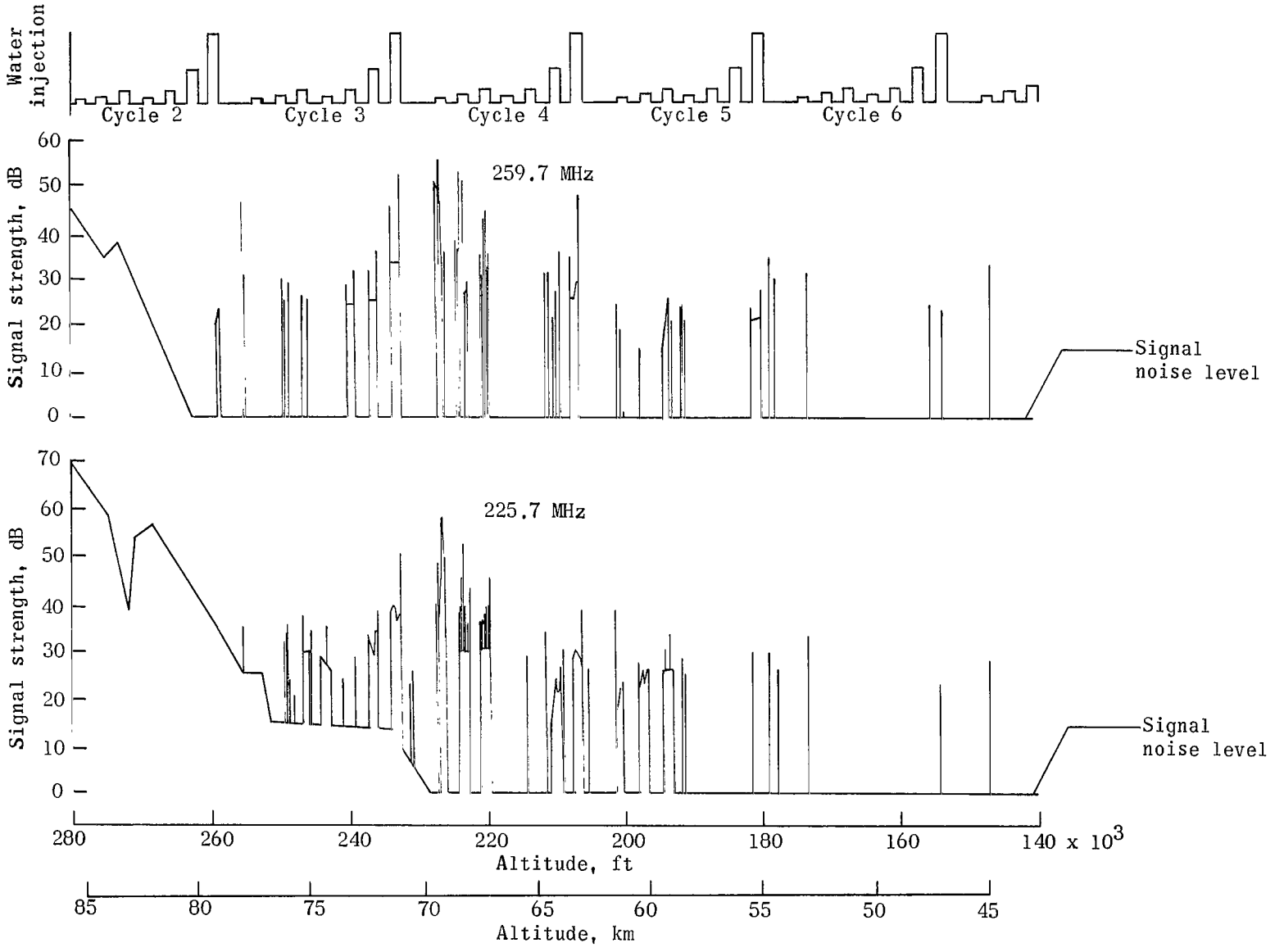

Figure 11.- RAM C-I water injection effects on VHF telemetry signal strength received aboard the USNS Twin Falls Victory.

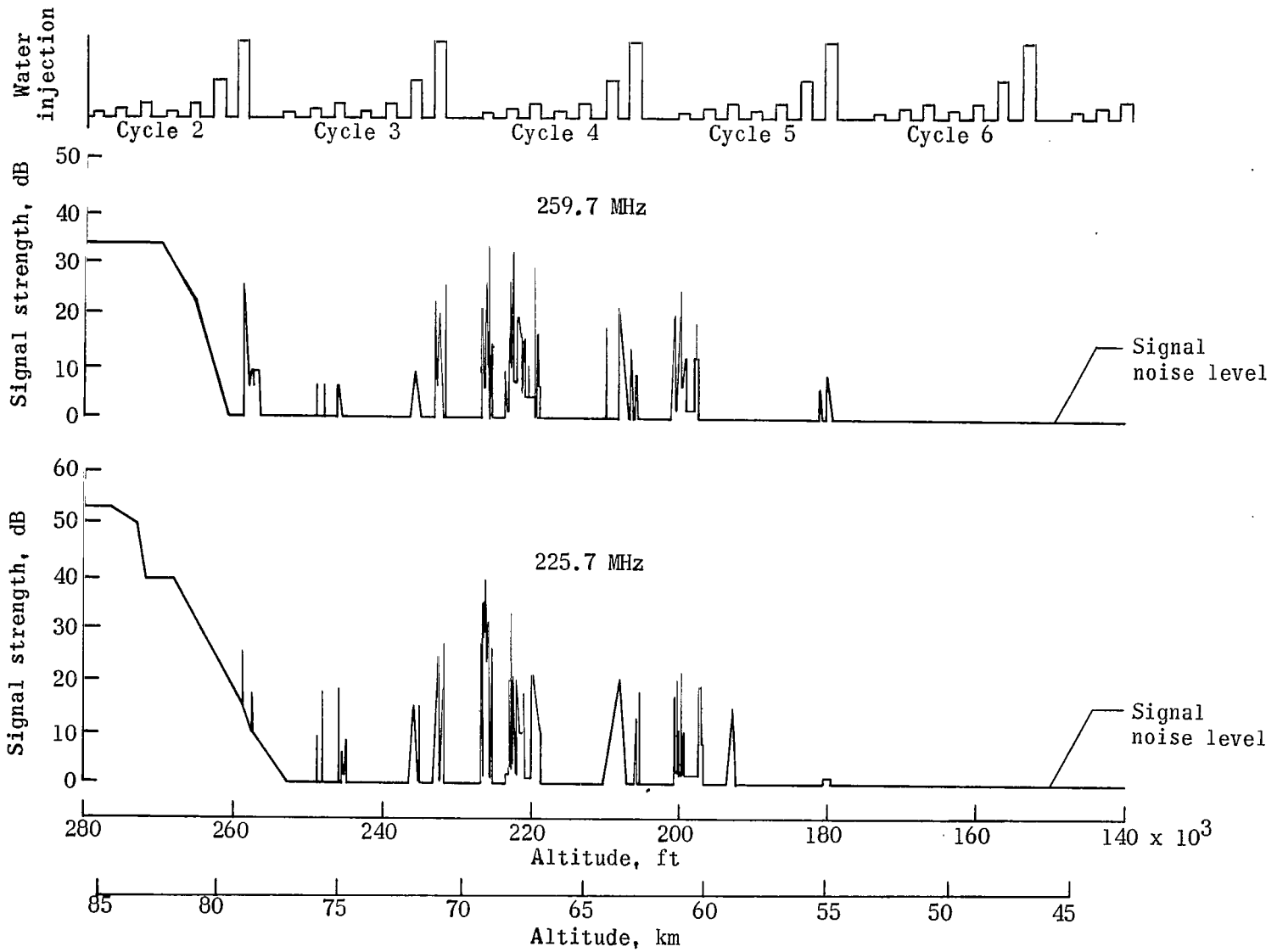

Figure 12.- RAM C-I water injection effects on VHF telemetry signal strength received aboard NASA aircraft 438.

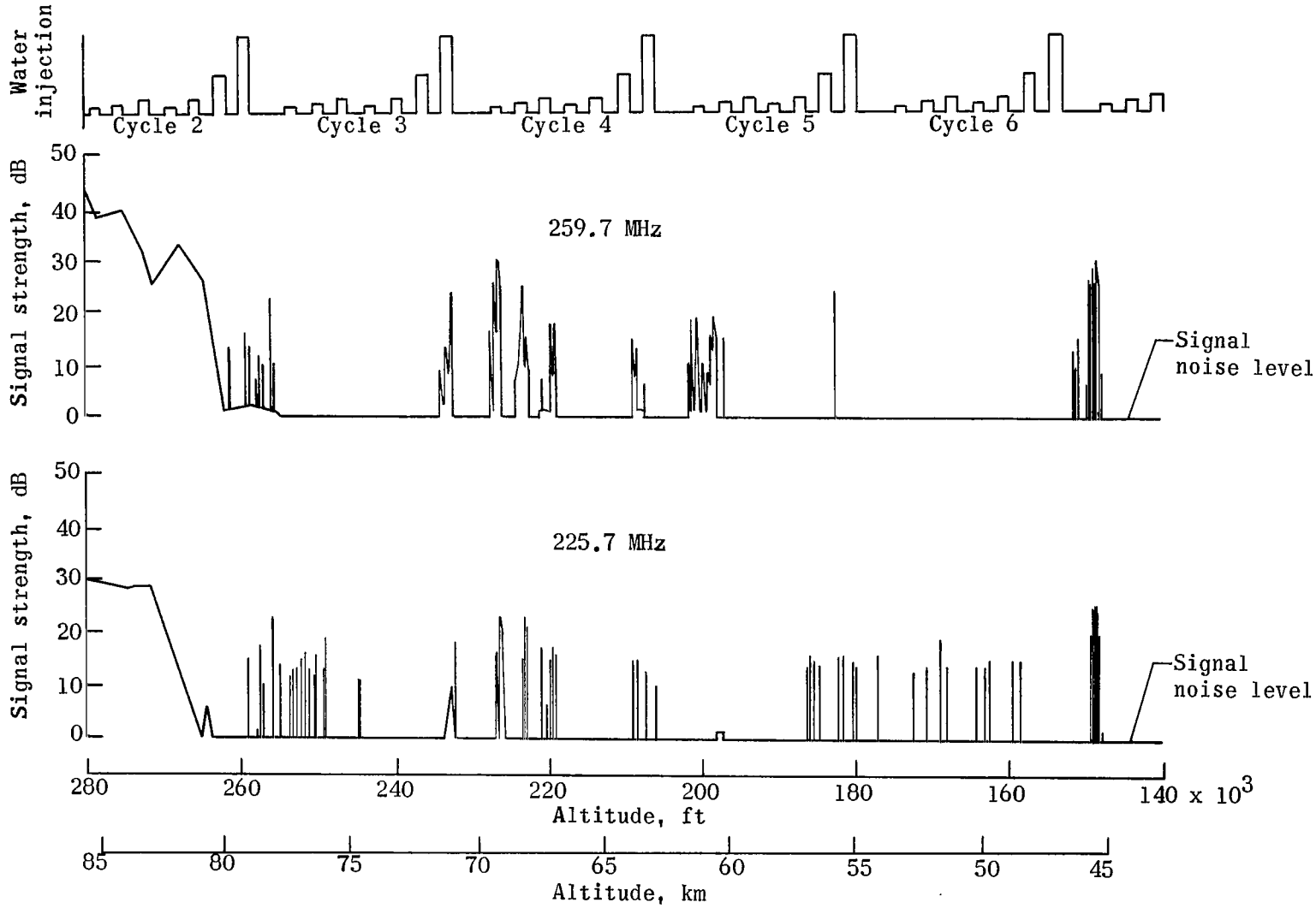

Figure 13.- RAM C-I water injection effects on VHF telemetry signal strength received aboard ETR aircraft number 1.

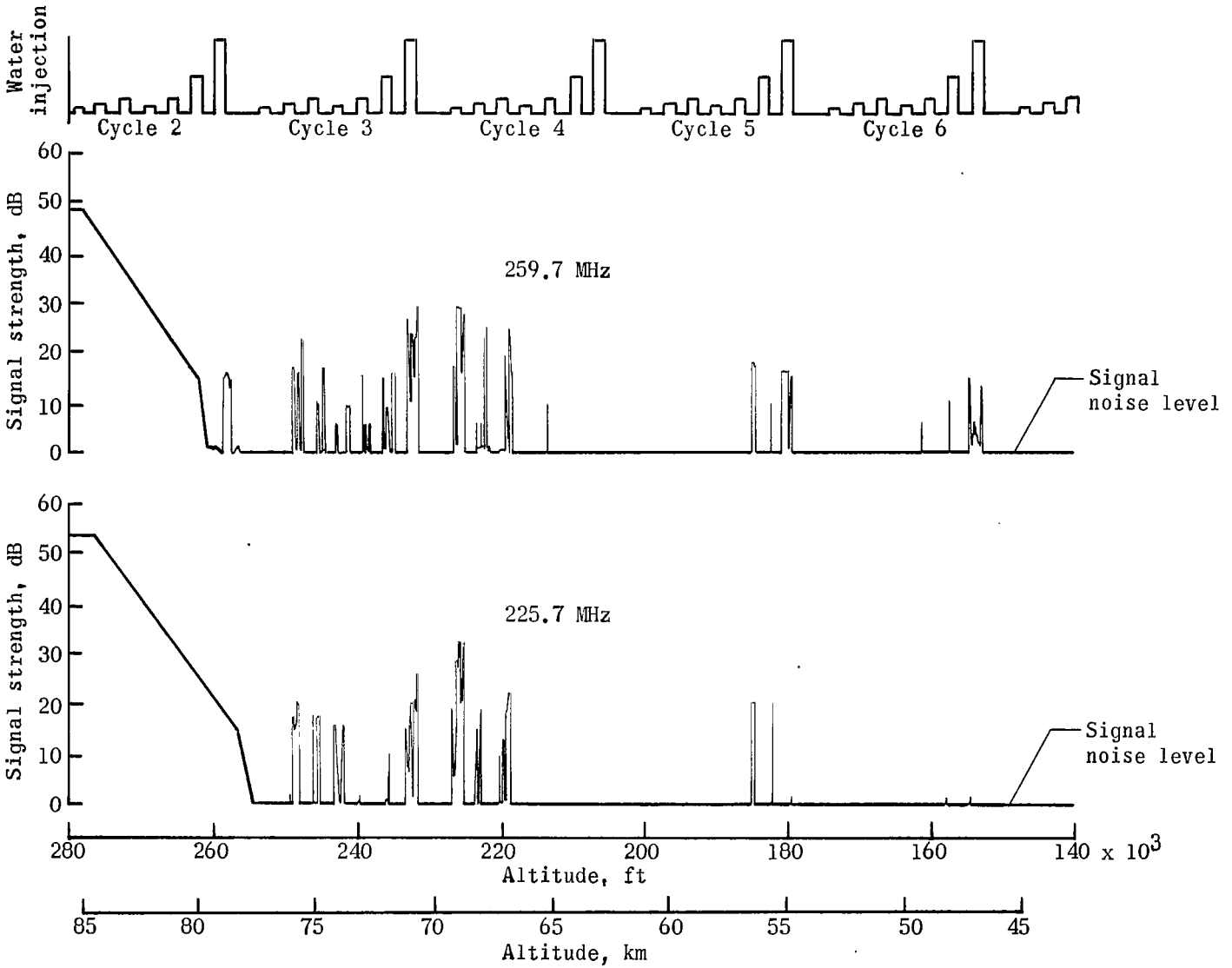

(a) Faired data.

Figure 14.- Records of VHF telemetry signal strengths received at Bermuda during RAM C-I water injection period.

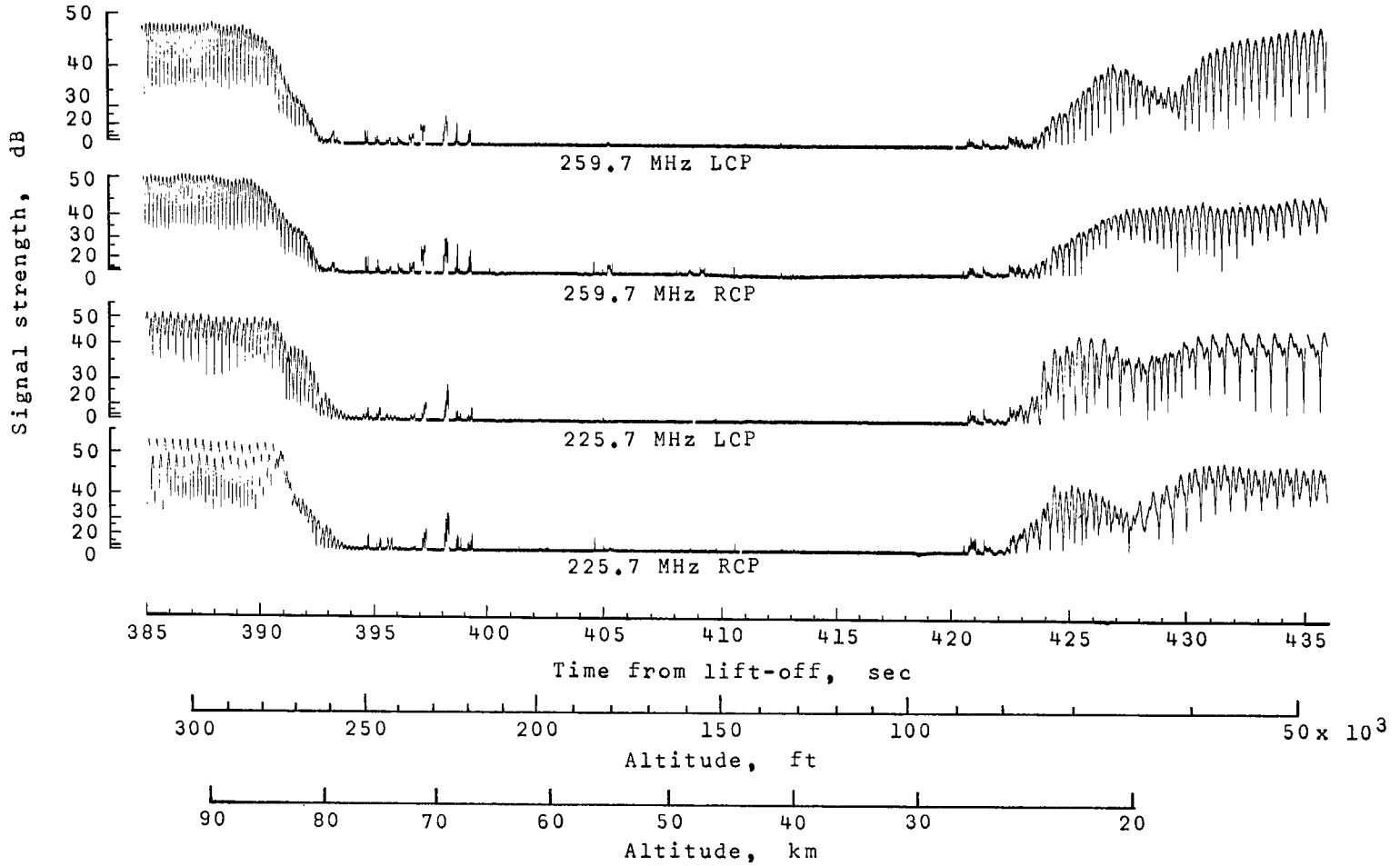

(b) Unfaired data. (LCP, left circular polarization; RCP, right circular polarization.)

Figure 14.- Concluded.

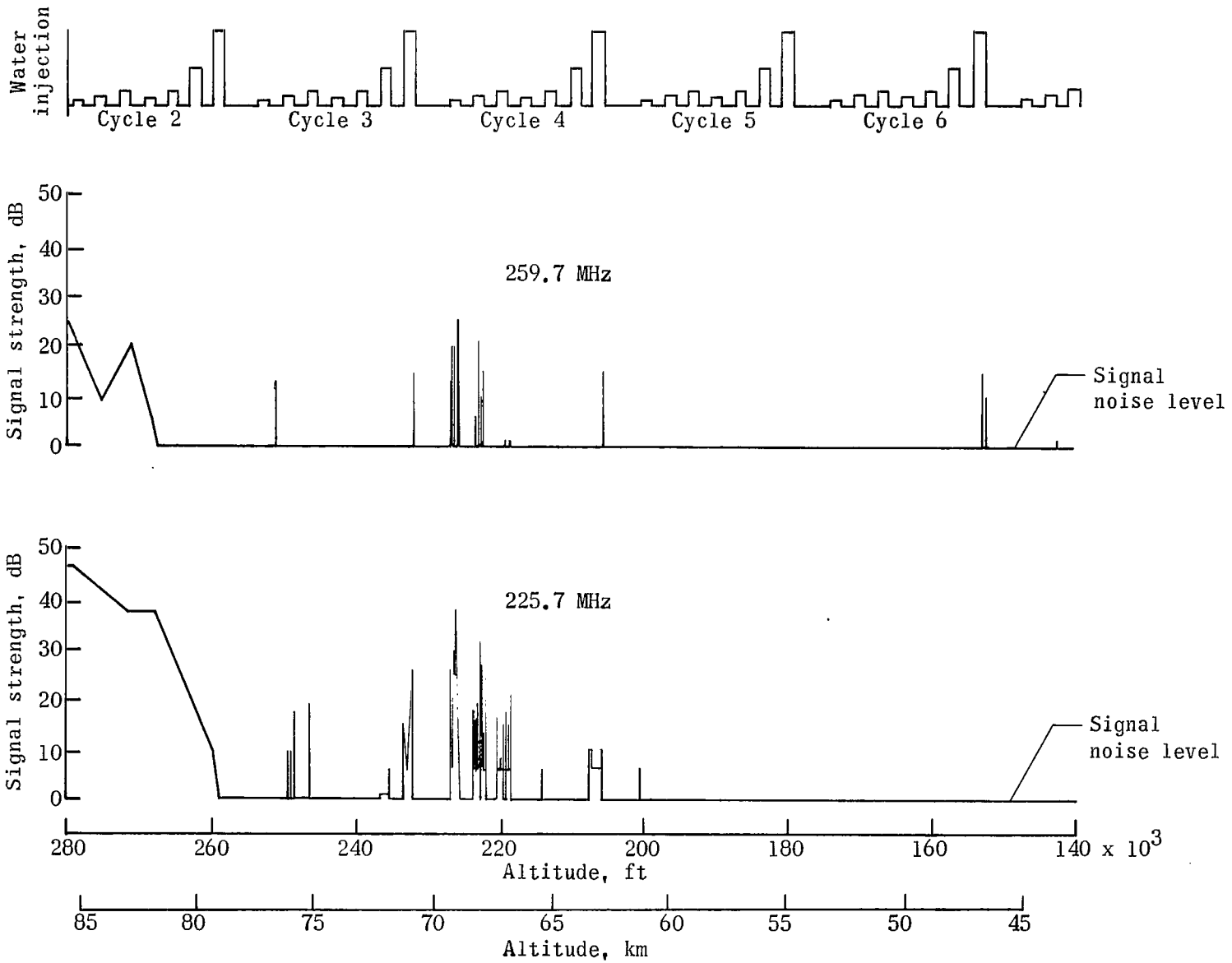

Figure 15.- RAM C-I water injection effects on VHF telemetry signal strength received aboard USNS Range Recoverer.

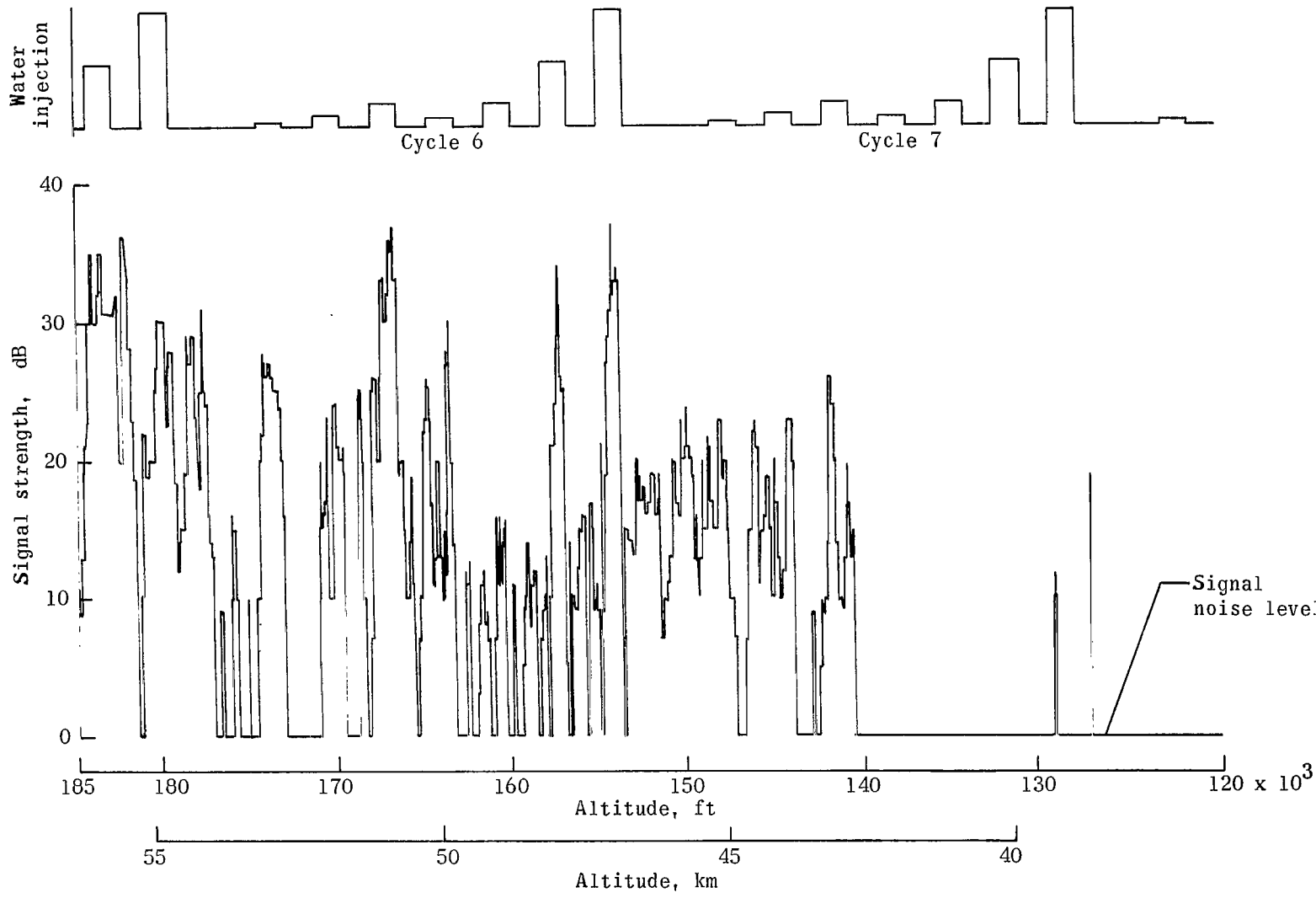

(a) Faired pulse-by-pulse data.

Figure 16.- Records of X-band telemetry signal strengths received at Bermuda during RAM C-I water injection period.

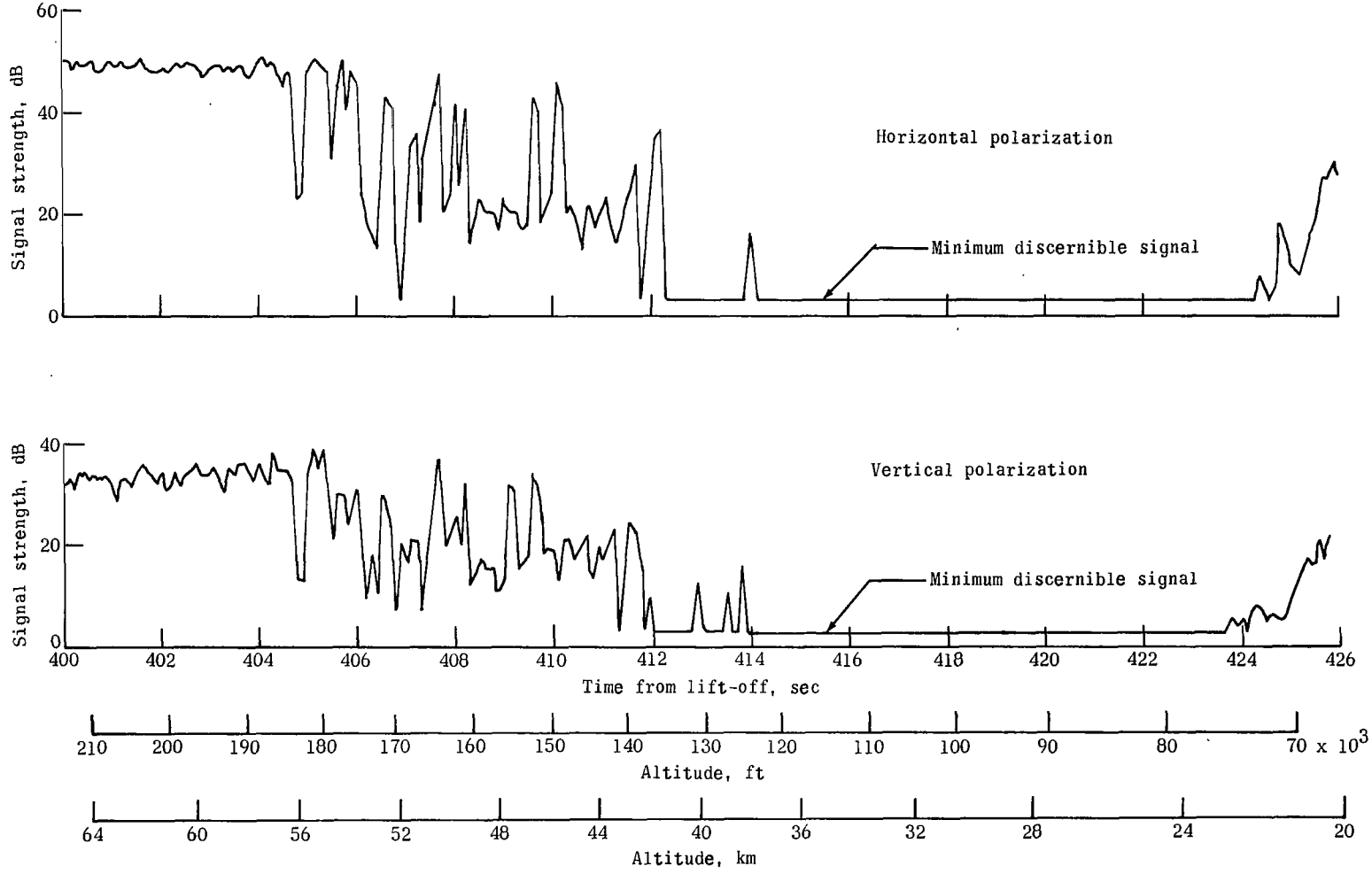

(b) Faired peak-pulse data.

Figure 16.- Concluded.

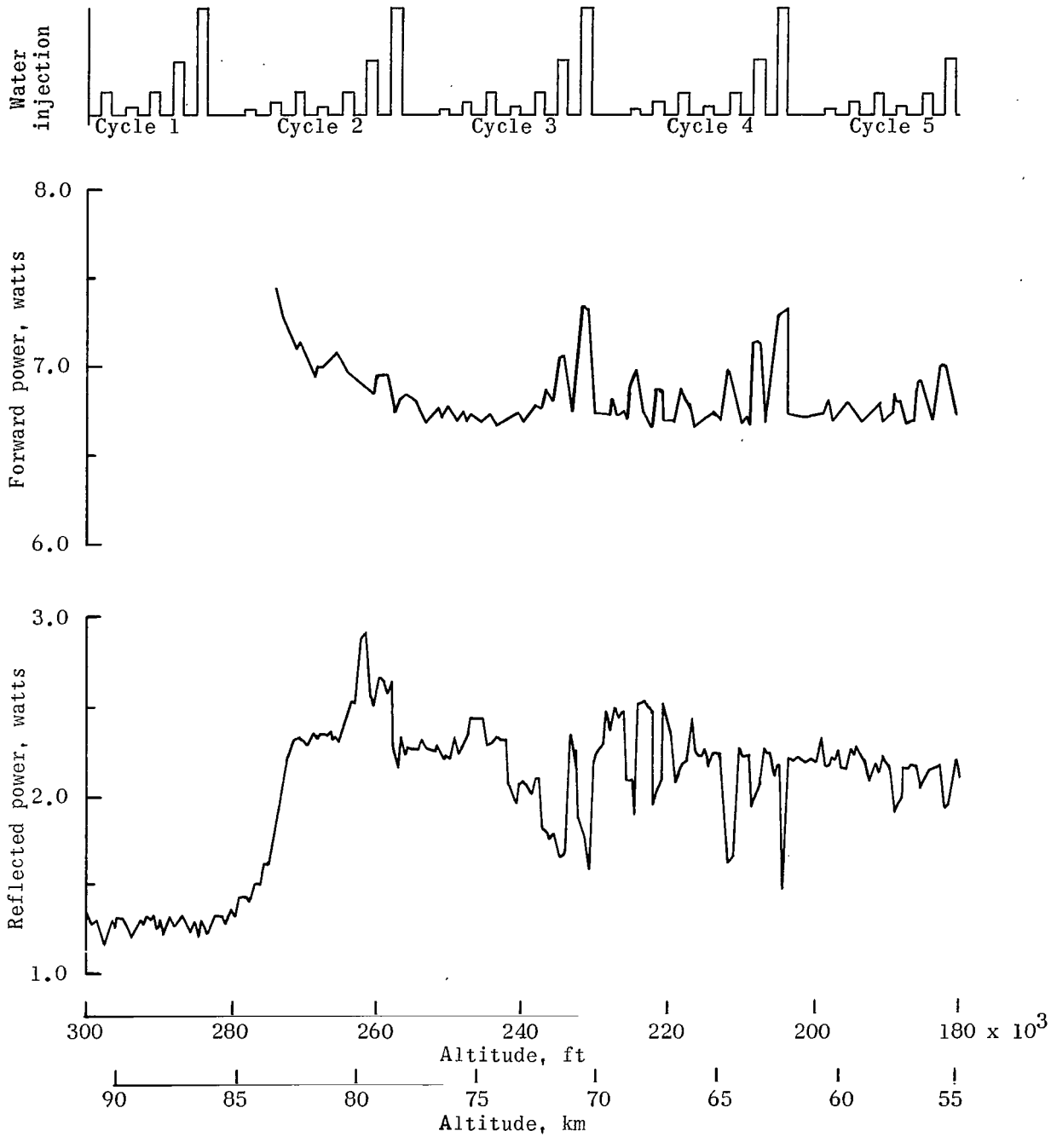

(a) 259.7-MHz system.

Figure 17.- Forward and reflected power of VHF and X-band telemetry systems as a function of altitude and water injection.

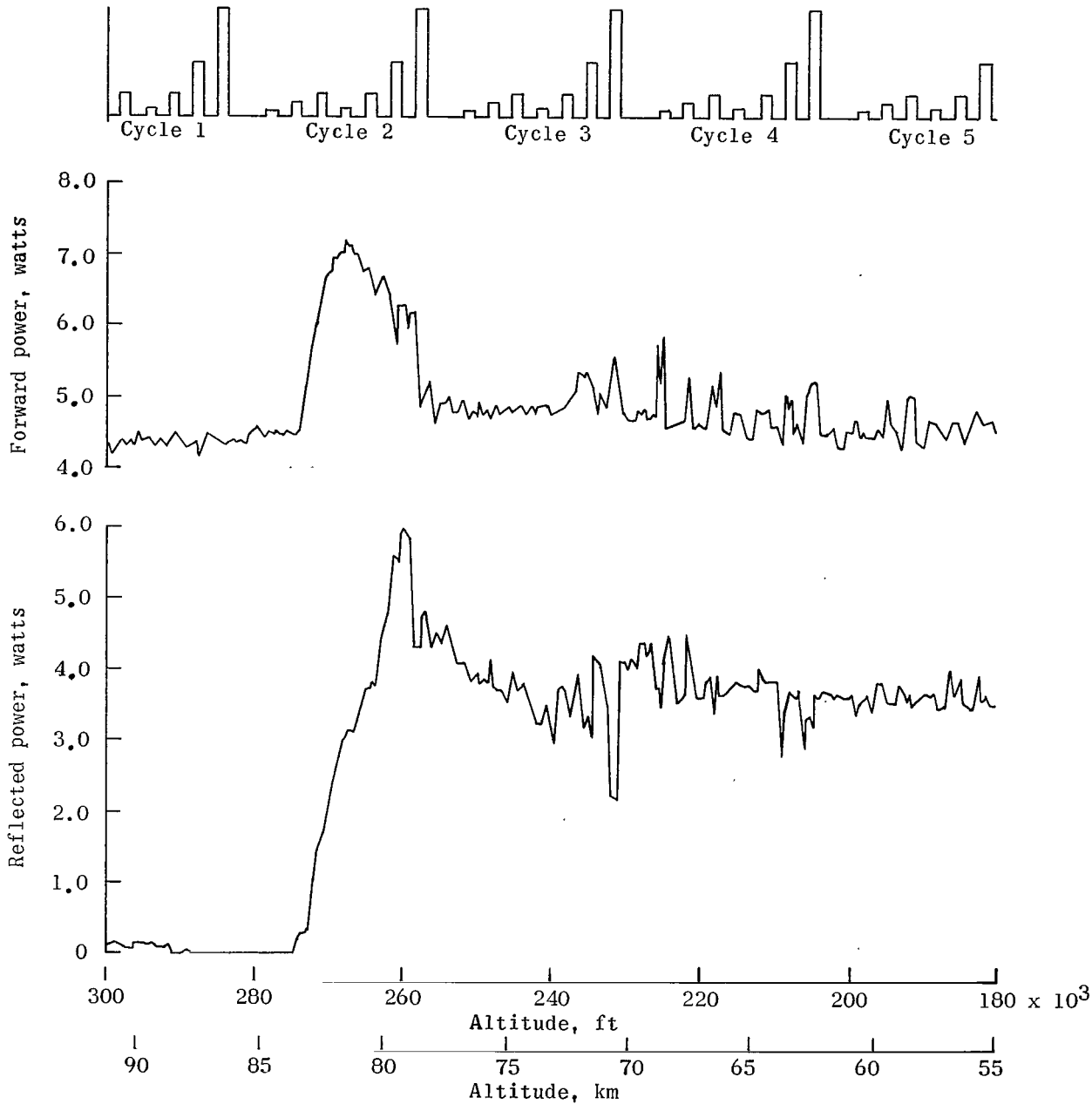

(b) 225.7-MHz system.

Figure 17.- Continued.

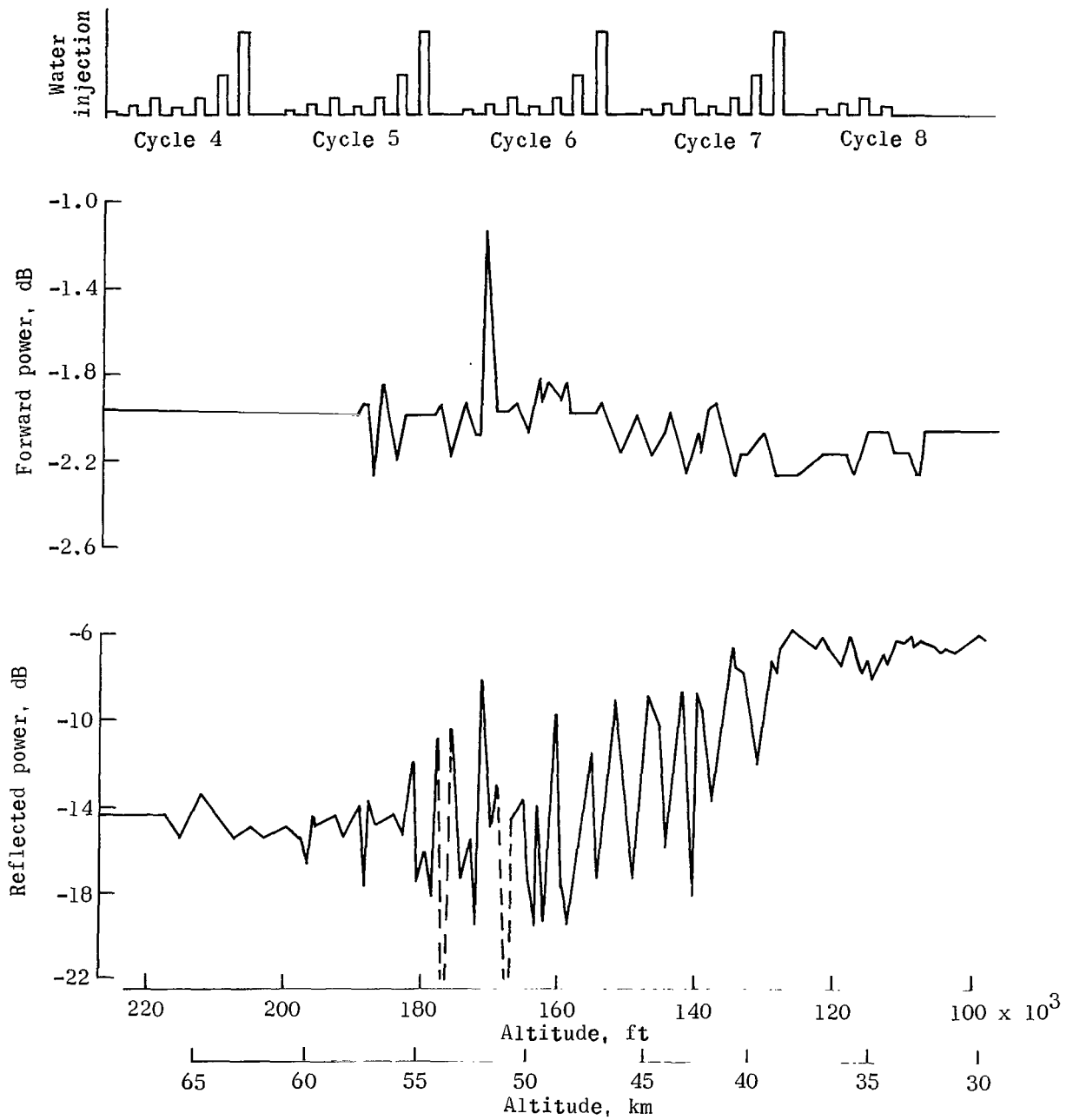

(c) 9210-MHz system.

Figure 17.- Concluded.

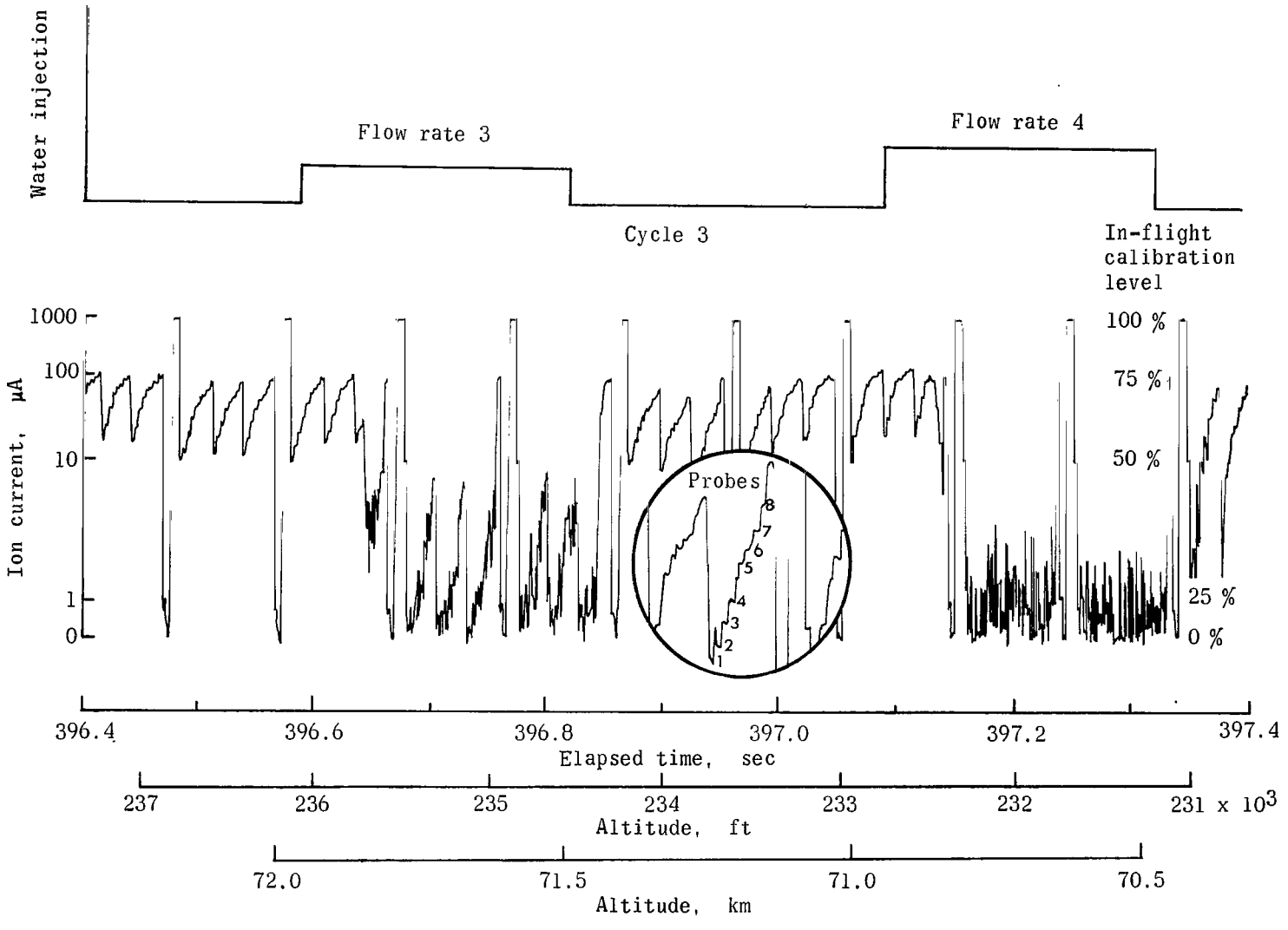

Figure 18.- Effects of water injection on electrostatic probe current measurements during injection cycle 3.

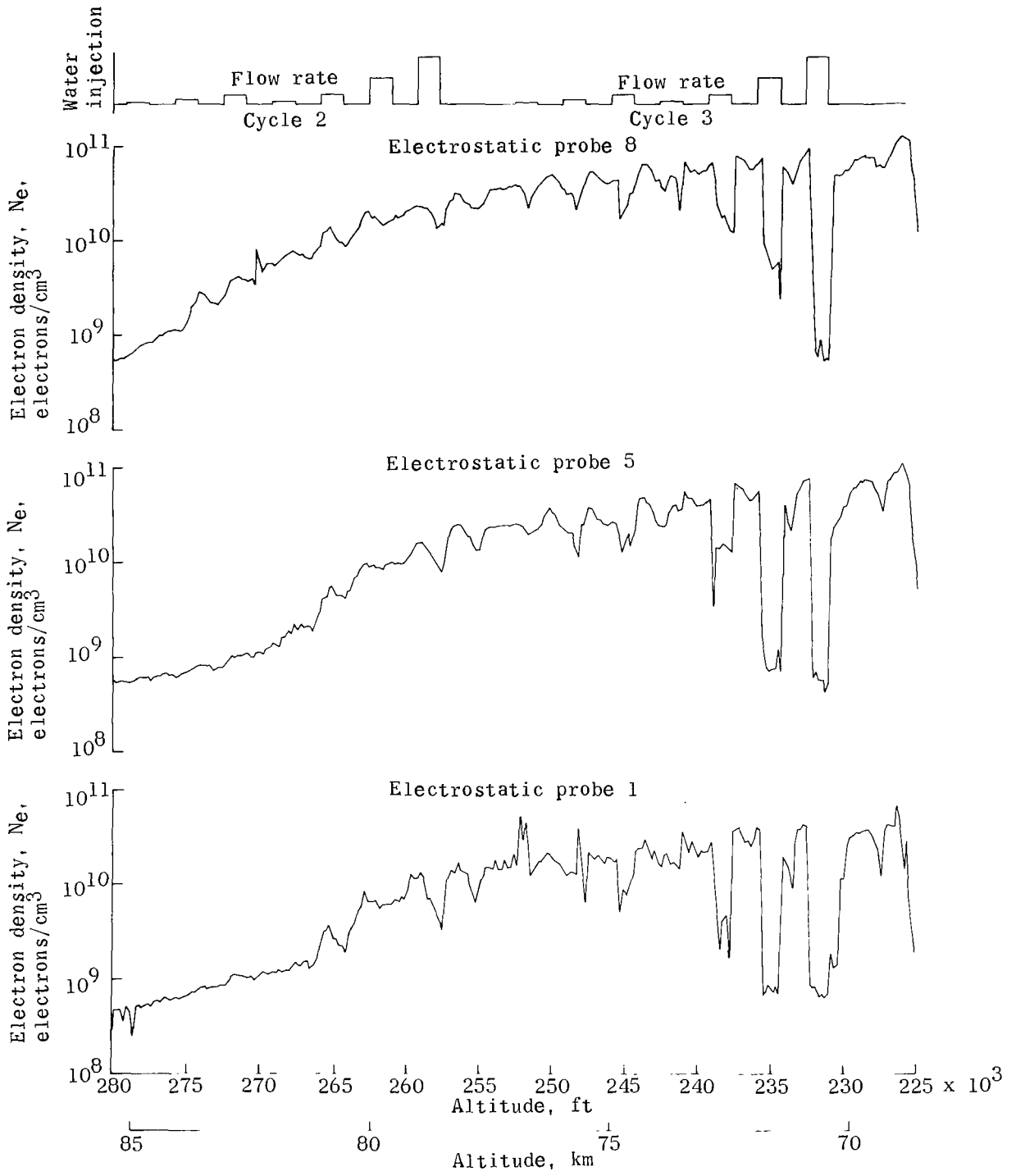

Figure 19.- Electron density of the RAM C-I flow field at standoff distances of 1, 4.5, and 7 cm as inferred from electrostatic probes 1, 5, and 8, respectively.

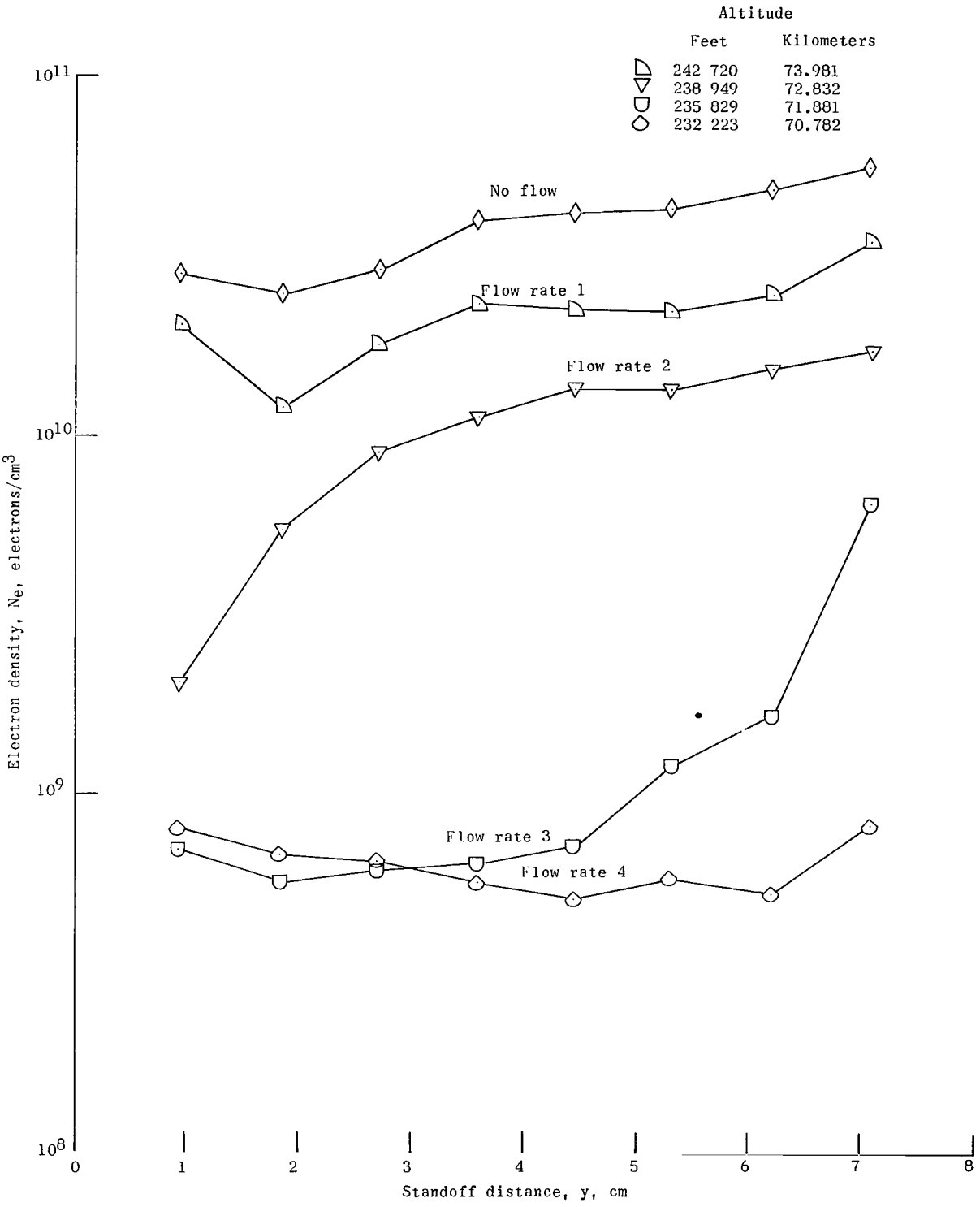

Figure 20.- Electron density distribution profiles for various injection flow rates of cycle 3.

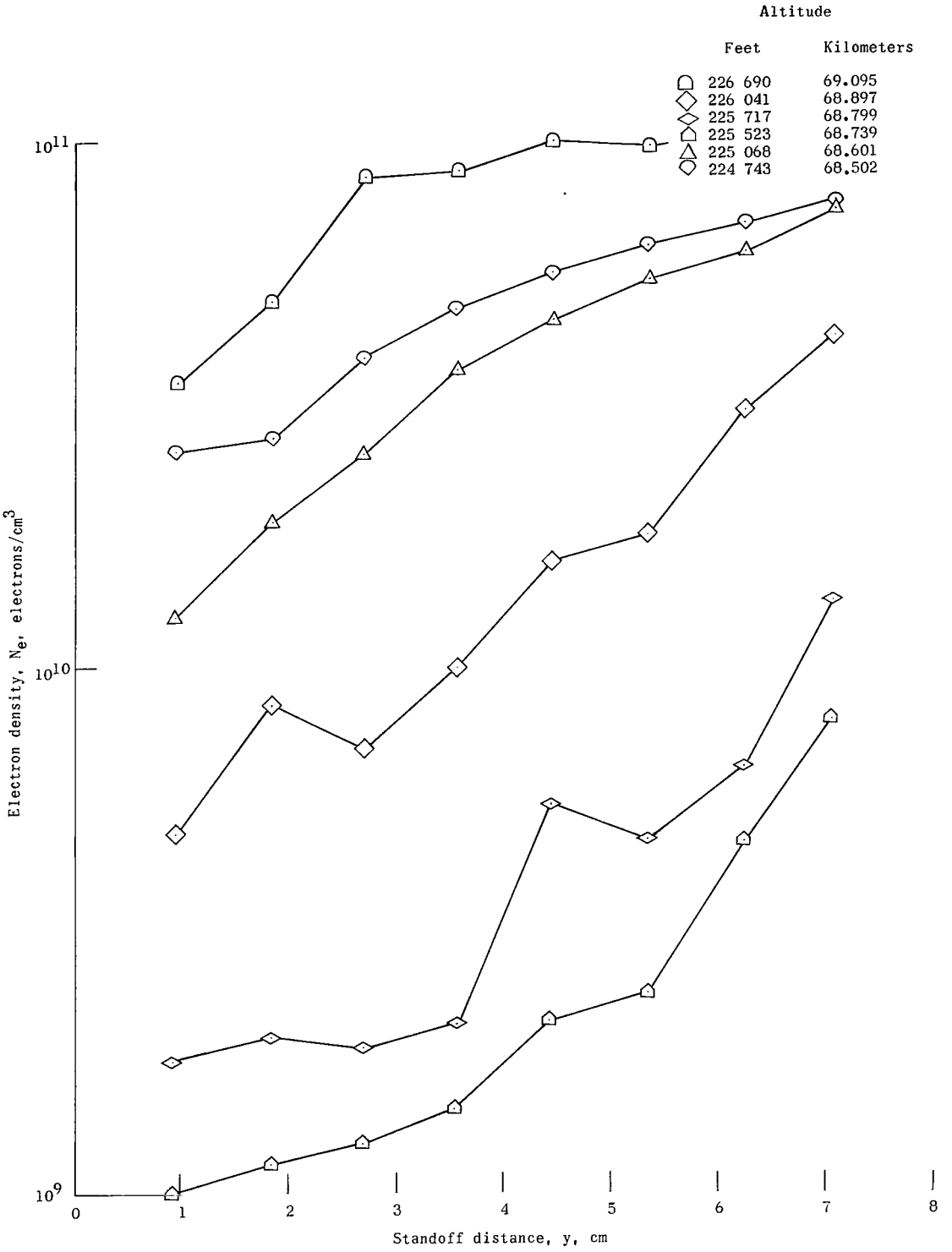

Figure 21.- Effect of stagnation injection at flow rate 5 of cycle 4 on electron density distribution profiles at various altitudes.

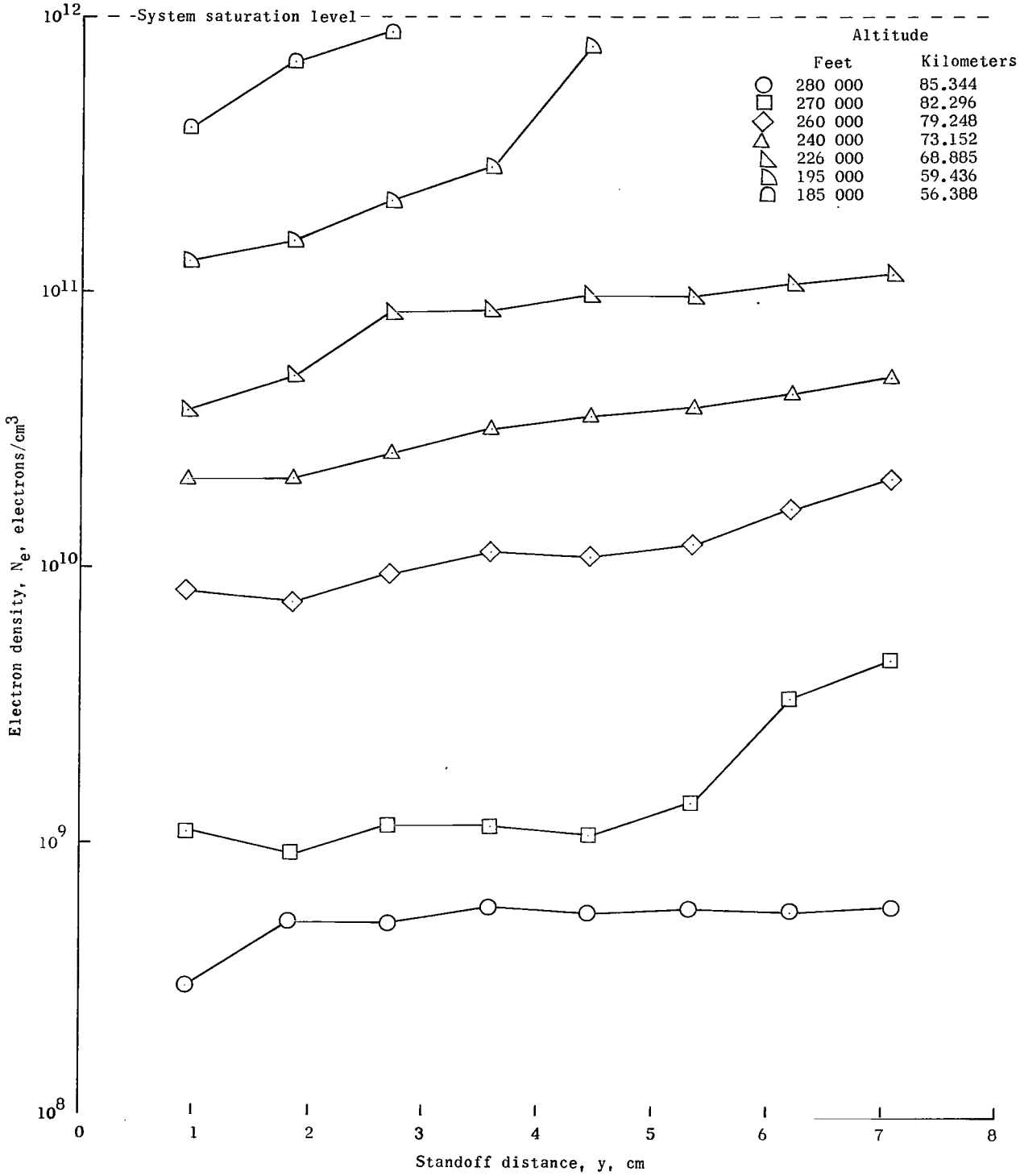

Figure 22.- Electron density distribution profiles at various altitudes. No water injection.

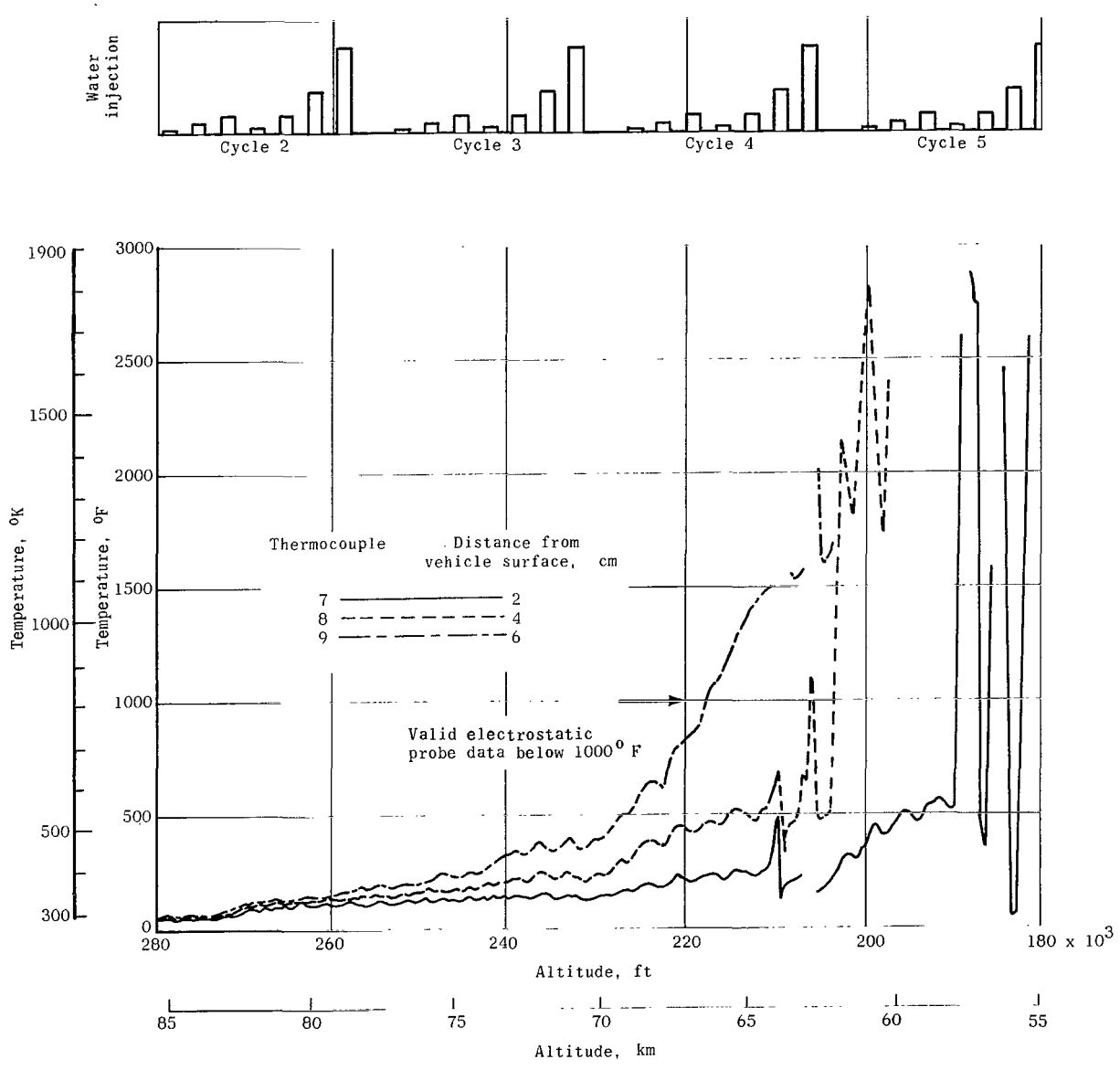

Figure 23.- Variation of thermocouple probe leading-edge temperature with altitude.

APPENDIX A

DESCRIPTION OF RAM C-I VHF TELEMETRY ANTENNA SYSTEMS

By Thomas G. Campbell

Introduction

The RAM C-I had two VHF telemetry systems for the transmission of "direct" time and "delayed" time data. The antennas designed for these telemetry systems consisted of two diametrically opposed cavity-backed slot antennas for the transmission of direct-time data and an array of circumferential slot antennas that transmitted the delayed-time data during the playback portion of the flight. This appendix presents a brief discussion of the design and development of these antenna systems and the final performance characteristics of each system.

The design objectives for the delayed-time telemetry antenna system were as follows:

(1) Optimize the pattern and radiation efficiency for the playback portion of the trajectory

(2) Provide broadband impedance characteristics to minimize plasma-sheath near-field effects

(3) Reduce the possibility of electromagnetic interference when low-level components are used

The design objectives for the direct-time telemetry antenna system were as follows:

(1) Use thin rectangular slot antennas for comparison purposes (This type of antenna had been used on previous RAM experiments.)

(2) Optimize the radiation efficiency while providing broadside radiation from 30^{o} to 140^{o} off the payload nose (Typical antenna gain should be $\geqq$-5 dB for this electrically small antenna.)

(3) Reduce the possibility of electromagnetic interference when low-level components are used

Delayed-Time Telemetry Antenna

A circumferential slot array was designed for the RAM C-I delayed-time telemetry antenna at a frequency f of 225.7 MHz to achieve end-fire (off the nose and tail)

radiation pattern characteristics. These characteristics were to optimize tracking and data acquisition during reentry and the playback phase of the trajectory.

The design of circumferential slot arrays has been discussed extensively in the past with respect to achieving omnidirectional pattern characteristics in the roll plane, but achieving end-fire or broadside radiation with polarization versatility is another problem. For this particular payload application, end-fire radiation was desired and obtained; however, the array could very easily have been altered to provide broadside radiation instead.

The antenna design was obtained by first testing two diametrically opposed circumferential slots on the coated conical configuration shown in figure A1. The slots were located in the aft portion of the nose cone to optimize the electrical length of each slot and to maximize the diametric spacing so that coupling would be reduced. The body circumference ka (where $k = \frac{2\pi}{\lambda}$, λ is wavelength in free space, and a is radius of nose cone) at the selected location is 1.34λ and the diameter d is 0.425λ. The two diametrically opposed slots were therefore spaced 0.425λ apart and the pattern control obtained agrees with the theory pertaining to an array of linear elements spaced the same distance apart. The two slots were fed in parallel with a half-wave-line balun which forced the potential at the feed point of each slot to be equal and opposite. A balanced-to-unbalanced impedance ratio of 4 is obtained and a 50-ohm impedance match was obtained at the paralleled input by adjusting the feed-point locations for each slot. The total slot length could also be adjusted by relocating shorting bolts across two circular rings inside the payload. The resulting slot lengths L were 0.334λ.

It is interesting to note that these two slots mounted on the cone provided radiation pattern control similar to that of an array of two linear $\frac{1}{2}\lambda$ elements with a spacing of approximately $\frac{1}{2}\lambda$ (ref. 26, pp. 279-300 and 471). The pattern results for the two slots on the cone are shown in figure A2(a) and A2(b). In figure A2(a) the slots are fed out of phase, that is, the center conductor of the feed line for one slot is connected to the forward side of the slot and the center conductor for the second slot is connected to the aft side of the slot. In figure A2(b) the pattern is for end-fire radiation and this pattern is obtained by merely reversing the feed polarity of the second slot. Therefore, the center conductor for each slot was connected to the forward side of the slot.

Since end-fire radiation was desired for this particular payload, two additional slots were added to the array to optimize the polarization of the end-fire radiation. The additional slots were also diametrically opposed and fed with a half-wave-line balun. The resulting pattern is essentially the superposition of the fields from the two pairs of slots and the measured results are shown in figure A2(c). The capability for end-fire circular polarization is evident in the pattern amplitudes of the orthogonal linear polarization. The sense of the circular polarization was easily altered by adjusting the phase

angle ϕ between slot pairs and the results are presented in figure A3. For $\phi = 0^{o}$, the time-phase angle by which the vertical component of the electric field leads the horizontal component of the electric field is 90^{o} and, when the nose cone is viewed off the nose, the sense of the circular polarization is left-hand circular or a clockwise wave approaching. As the payload is viewed from the rear, the sense of the circular polarization is right-hand circular or a clockwise wave receding. As ϕ is increased, the sense is completely reversed with right-hand circular off the nose and left-hand circular off the tail. The same polarization versatility could be achieved for broadside radiation by changing the polarity of the slots accordingly. The patterns in figure A3 are also shown for several roll angles Φ, and no severe pattern changes were observed.

The final radiation characteristics were somewhat different from those shown in figure A3 due to a change in the polarization capability of the main tracking ship. Therefore, the phase variation between slot pairs was changed to produce a more linearly polarized signal off the nose and tail of the payload. The final impedance, VSWR, and typical radiation pattern characteristics of the delayed-time telemetry antenna are shown in figures A4(a), A4(b), and A5, respectively.

Direct-Time Telemetry Antenna

Two diametrically opposed, axial, cavity-backed slot antennas were used to transmit the direct-time telemetry data during the RAM C-I flight experiment. Slot antennas were used on previous RAM experiments and, therefore, they were used on this RAM payload for comparative purposes. Two antennas were used (locations are shown in fig. A1 and in sketch in table I) so that signal variation due to payload spin could be minimized. In order to prevent corona, the slot apertures were pressurized instead of being encapsulated. The slots were pressurized by placing a thin phenolic cover over the apertures. The cover contained a valve that would close when the ambient pressure dropped below 3.5 psi (24.132 kN/m^2).

Since an encapsulating dielectric is usually lossy, pressurizing the slots increased the radiation efficiency. Pressurizing the slots also simplified the task of tuning the cavity-backed slot antennas because there was no need to compensate for an encapsulating dielectric. In figure A1 can be seen the pressurizing cover over the slot aperture.

The free-space impedance and voltage standing wave characteristics of the direct-time telemetry antennas are shown in figure A6. As expected, these antennas are narrow bandwidth and experienced a near-field detuning effect when they were surrounded by the plasma sheath.

Typical radiation pattern characteristics of the direct-time telemetry antenna are shown in figure A7. On the basis of these radiation pattern characteristics, it was concluded that this antenna system would satisfy the experiment objective.

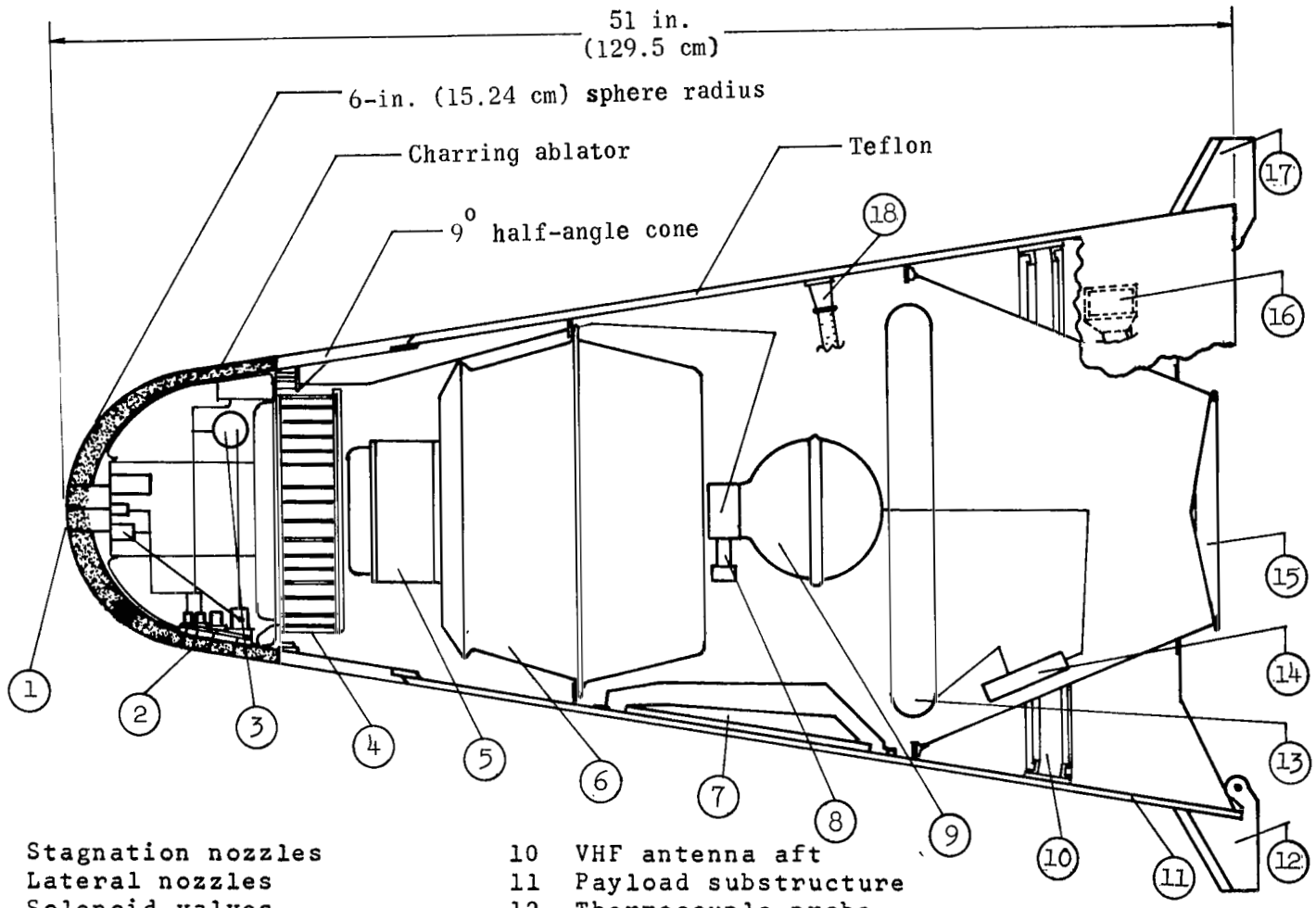

1	Stagnation nozzles	10	VHF antenna aft
2	Lateral nozzles	11	Payload substructure
3	Solenoid valves	12	Thermocouple probe
4	Power supply	13	Nitrogen supply
5	Tape recorder	14	Regulator
6	Telemetry package	15	Payload to Scout transition
7	VHF antenna forward	16	C-band antenna
8	Squib valve	17	Electrostatic probe
9	Material addition storage	18	X-band antenna

Figure A1.- RAM C-I configuration showing experiment and instrumentation systems.

APPENDIX A

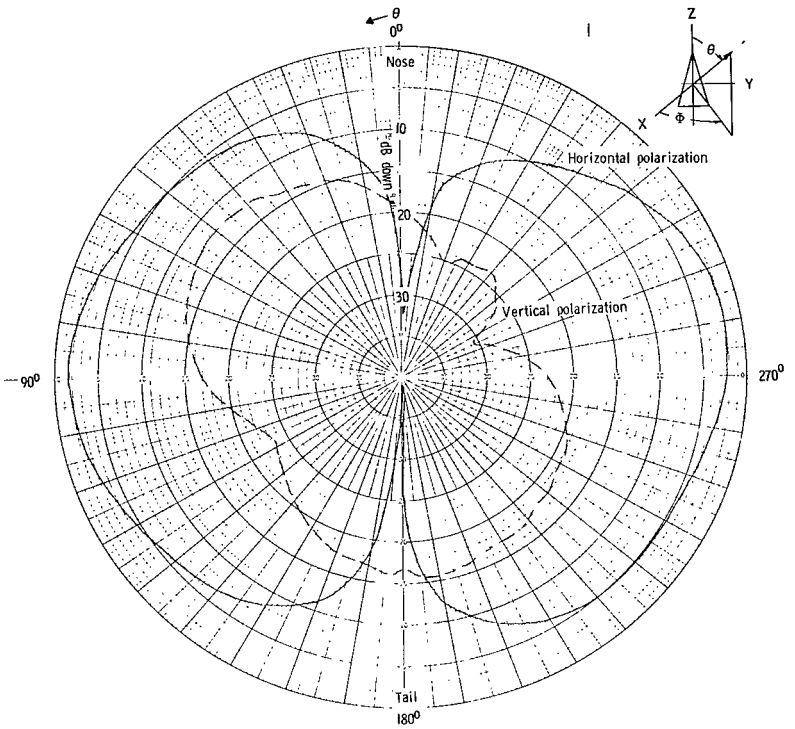

(a) Slots fed out of phase.

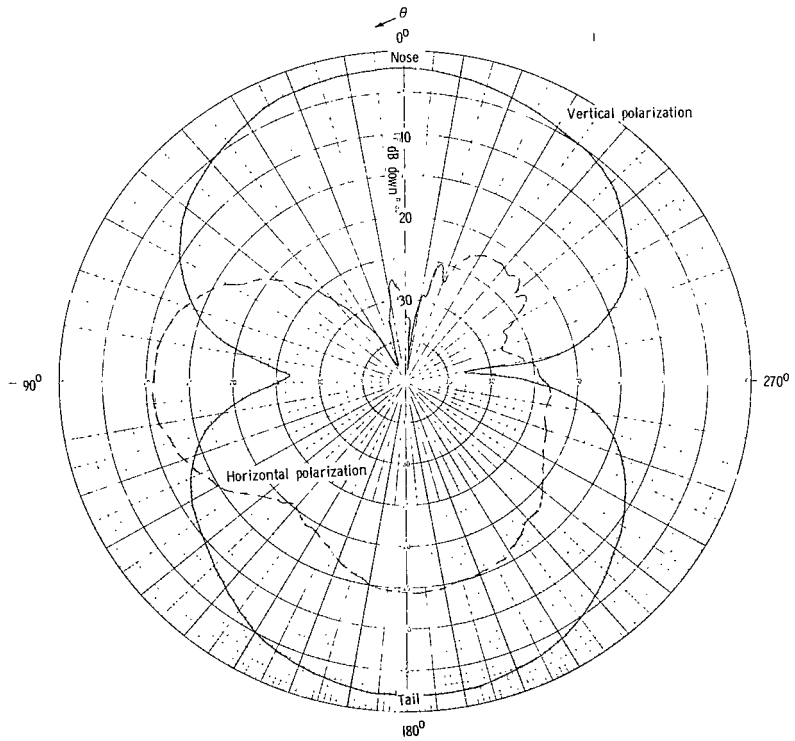

(b) Slots fed in phase.

Figure A2.- Radiation pattern diversity capabilities of the circumferential slot array. Elevation plane.

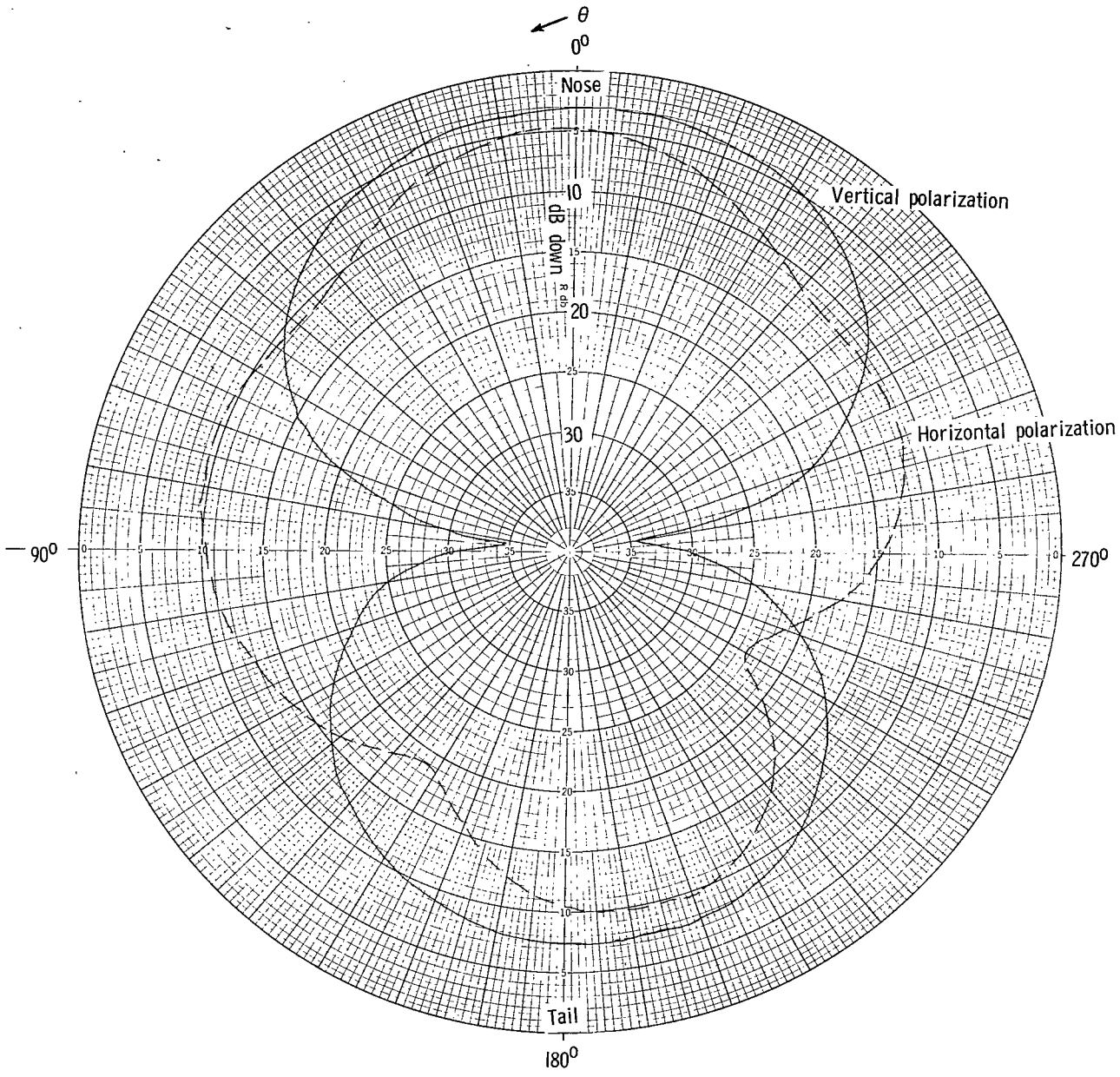

(c) Four slots fed in phase.

Figure A2.- Concluded.

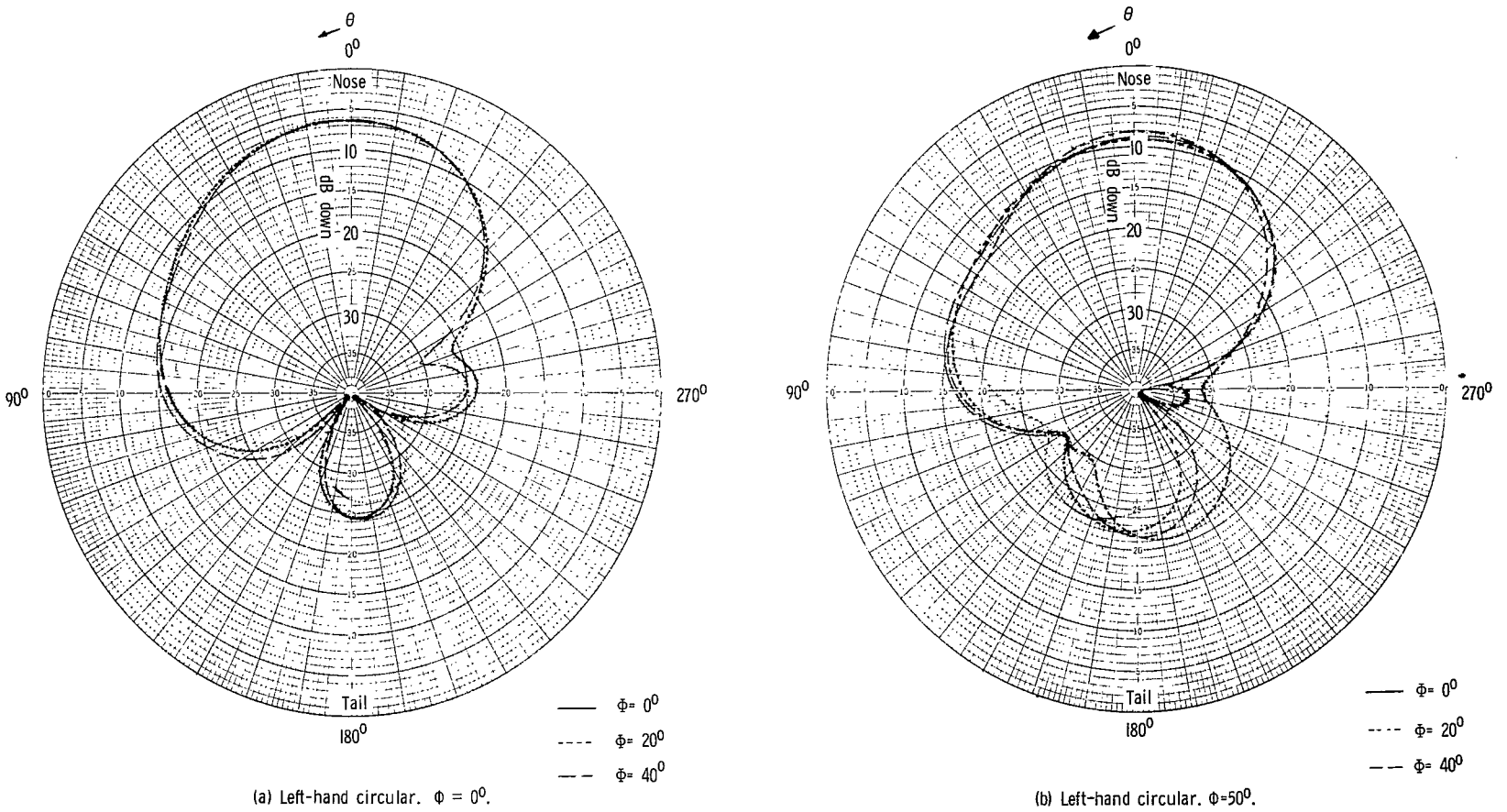

(a) Left-hand circular. $\Phi = 0^{\circ}$.

(b) Left-hand circular. $\Phi = 50^{\circ}$.

Figure A3.- Polarization diversity capabilities of the end-fire slot array. Elevation plane.

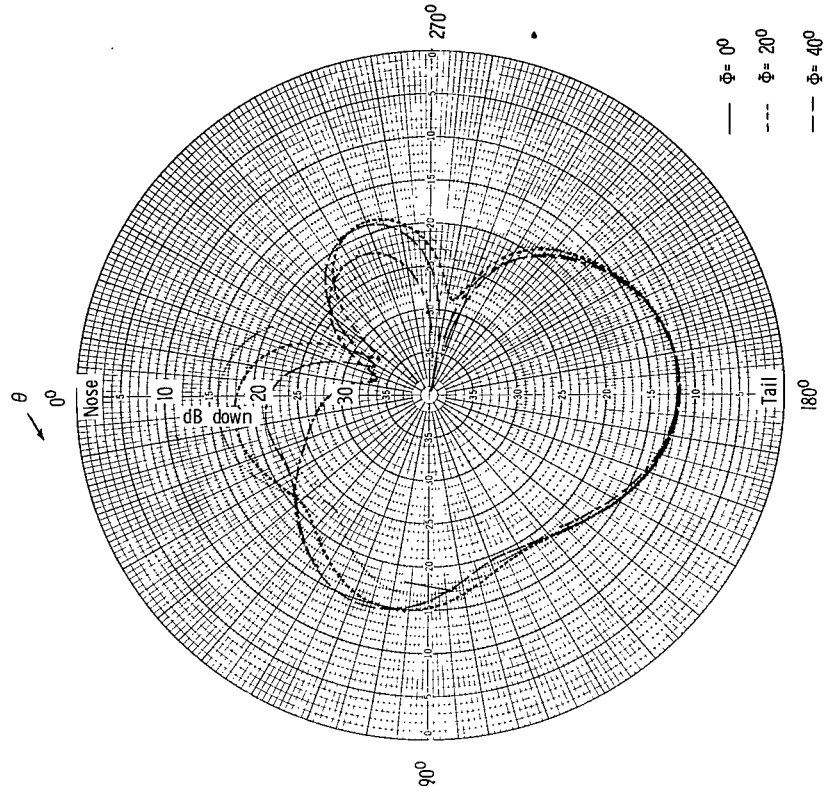

(d) Right-hand circular, $\Phi = 0^{0}$.

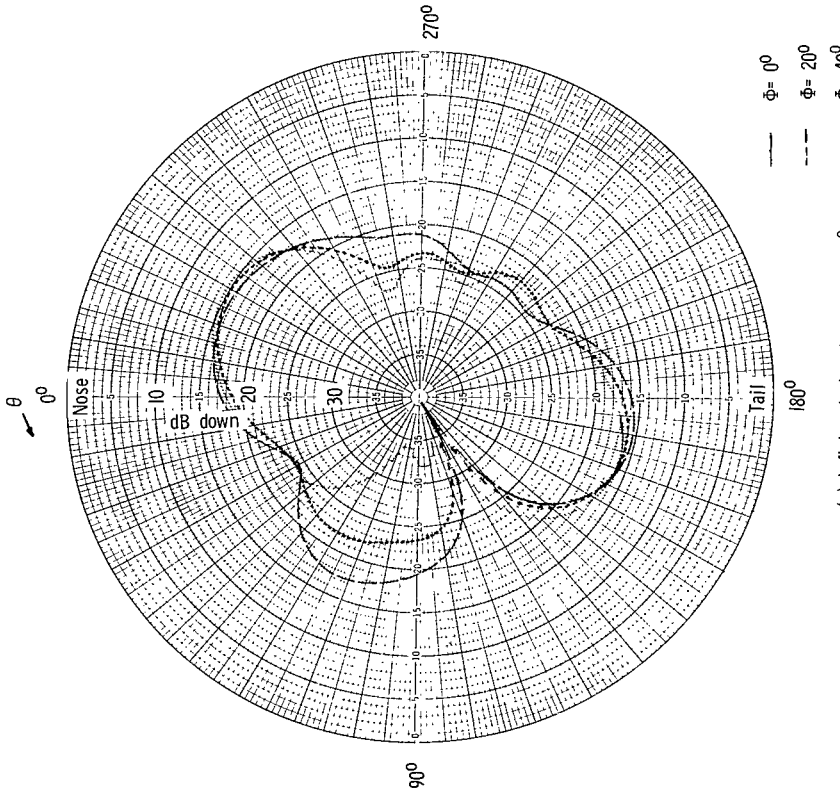

(c) Left-hand circular. $\Phi = 100^{0}$.

Figure A3.- Continued.

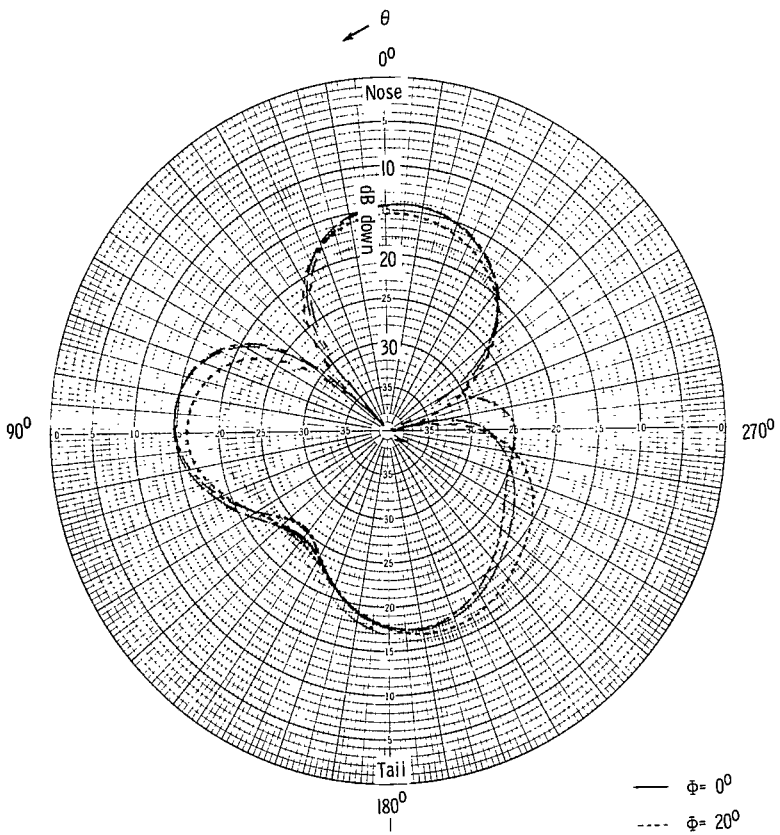

(e) Right-hand circular. $\Phi = 50^{0}$.

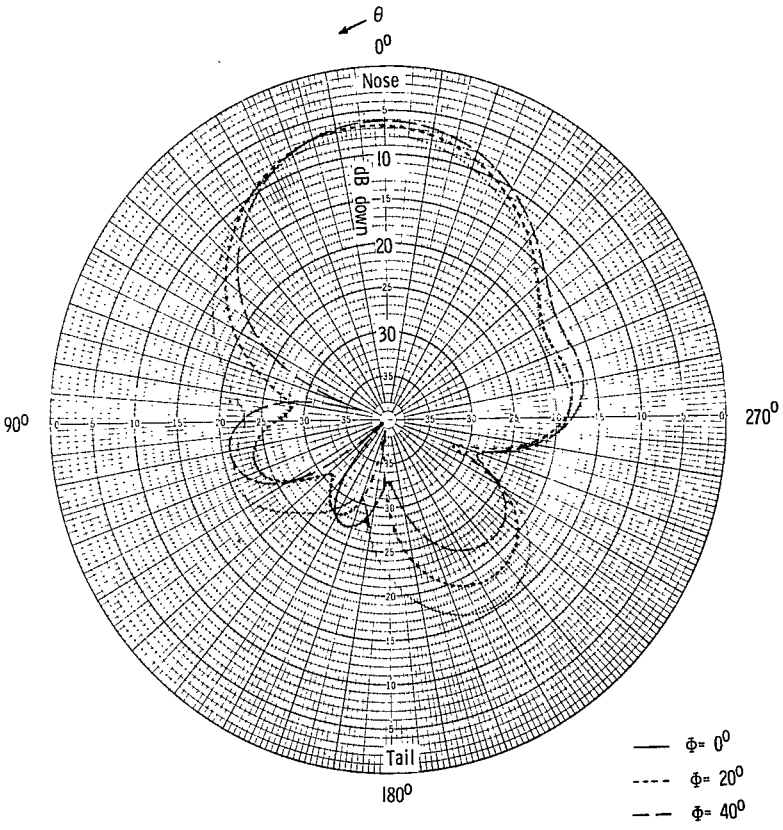

(f) Right-hand circular. $\Phi = 100^{0}$.

Figure A3.- Concluded.

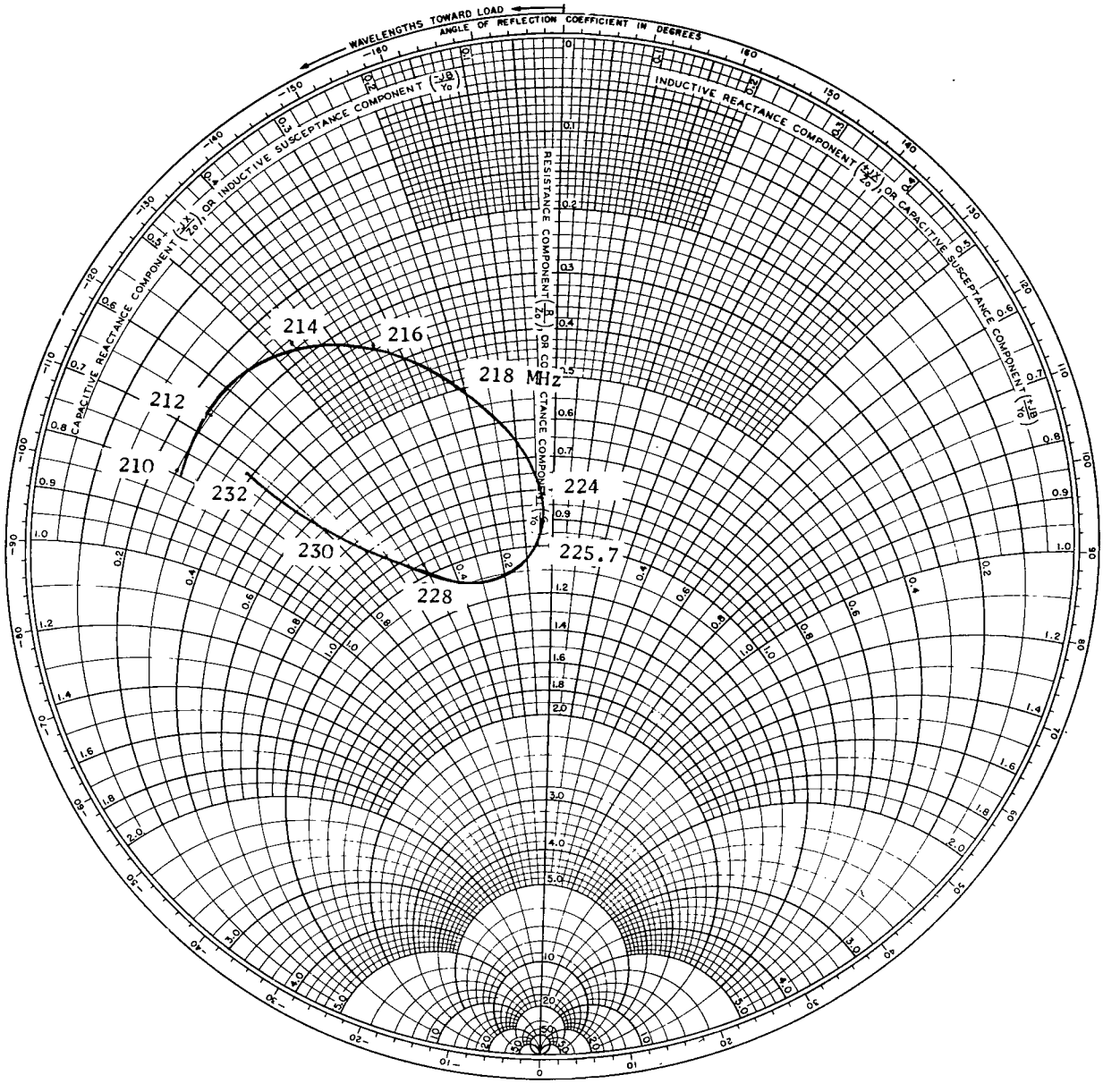

(a) Impedance.

Figure A4.- Final performance characteristics of delayed-time telemetry antenna (free space).

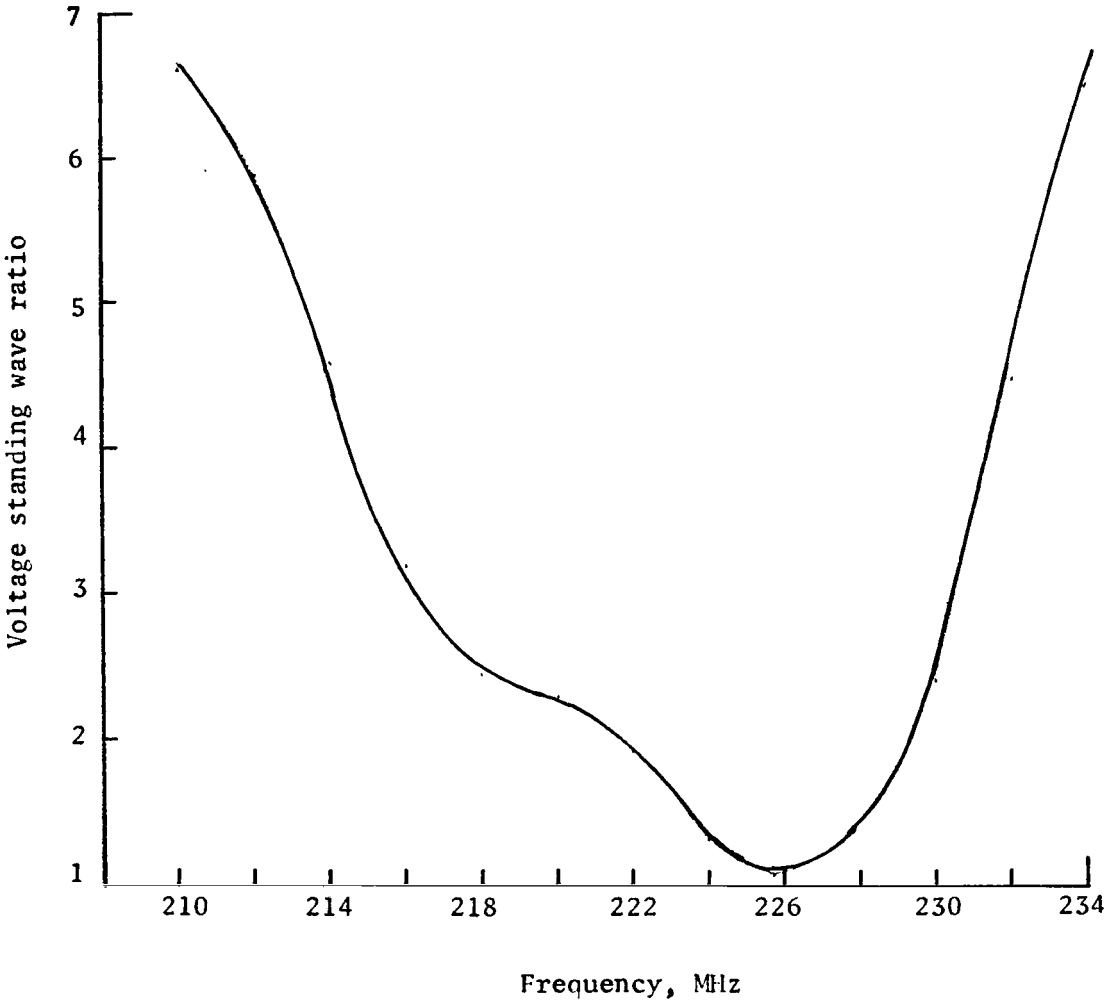

(b) Voltage standing wave ratio.

Figure A4.- Concluded.

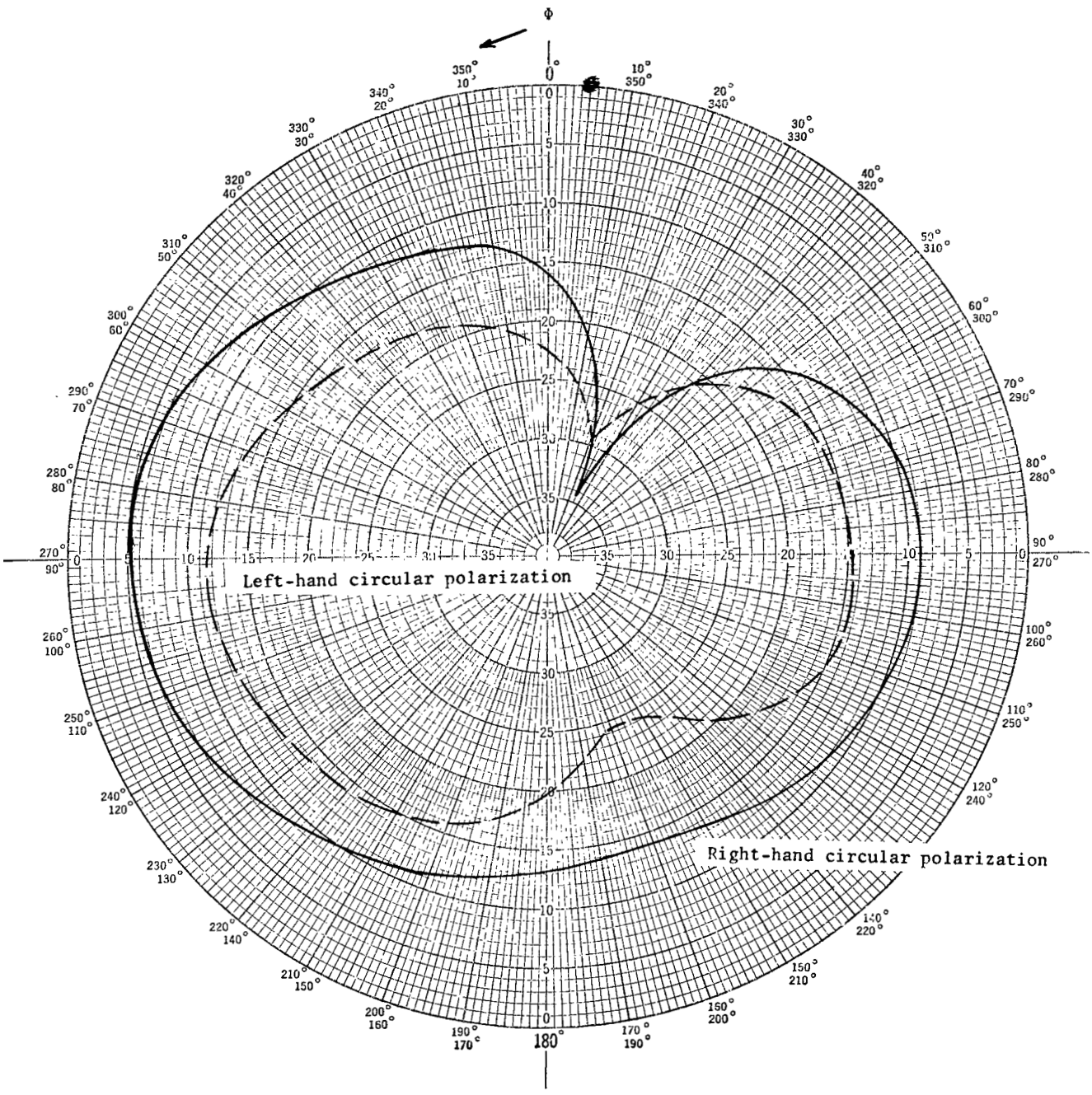

Figure A5.- Equatorial plane radiation patterns of delayed-time telemetry antenna (free space). Isotropic level at the 6-dB circle; $\theta = 90^{0}$; f = 225.7 MHz.

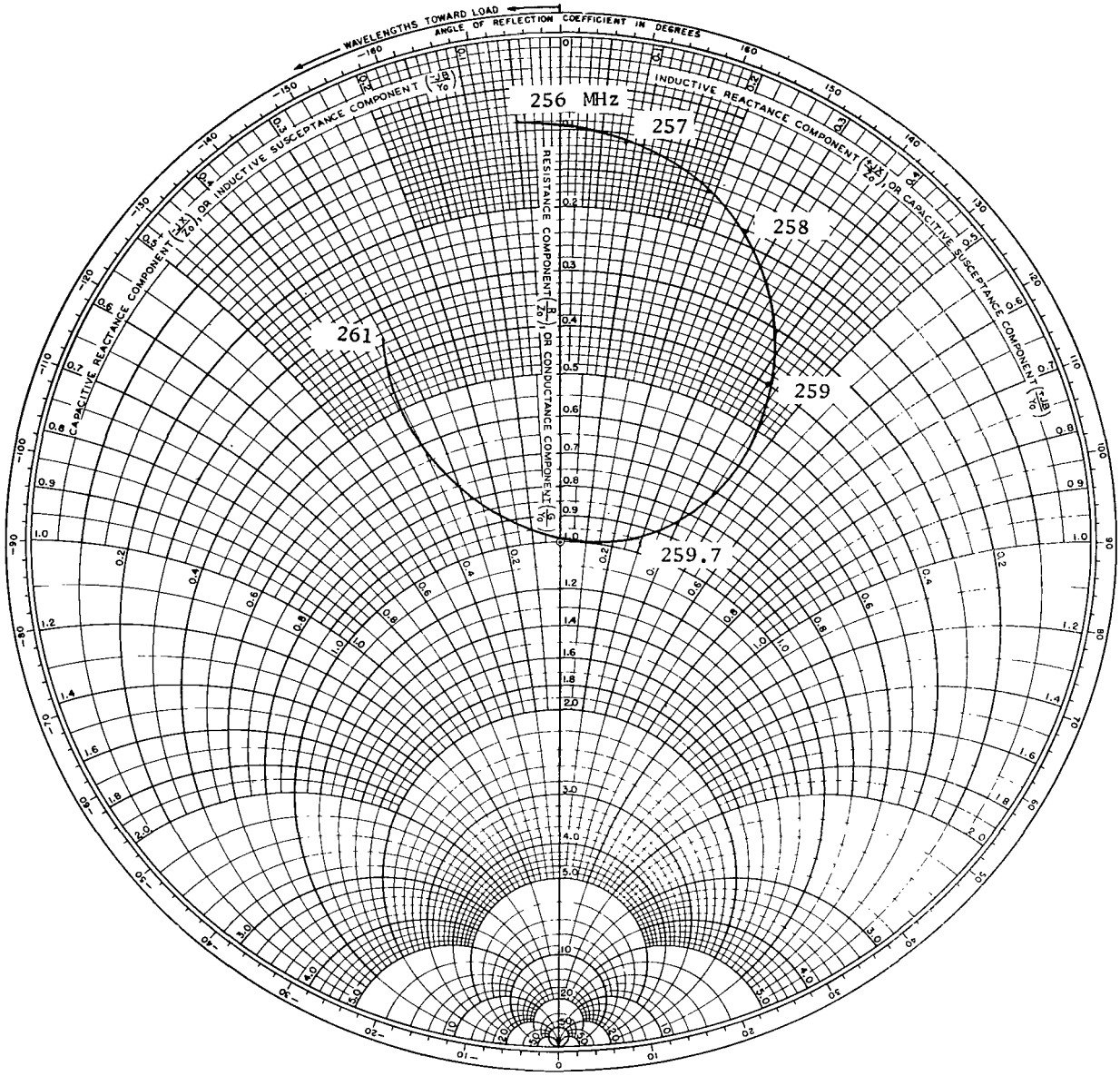

(a) Impedance.

Figure A6.- Final performance characteristics of direct-time telemetry antenna (free space).

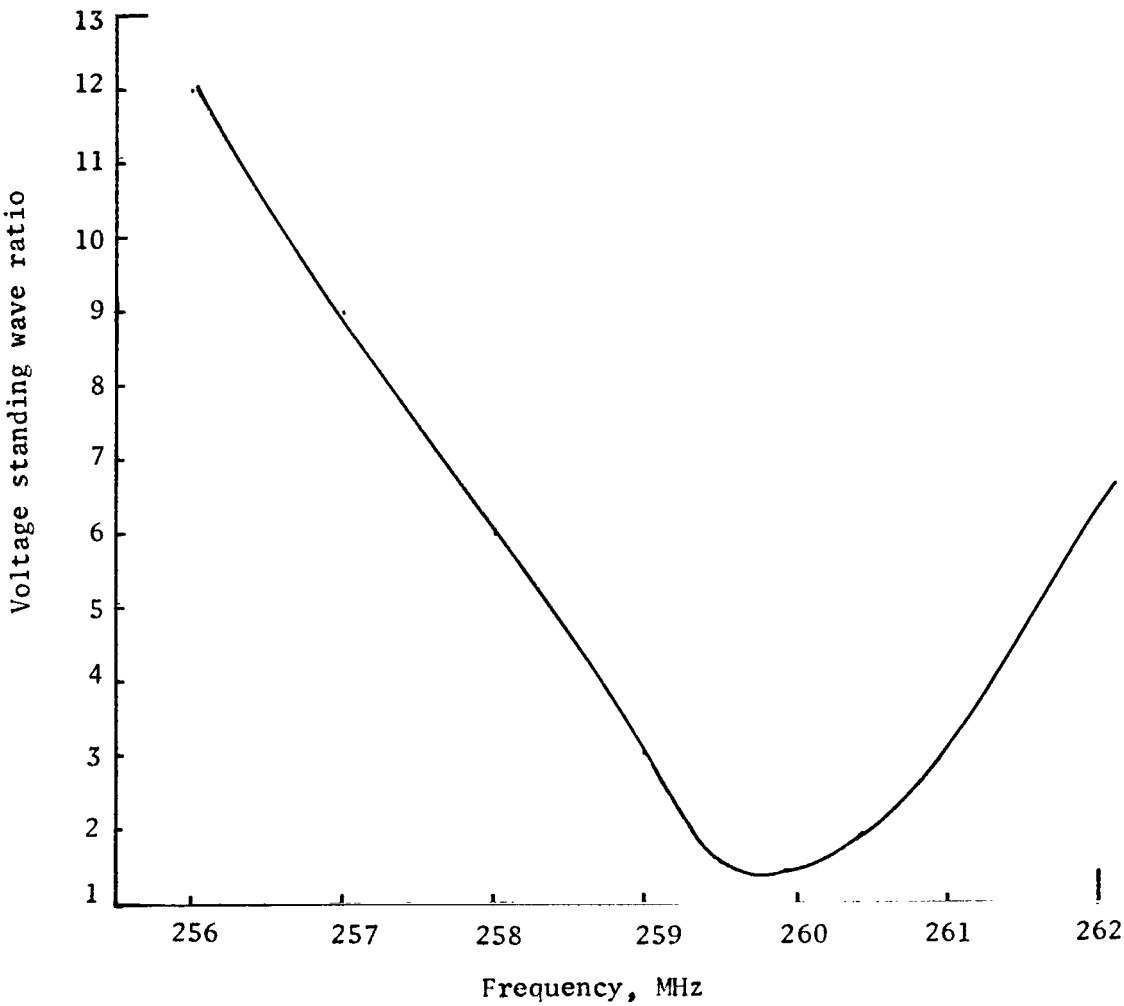

(b) Voltage standing wave ratio.

Figure A6.- Concluded.

APPENDIX A

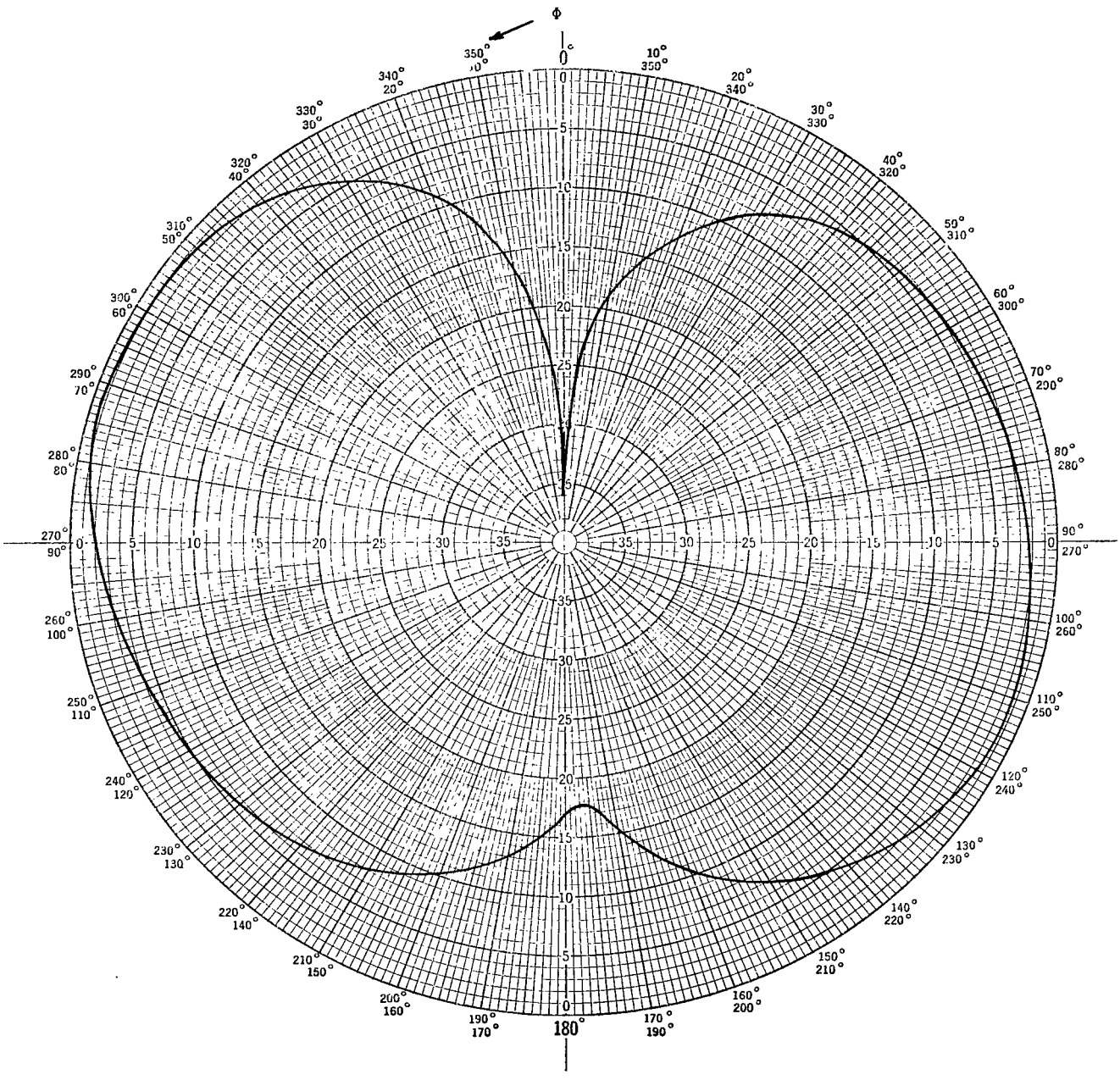

Figure A7.- Equatorial plane radiation pattern of direct-time telemetry antenna (free space).
θ = 90°; f = 259.7 MHz; peak gain, -4 dB.

APPENDIX B

DESIGN AND DEVELOPMENT OF C-BAND AND X-BAND RAM C-I ANTENNAS

By Fred B. Beck

Introduction

The major design considerations for the RAM C-I C-band and X-band antennas are physical size, pattern coverage, and gain. The limitations on physical size are surface area on the circumference of the payload and internal volume. Since the antenna surface area primarily determines the pattern coverage, the antenna apertures were designed to be a compromise of these two parameters. With the antenna aperture dimensions defined, the resultant pattern coverage and gain are primarily determined by leaky surface wave effects (ref. 27) from the ablation coating and efficiency of aperture excitation, respectively.

Preliminary Antenna Design

The first step in the preliminary design procedure for the RAM C-I C-band and X-band antennas was to build a metal mock-up of the payload to be used in conjunction with various antenna test models. The next step was to determine the available payload space for mounting the antennas and their far-field pattern requirements. The final inputs needed for the preliminary design were trajectory information and antenna polarization requirements. The important trajectory parameter at this stage of the design was the aspect angle since this angle dictates the orientation of the far-field patterns. The aspect angle is formed by a line through the nose-to-tail axis of the payload and the line of sight from a receiving station. For the RAM C-I flight, the primary downrange receiving station is Bermuda.

Different test antenna models were designed within the preliminary guidelines of space and mounted in the RAM C-I metal mock-up in specified locations. Horn antennas were chosen rather than some other aperture-type antenna because of their simplicity and because they had been used on previous RAM flights. Since pattern coverage at X-band frequency was required over the entire 360° in the roll plane, an array of four horns was chosen. However, for C-band frequency, only one horn was required for continuous smoothed radar tracking.

After the preliminary design decision to use horns for both the C-band and X-band antenna systems was made, far-field radiation patterns were then measured to determine whether the coverage was compatible with anticipated flight conditions. Examination of these preliminary patterns for both circumferential and axial polarization clearly

demonstrated that circumferential polarization would not be acceptable for the four-horn X-band array. The reason for the unacceptability of the X-band circumferential polarization was the occurrence of deep nulls around the entire 360° of the roll pattern. Although either vertical or horizontal polarization gave a satisfactory C-band pattern, the downrange C-band tracking radar could receive only vertical polarization, which dictated that the C-band payload polarization be circumferential.

Once the preliminary X-band and C-band antenna design, including the choice of polarization, was completed, effort was then channeled toward refinements of the basic design. In order to make these refinements, trajectory information and a payload mock-up including the teflon heat shield were required. By using the mock-up with heat shield, more meaningful pattern and standing wave ratio measurements were made and incorporated into a final design.

Trajectory Parameters

The reentry trajectory parameters used in the final design of the C-band and X-band antennas are given in figure B1. The variation of altitude, velocity, elevation angle, aspect angle, and heat-shield ablation rate with time from lift-off in seconds is given in figure B2. From the standpoint of antenna design, the two most important of these parameters are aspect angle and heat-shield ablation rate. The aspect angle of the trajectory dictates the orientation of the antennas with respect to the spacecraft axis. Since the aspect angle is approximately 90° as the payload passes Bermuda, the antennas should have radiation patterns favoring the side rather than the nose or tail of the payload. The heat-shield ablation rate has an important effect on the matching of the antennas and on radiation patterns due to trapped energy in the ablative material.

Antenna Voltage Standing Wave Ratio

A major contribution to a high VSWR on flight vehicles is frequently the impedance mismatch caused by the dielectric heat shield covering the antennas. The method commonly used to decrease the VSWR of horn antennas is to insert a proper size dielectric plug into the throat of the aperture. However, since the protective heat shield ablates during reentry, some detuning effects are still expected to occur. Therefore, the dielectric plug should be designed to allow some detuning before and after the ablation period. The heat-shield thickness on the RAM C-I before ablation is approximately 0.31 in. (0.79 cm) at the location of the C-band and X-band antennas. After ablation, the thickness is calculated to be approximately 0.11 in. (0.28 cm); this indicates that 0.2 in. (0.51 cm) of the heat shield will ablate during reentry.

The E-plane and H-plane views of the C-band horn antenna and the location of the teflon matching plug are shown in figure B3. The matched condition for the horn occurs

for a teflon thickness equal to a multiple of dielectric half-wavelengths. Since 0.2 in. (0.51 cm) of the heat shield ablates during reentry, the plug plus heat shield and bonding agent should be designed 0.1 in. (0.25 cm) greater than the matched condition.

The variation of the VSWR with frequency of the C-band horn antenna on the RAM C-I is presented in figure B4. Note that the VSWR over the frequency range from 5.40 GHz to 5.8 GHz is always less than the maximum desirable preflight value of 2 to 1. Since the horn has approximately 0.1 in. (0.25 cm) more teflon covering than is required for a matched condition, the horn is expected to become matched when 0.1 in. of the heat shield has ablated.

In designing the X-band matching plugs extra care was deemed necessary because 0.2 in. (0.51 cm) of teflon approaches $\frac{1}{4}\lambda$ at the design frequency of 9.21 GHz. This thickness is a sufficient amount to mismatch the horns if the plugs are not designed properly. A drawing of the flight X-band horn antenna with matching plug is shown in figure B5.

The variation of VSWR with frequency of the four-horn-array X-band antenna on the RAM C-I is shown in figure B6. The total thickness of the matching plug, heat shield, and bonding agent on the flight payload is approximately 0.94 in. (2.39 cm). This thickness is approximately 0.06 in. (0.15 cm) greater than 1λ in the dielectric. Since the X-band horns are designed primarily for the reentry data period and the total 0.2-in. (0.51 cm) heat-shield ablation does not all occur during this time, less overdesign for the matching plugs of the X-band horn is required than for the matching plugs of the C-band horn.

Once the C-band and X-band matching plugs are designed and incorporated into the flight payload, no further refinements should be required unless the far-field patterns have changed so that they are no longer acceptable for flight.

Far-Field Patterns of C-Band Antenna

Antenna patterns were measured for different aspect angles varying from 0° to 180°. These patterns for various aspect angles are shown in figure B7. The payload top is at $\phi = 0^{\circ}$ with all patterns measured over 360° in the roll plane of the model. Note that the level of the patterns increases with an increase in aspect angle up to 80° and then decreases as the aspect angle is increased further. The reason for the symmetry around an aspect angle of 80° instead of 90° is the approximate 10° half-angle of the cone-shaped payload. For tracking purposes, the patterns in figure B7 appear very adequate except for aspect angles near 0° and 180°, which are never encountered at Bermuda.

The curve in figure B8 gives a better idea of how the maximum pattern level varies with aspect angle. The peak gain of the horn is 7.5 dB above the isotropic level.

Far-Field Patterns of X-Band Antenna

Some typical X-band patterns measured on the RAM C-I are shown in figure B9. Each plot is a 360^{o} roll-plane pattern for a specific aspect angle. The aspect angle, starting with 0^{o}, is increased in increments of 10^{o}. For all the roll-plane patterns, the payload top is at $\phi = 0^{o}$.

An important observation to make about most of the patterns in figure B9 is the number and magnitude of the peaks and nulls that occur in the roll plane. These variations are due to individual pattern overlap and leaky surface waves radiating around the periphery of the payload. If the payload was not covered with a layer of teflon, the individual pattern overlap would be the only contributor to the peaks and nulls. Also, the deep variations would occur primarily in the regions between any two adjacent horns. However, since a layer of teflon is attached for thermal protection, variations also occur which can be attributed to leaky surface waves. Leaky surface waves (ref. 28) can exist for a dielectric skin thickness of zero. The equation for the different modal cutoff thicknesses t (in wavelengths) is

$$t = \frac{n}{4\sqrt{\epsilon - 1}}$$

where n is an integer representing the mode number and ϵ is the dielectric constant. Since the dielectric constant of teflon is 2.1, $t = 0.238n$. Due to the boundary conditions, only the even TM (transverse magnetic) and the odd TE (transverse electric) modes can exist. Therefore, at 9.21 GHz and a teflon skin thickness of 0.31 in. (0.79 cm), only the TM_0 and the TE_1 leaky wave modes can exist. The cutoff thickness for the TE_1 mode at 9.21 GHz is approximately 0.305 in. (0.77 cm). Thus, with more than 0.005 in. (0.013 cm) of heat-shield ablation, the TE_1 leaky surface wave mode can no longer be excited. The TM_0 mode never cuts off except for a heat-shield thickness of zero.

The effects of leaky surface wave radiation can also be observed in the cross-polarized component of the far-field pattern. Measured patterns depicting the cross-polarized components are shown in figure B10. These patterns were measured in the same manner as those in figure B9 except for the polarization change. The high magnitude of the patterns demonstrates that considerable cross-polarized energy is coupled out of the leaky surface waves; this should not cause undue concern, since it is possible to use the cross-polarized component to advantage. With a polarization diversity ground station, the cross-polarized component can be used to fill in many nulls in the dominantly polarized pattern. An illustration of what should be recorded with a polarization diversity system is shown in figure B11.

APPENDIX B

Concluding Remarks

The trajectory for the RAM C-I experiment was very compatible with reception of a strong signal from the payload during the prime data period of the mission. The high level of pattern reception was due primarily to an aspect angle near 90^{o} for much of the flight during prime data transmission.

Problems encountered in antenna design were mostly those of a minor nature such as the X-band matching plug and effects of leaky surface waves on far-field patterns. Since the matching plugs were designed properly, no serious detuning due to heat-shield ablation was expected from either the X-band or C-band antennas unless considerably more than 0.2 in. (0.51 cm) of teflon is lost during reentry. The leaky surface wave problem was overcome by choosing the proper polarization for the payload. On the basis of the results obtained during this flight, the antenna designs were adequate.

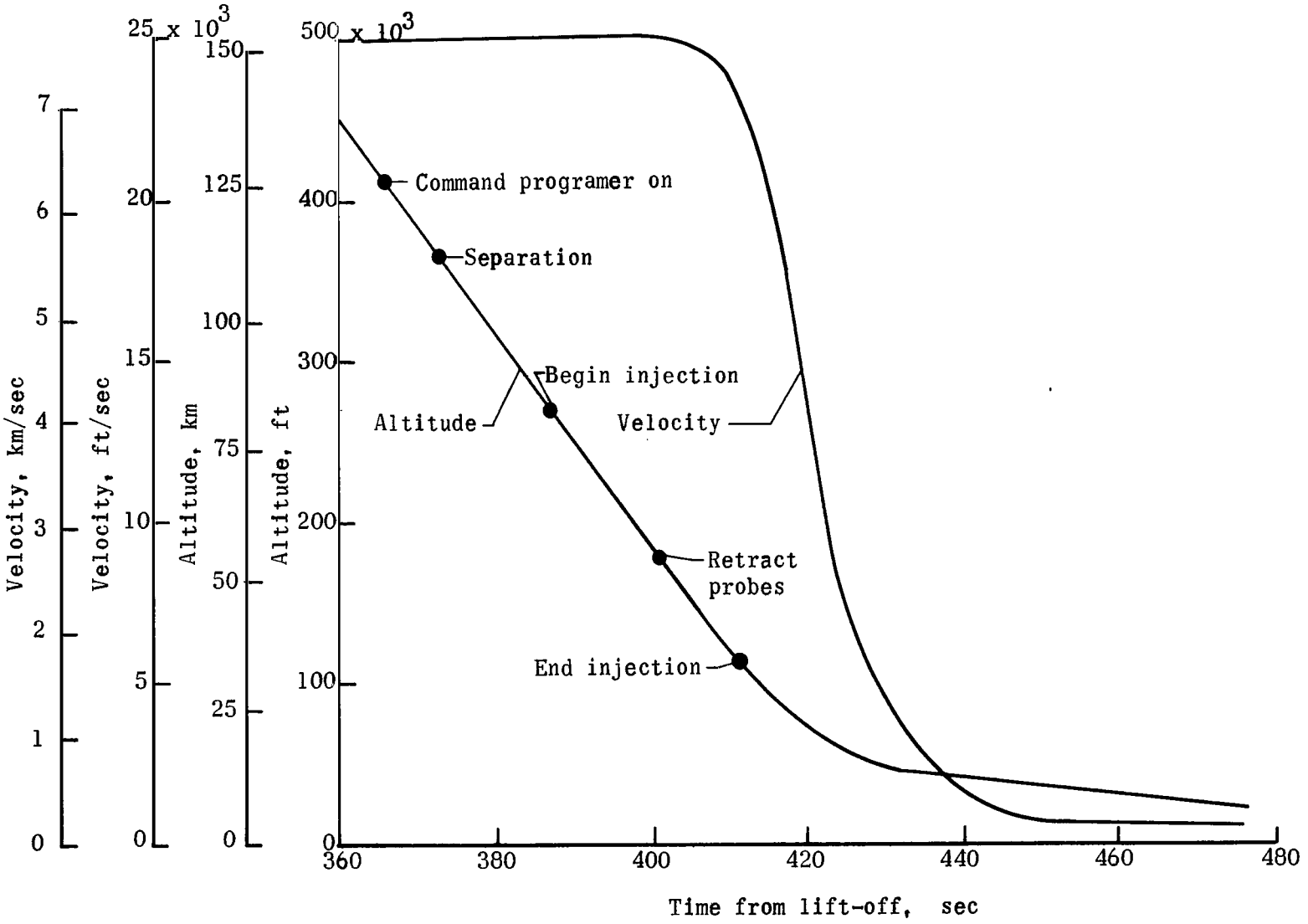

Figure B1.- RAM C-I reentry trajectory.

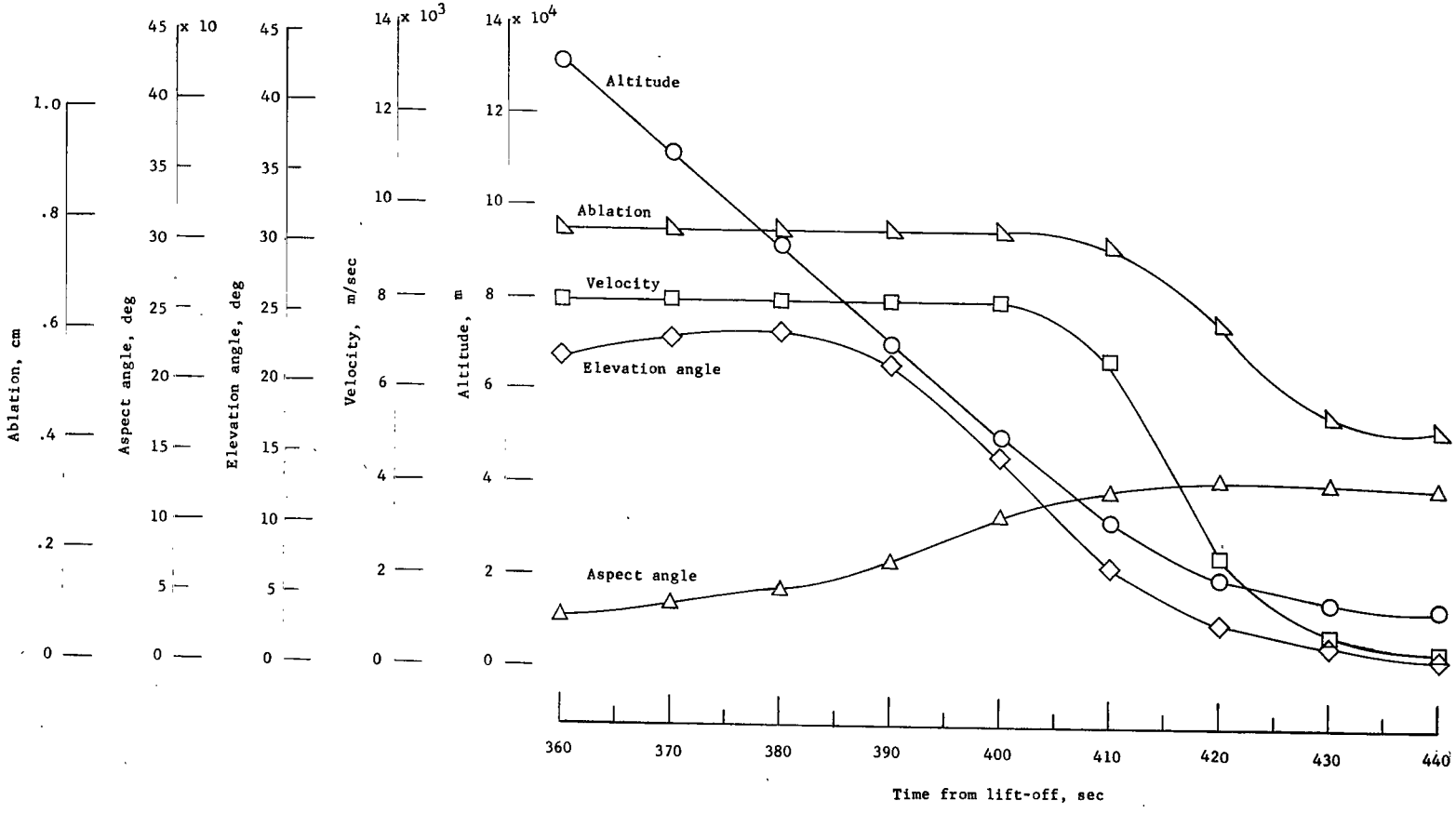

Figure B2.- Variation of RAM C-I altitude, velocity, elevation angle, aspect angle, and ablation rate with time from lift-off.

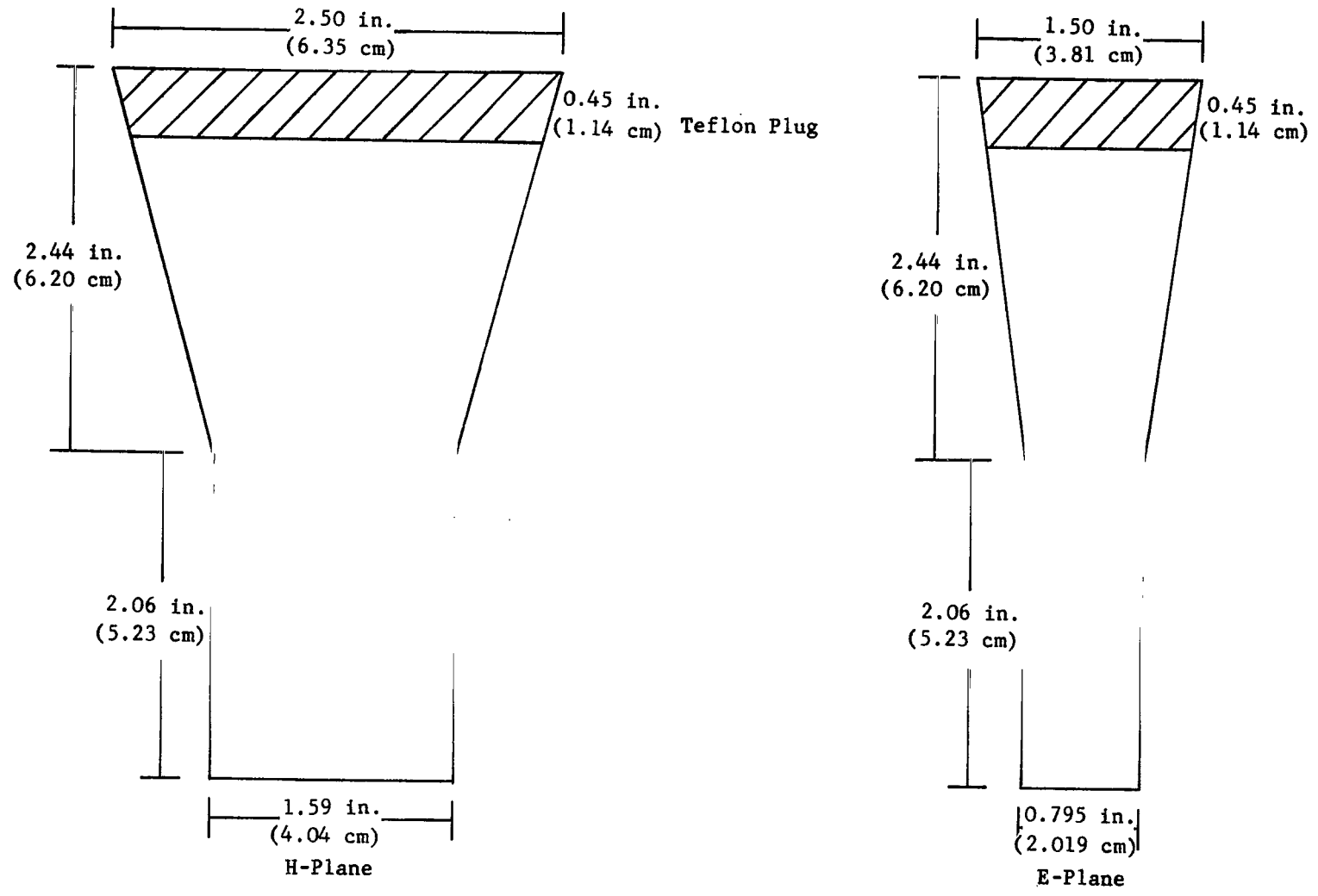

Figure B3.- C-band horn antenna on RAM C-I.

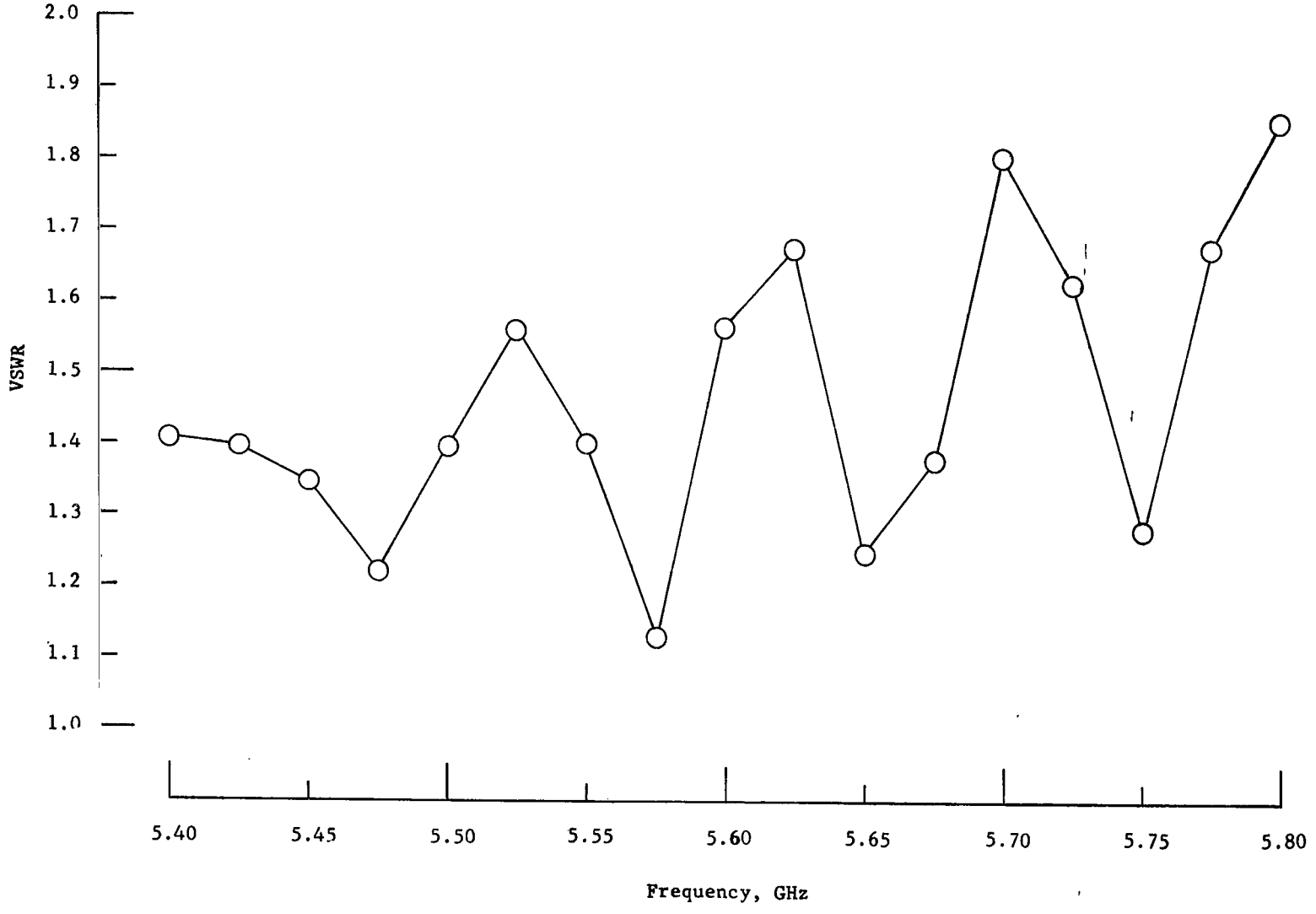

Figure B4.- Variation of voltage standing wave ratio with frequency of the C-band horn antenna.

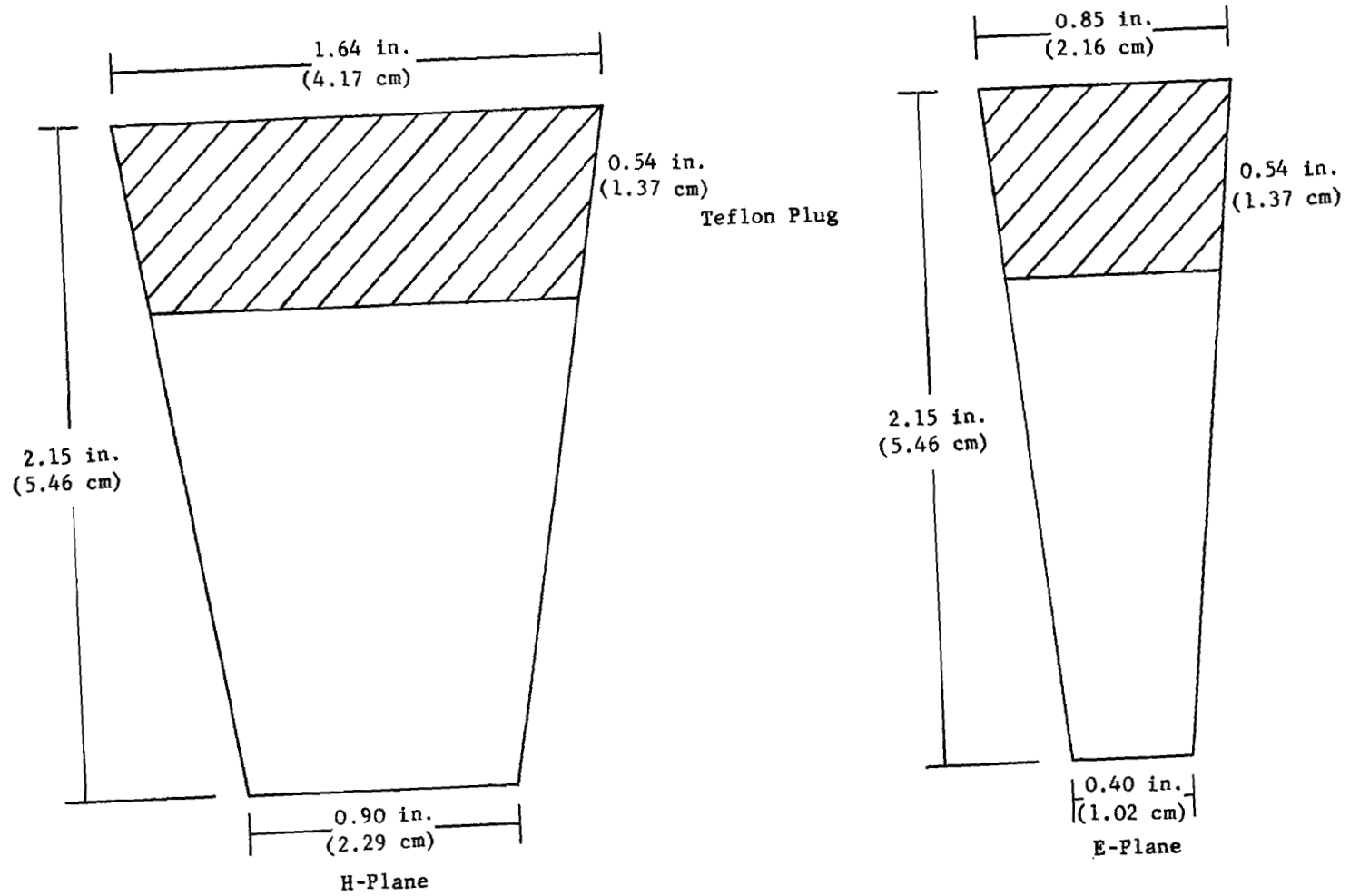

Figure B5.- X-band horn antenna on RAM C-I.

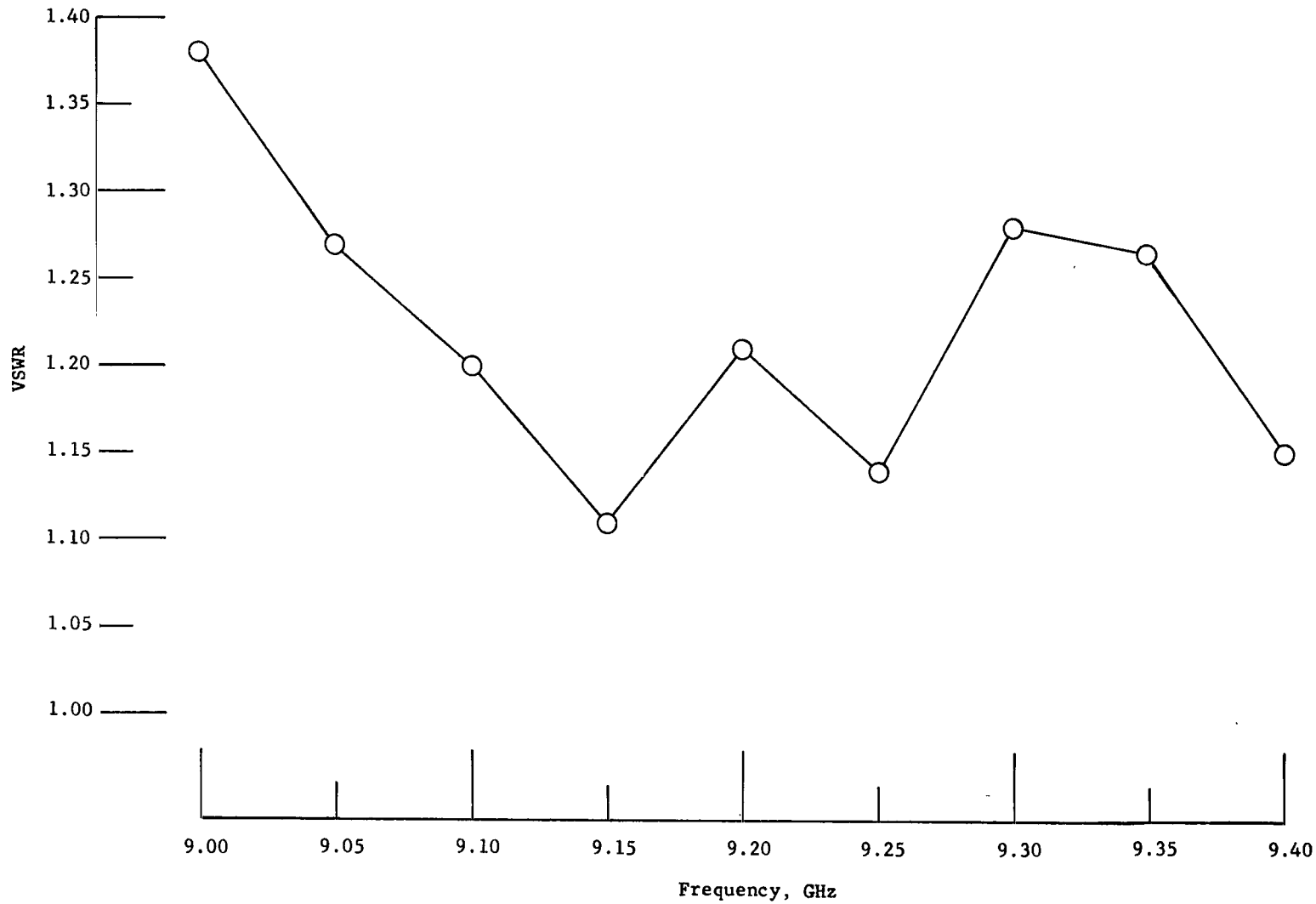

Figure B6.- Variation of voltage standing wave ratio with frequency of four-horn-array X-band antenna.

APPENDIX B

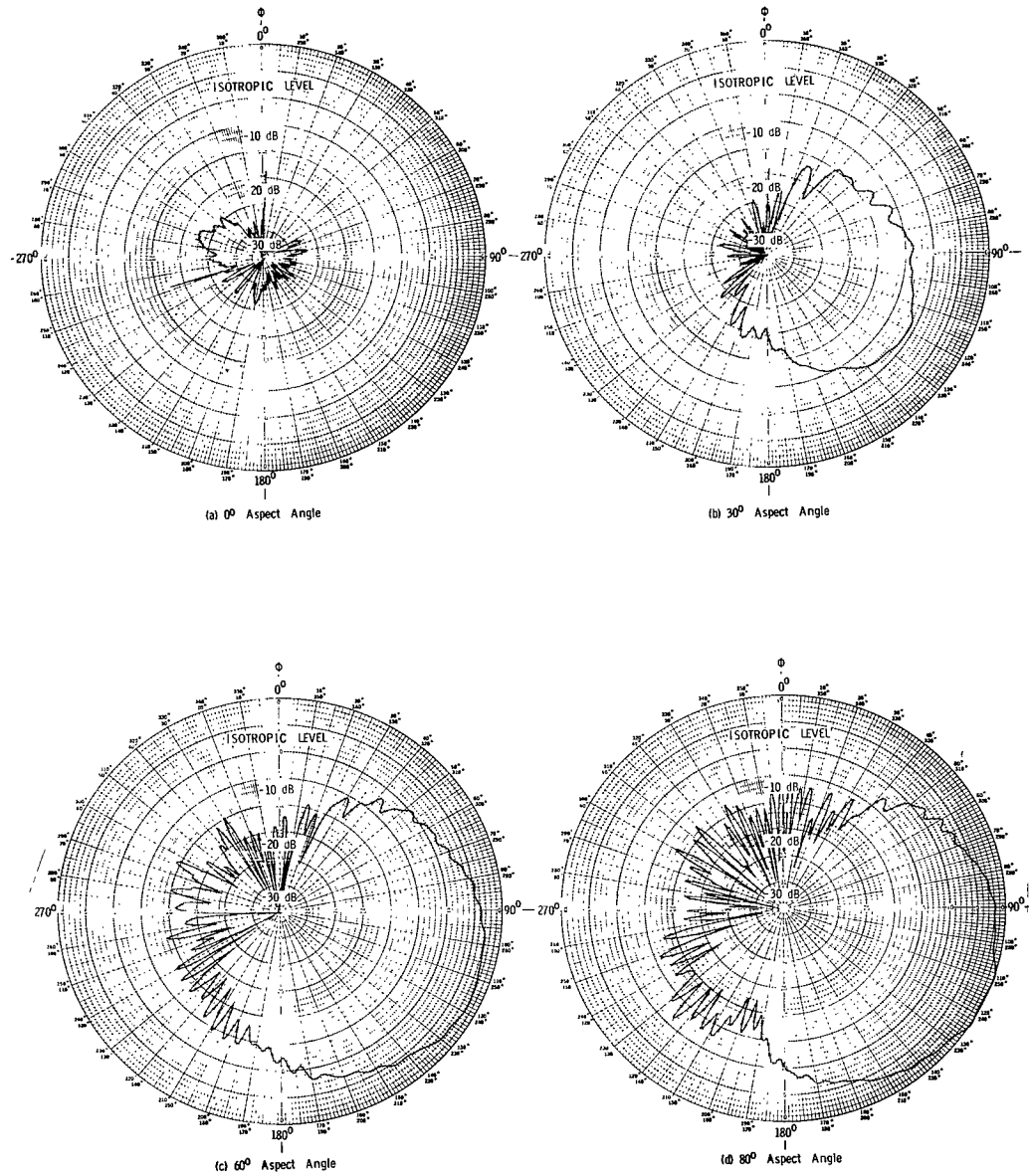

Figure B7.- Measured C-band roll-plane antenna patterns for various aspect angles.

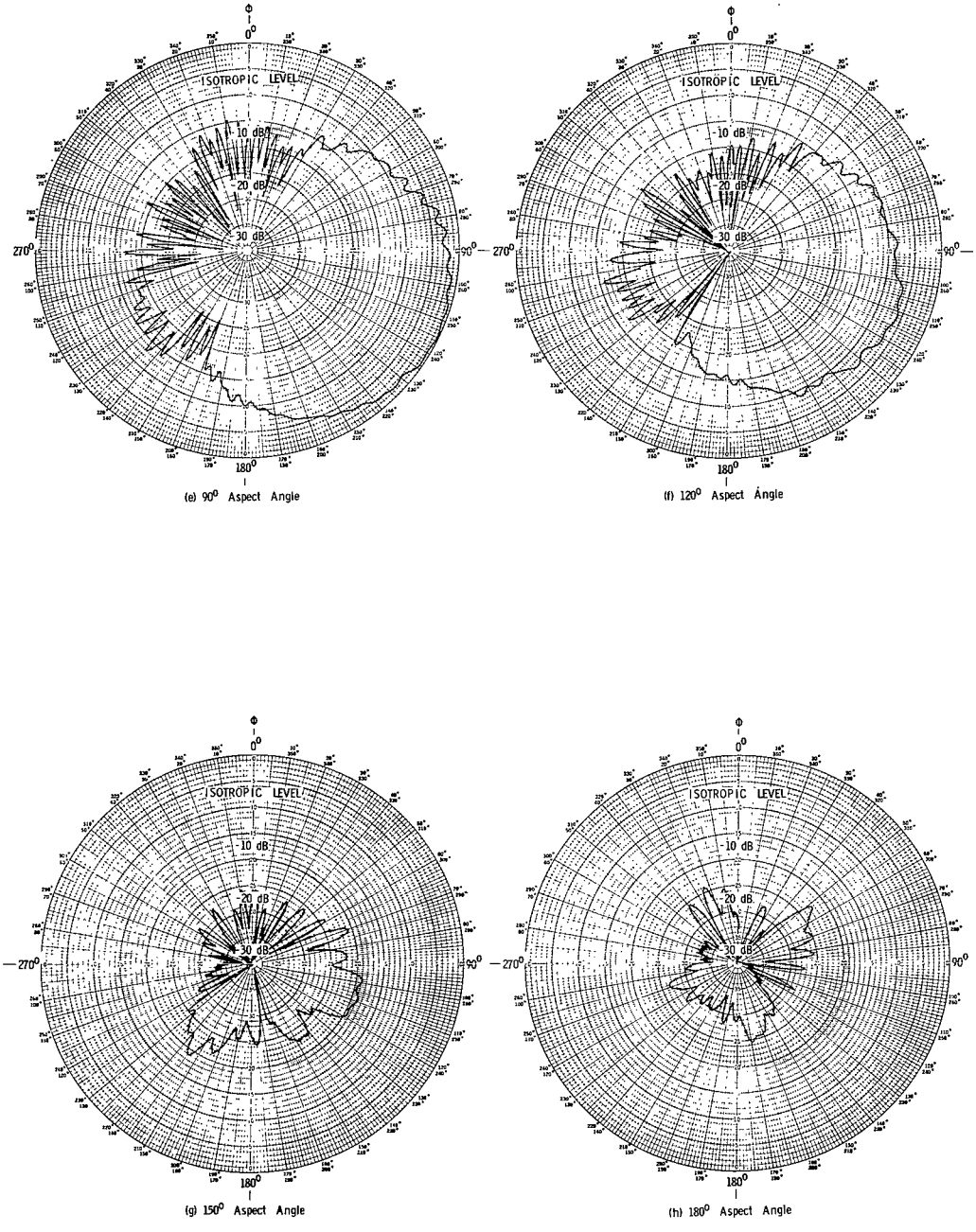

(e) 90° Aspect Angle

(f) 120° Aspect Angle

(g) 150° Aspect Angle

(h) 180° Aspect Angle

Figure B7.- Concluded.

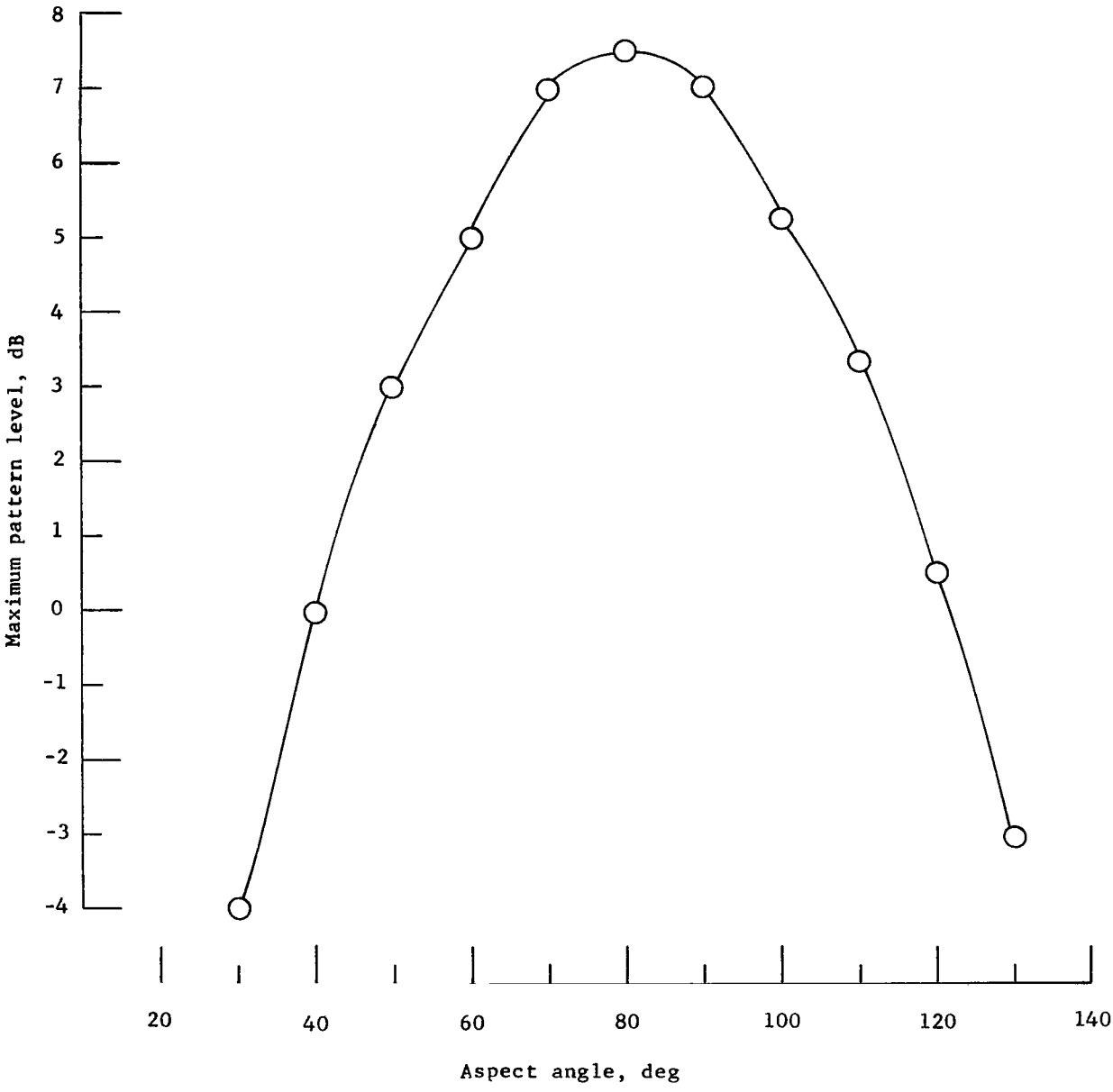

Figure B8.- Variation of maximum pattern level with aspect angle of C-band horn antenna.

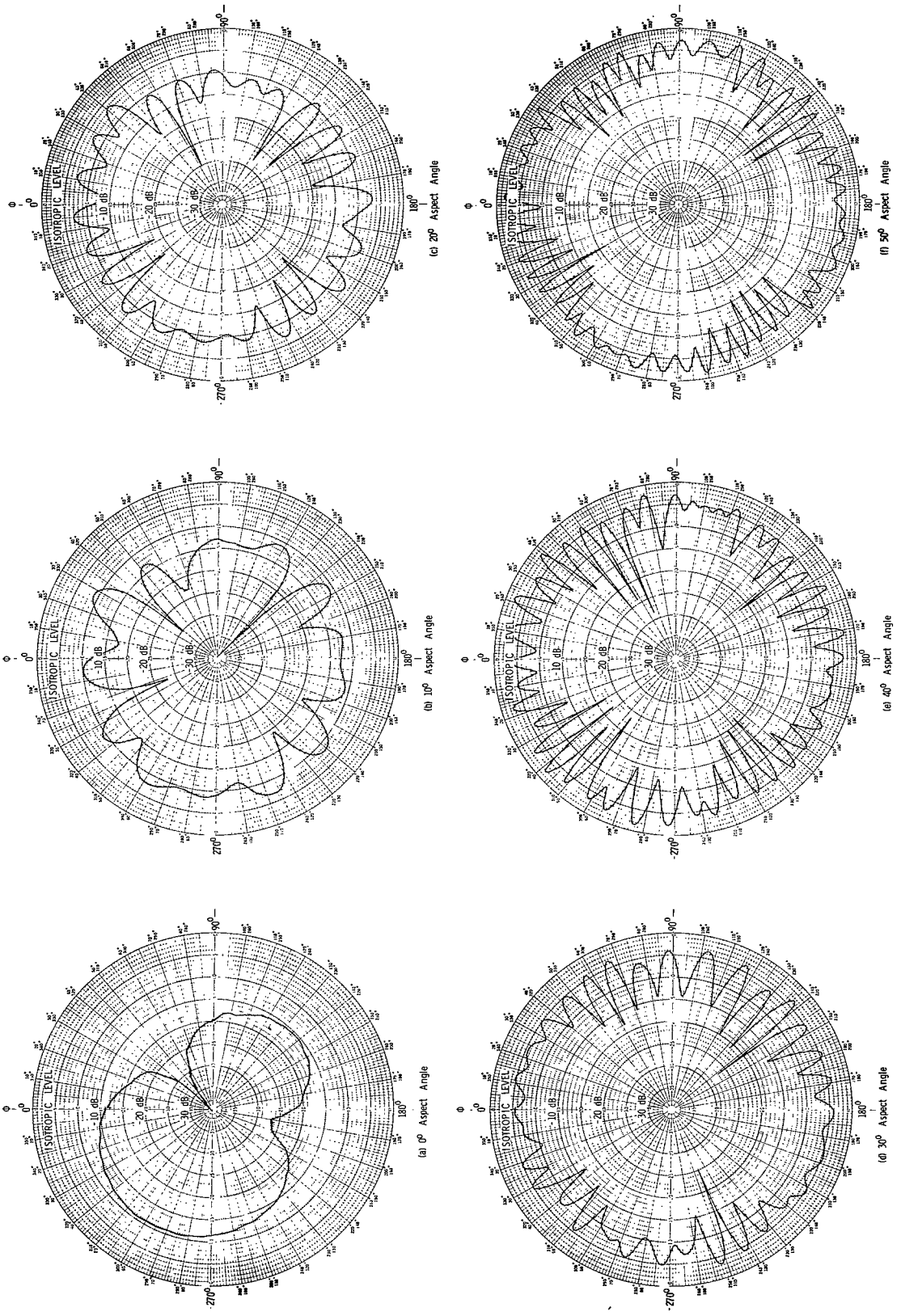

Figure B9.- Measured X-band roll-plane antenna patterns for various aspect angles.

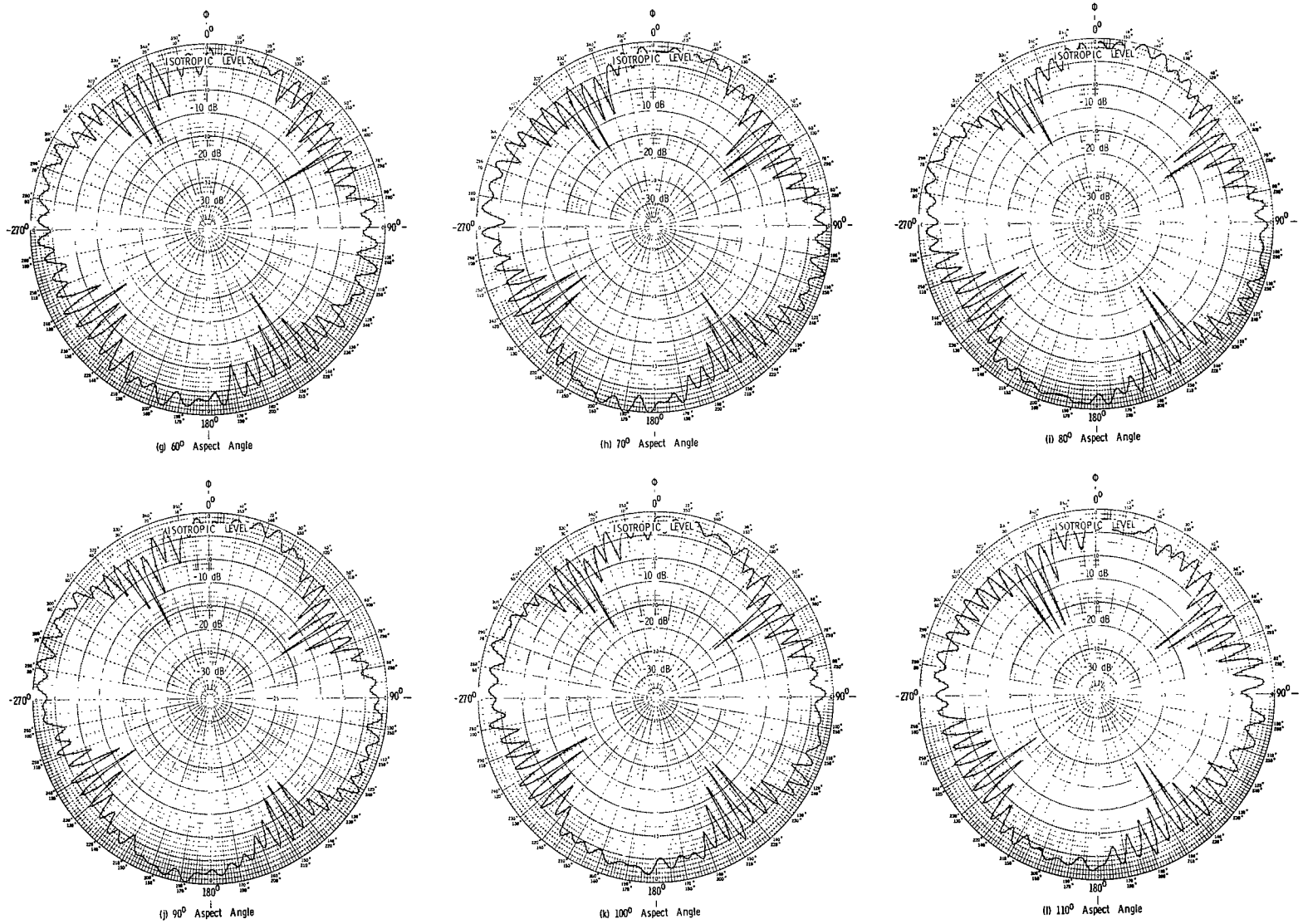

(g) 60° Aspect Angle

(h) 70° Aspect Angle

(i) 80° Aspect Angle

(j) 90° Aspect Angle

(k) 100° Aspect Angle

(l) 110° Aspect Angle

Figure B9.- Continued.

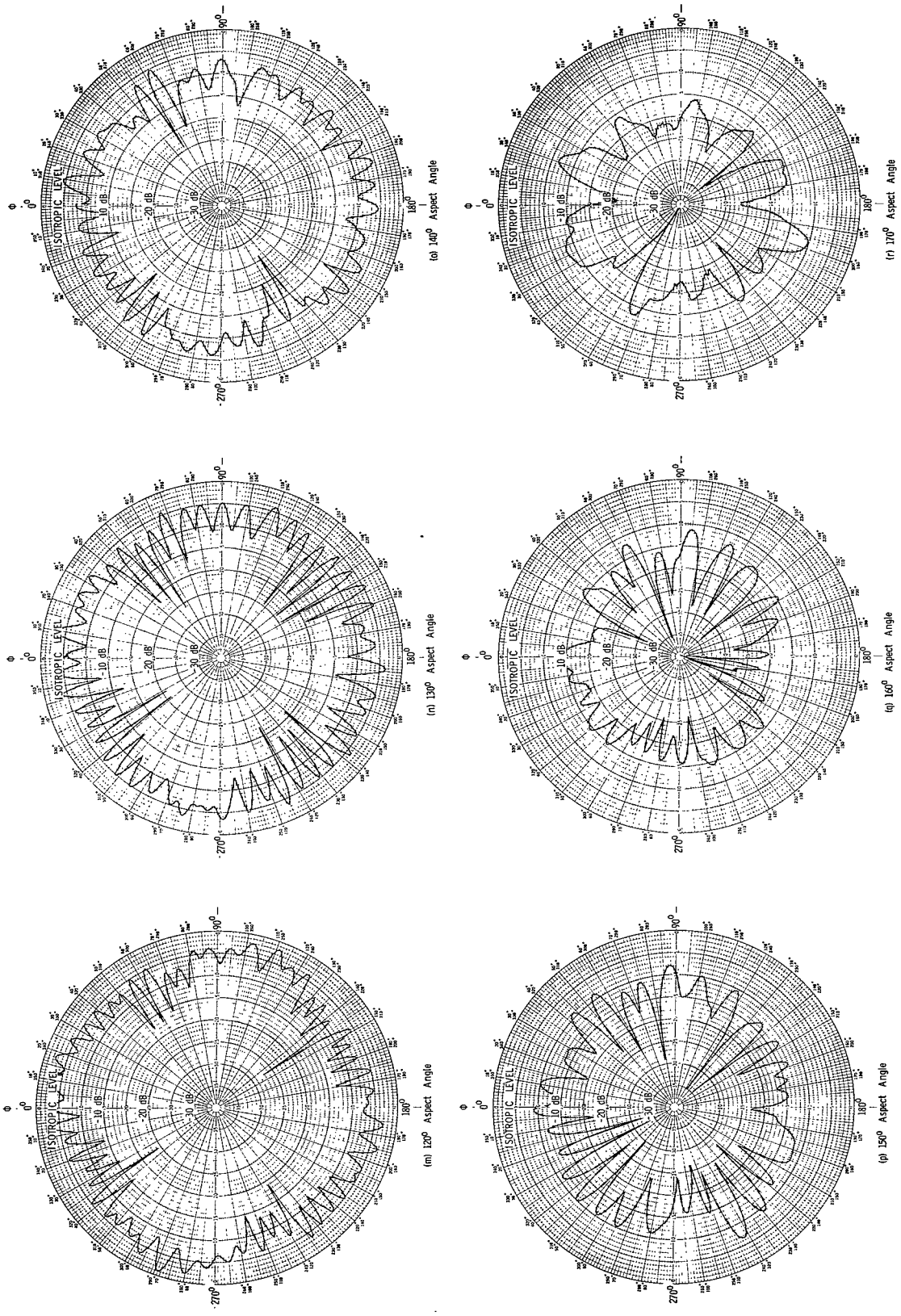

Figure B9.- Concluded.

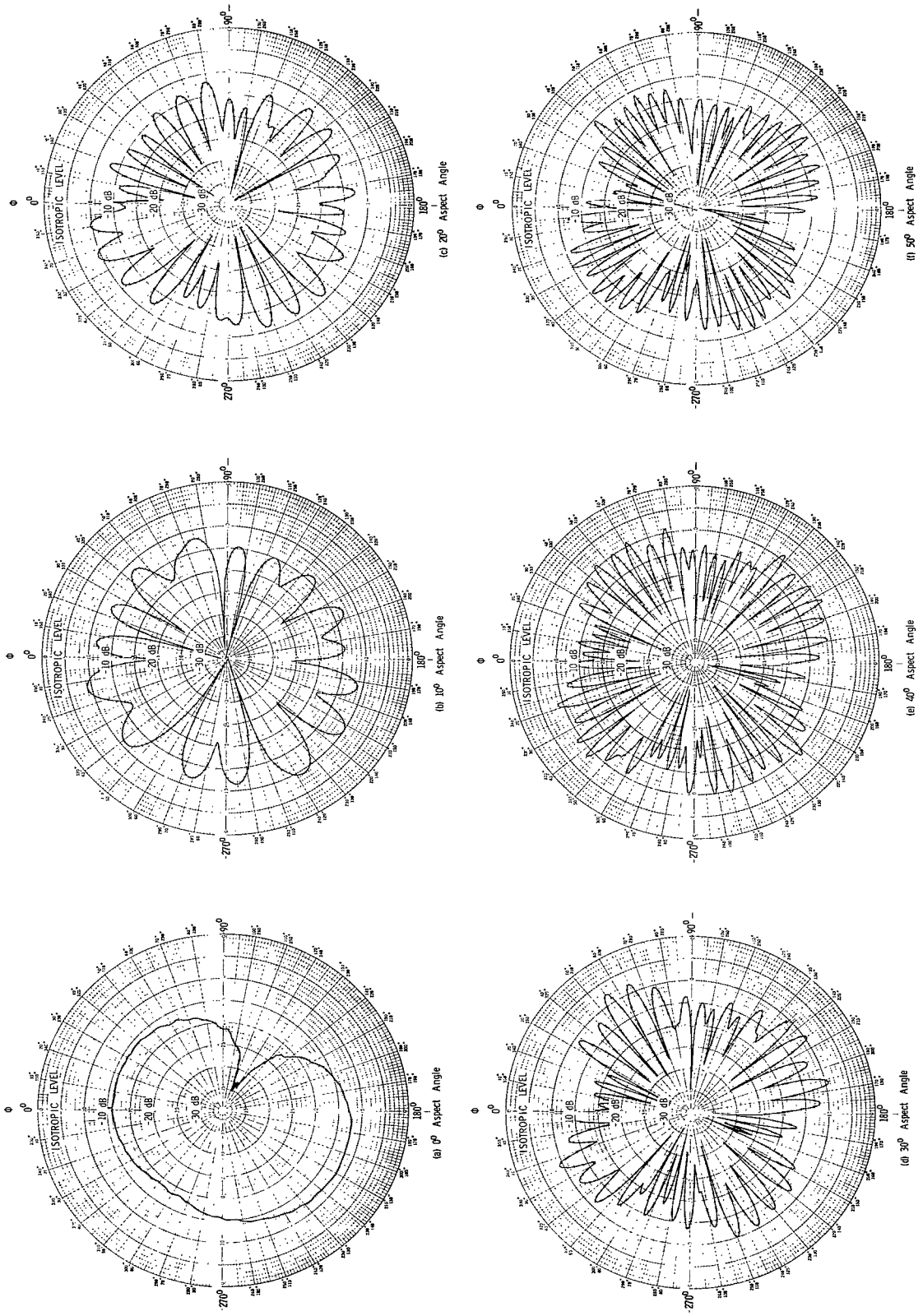

Figure B10.- Cross-polarized X-band roll-plane antenna patterns for various aspect angles.

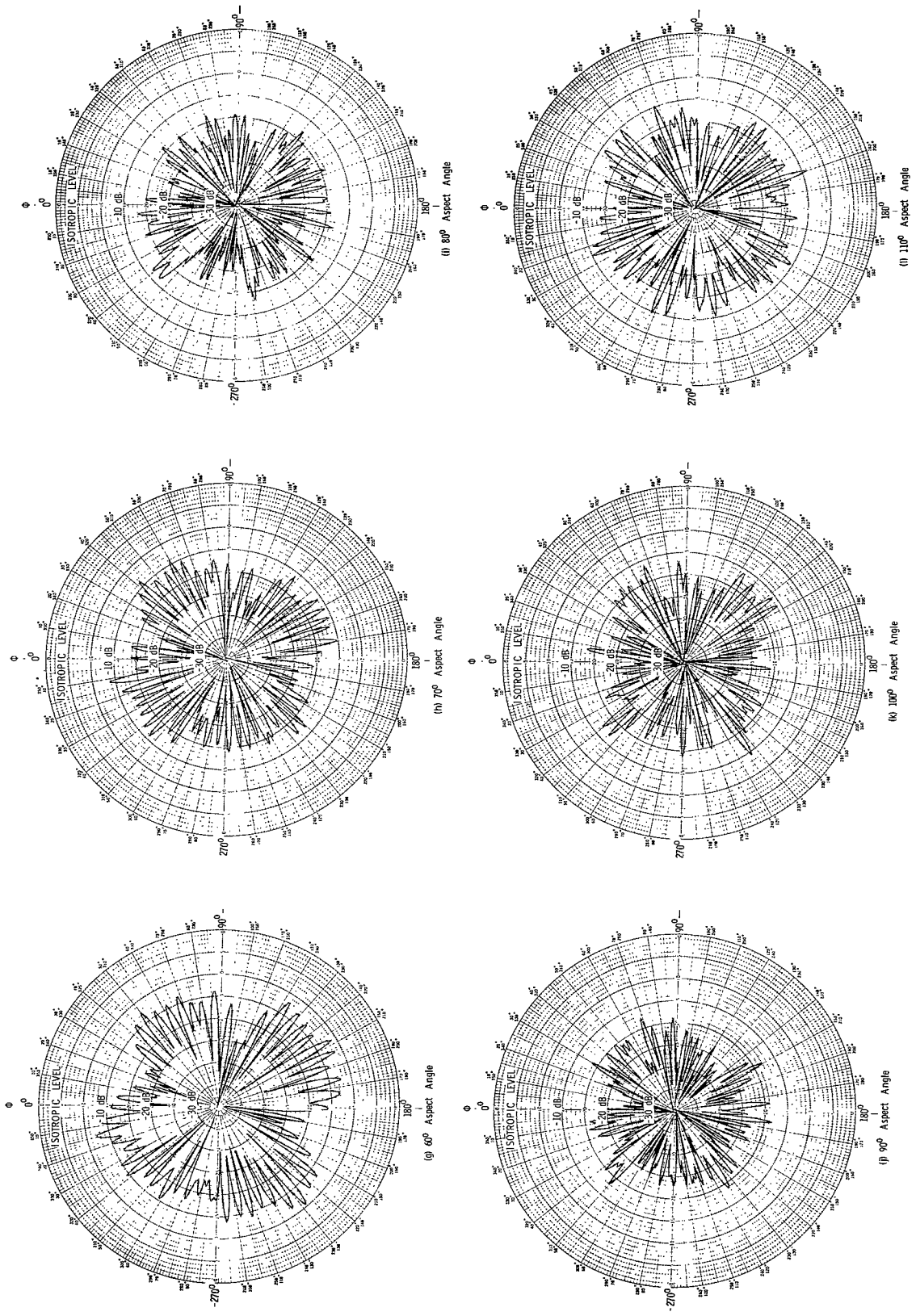

Figure B10.- Continued.

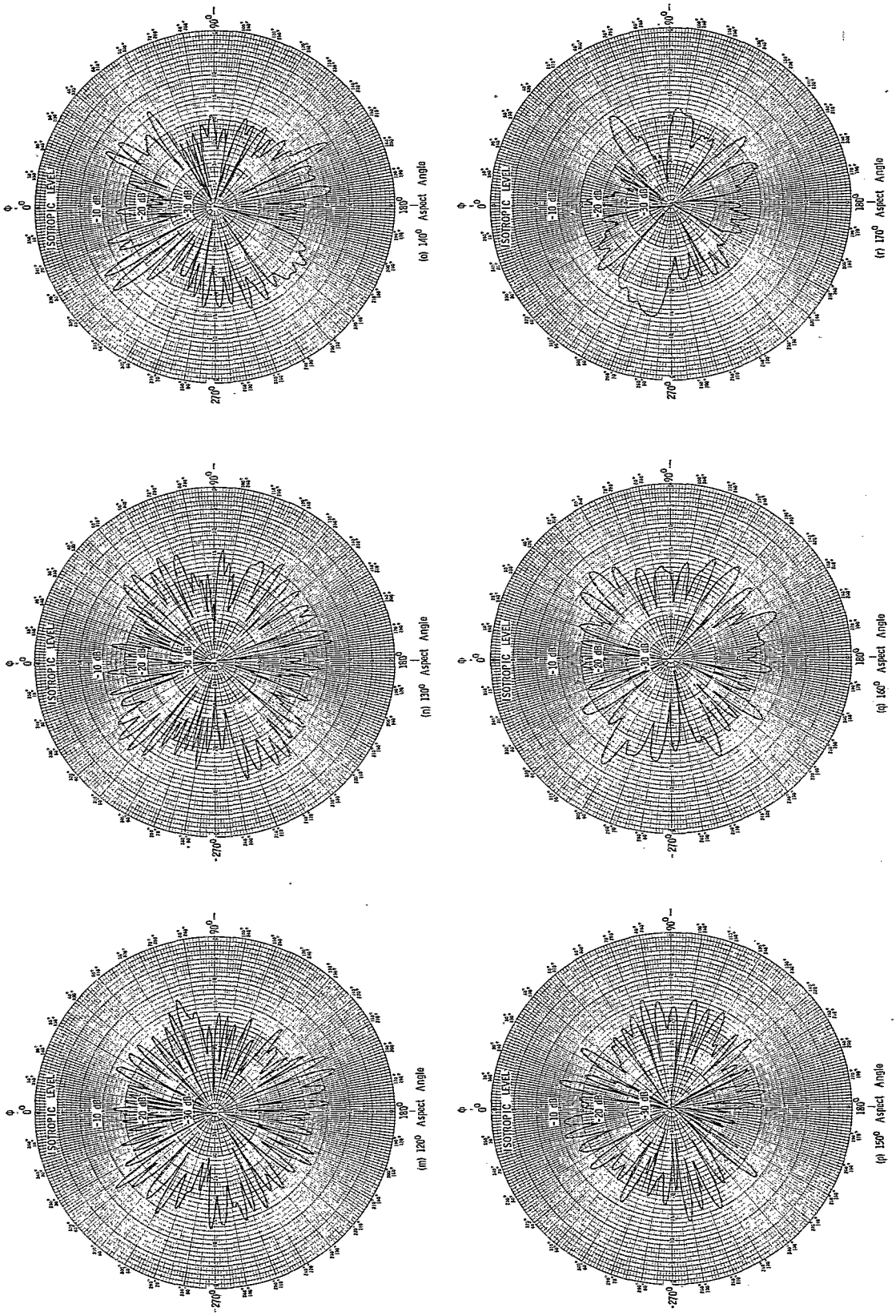

Figure B10.- Concluded.

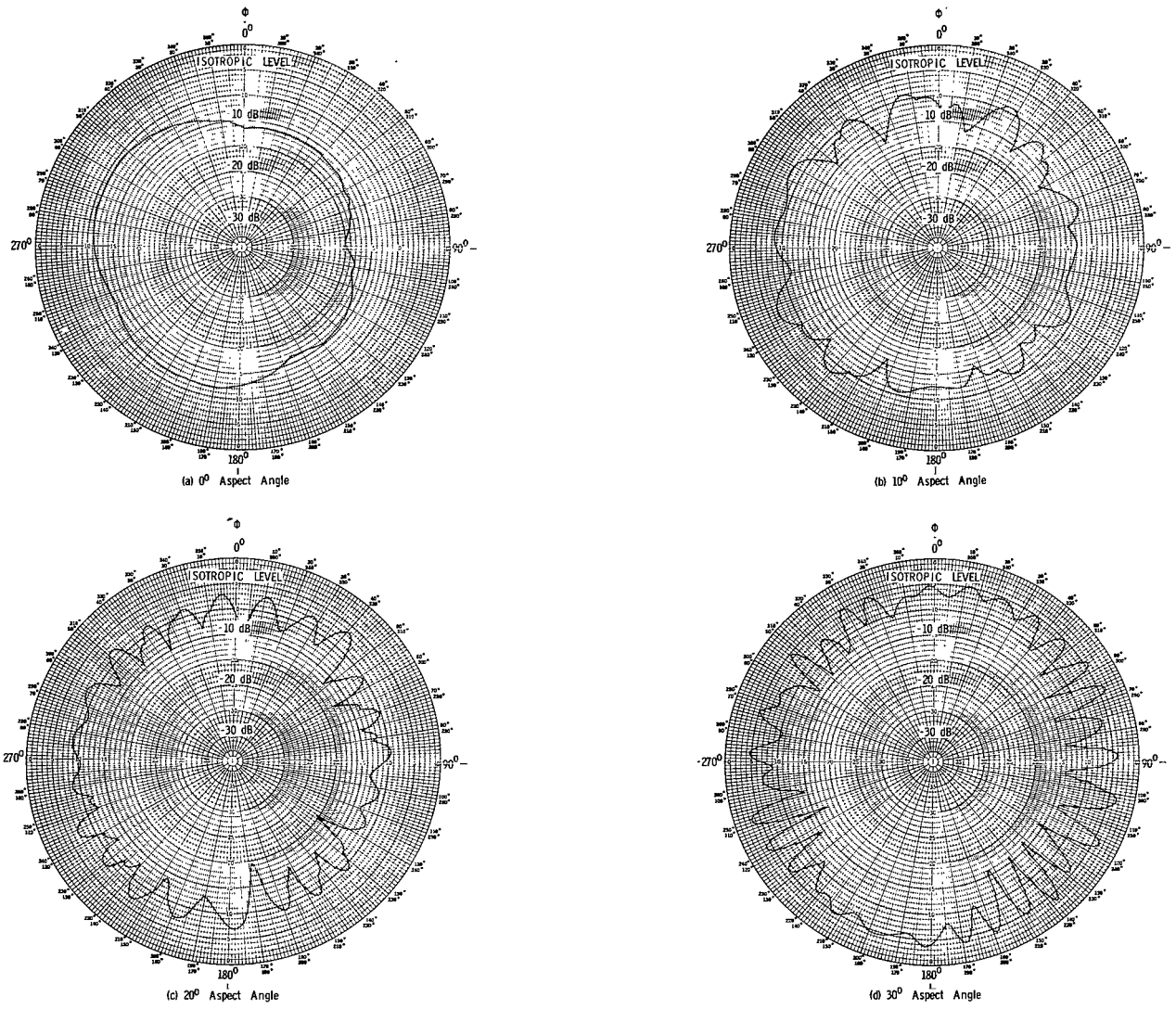

Figure B11.- Sum of dominant and cross-polarized far-field components as a function of roll angle for various aspect angles.

APPENDIX C

INTERPRETATION OF RAM C-I ELECTROSTATIC PROBE DATA

By W. Linwood Jones, Jr.

Introduction

The positive ion current collected by the electrostatic probe is used to measure the free-electron density of the flow-field plasma for altitudes greater than 180 000 ft (54.9 km). In relation to the flowing plasma, each ion collector appears to be a cylindrical wire 0.010 in. (0.0254 cm) in diameter and 0.212 in. (0.5385 cm) long, which is inclined at an angle of 45° with respect to the plasma flow. A classical electrostatic probe theory modified to account for the directed ion flux resulting from the plasma flow is used to calculate the positive ion density. This theory has been experimentally verified to be applicable within a factor of ± 2 for the RAM C-I probe physical configuration at altitudes greater than 150 000 ft (45.7 km). (See ref. 15.)

Theory

In the positive-ion saturation region of the probe voltage-current characteristic, the current is

$$I_+ = f\left(n_+, T_-, v_f, m_+, V, A\right) \tag{C1}$$

where

I_+ collected current

n_+ positive-ion density

T_- electron temperature

v_f flow velocity

m_+ ion mass

V probe potential

A probe area

APPENDIX C

Since there are four unknown variables $(n_+,\ T_-,\ v_f,\ m_+)$ and only one measured quantity (I_+), the quantities T_-, v_f, and m_+ must be determined from theoretical flow-field calculations. The exact functional dependence of n_+ on the other three unknowns is complicated; however, to a first-order approximation

$$n_+ \propto v_f \sqrt{\frac{m_+}{T_-}} \tag{C2}$$

To illustrate the data reduction procedure, a sample calculation is presented.

Sample Calculation

The following factors are given in the sample calculation:

Altitude 250 000 ft (76.2 km)

Ion collector 8

Measured current 50×10^{-6} A

The first factor to be calculated is the probe potential relative to the plasma potential V which is obtained from the following equation:

$$V = \left| V_O - \frac{5kT_-}{e} \right| \tag{C3}$$

where

V_O applied bias, -5 volts

k Boltzmann constant

e electronic charge

The electron temperature is assumed to be equal to the local gas temperature. A plot of gas temperature as a function of altitude for the ion collector locations is shown in figure C1. These temperature data as well as the flow velocity data given in figure C2 were generated by a nonequilibrium, boundary-layer-corrected flow-field analysis of the RAM C-I trajectory. For an altitude of 250 000 ft (76.2 km) and ion collector 8, the electron temperature was calculated to be 3600° K. The probe potential V is therefore 6.551 volts.

The next factor to be determined is the potential-to-kinetic energy ratio for ions η, which is calculated to be

$$\eta = \frac{eV}{kT_-} = 21.12 \tag{C4}$$

The ratio of ion-sheath radius to probe radius γ is estimated by manipulating the space-charge-limited diode equation in terms of the measured current, the probe potential, and the physical dimensions of the probe. The result is shown in figure C3 where $(\gamma - 1)$ is plotted as a function of the parameter Θ, which is defined as

$$\Theta = \frac{L}{r_p} \frac{V^{3/2}}{I_+} \left(1 + \frac{2.66}{\sqrt{\eta}}\right) \tag{C5}$$

where

L probe length, 0.5385 cm

r_p probe radius, 0.0127 cm

For a measured current of 50 μA, the value of Θ is 2.24×10^7. The corresponding sheath-to-probe radius ratio γ is 2.25.

The modified normalized probe current R is now determined. Figure C4 is a plot of R as a function of the modified potential-to-kinetic energy ratio H, which is defined as

$$H = \frac{\eta}{(1 + s^2)} \tag{C6}$$

The ion speed ratio s is

$$s = \frac{v_f \sin \theta}{v_+} \tag{C7}$$

where

v_f flow velocity, 6.35×10^5 cm/sec

θ angle between flow velocity and the cylindrical axis, 45^o

v_+ ion velocity, calculated to be

$$v_+ = \left(\frac{2kT_-}{m_+}\right)^{1/2} = 1.413 \times 10^5 \text{ cm/sec} \tag{C8}$$

for $m_+ = 49.88 \times 10^{-24}$ g (theoretical positive ion concentration 95% NO^+). From equation (C7) $s = 3.180$, and thus the value of H is 1.906. The corresponding value of R is 1.61, determined from the following equation:

$$R = \frac{I_+}{I_r} \frac{1}{(1 + s2)^{1/2}} \tag{C9}$$

where

$I_r = JA$

A probe area, 0.0420 cm^2

J random current density expressed as

$$J = n_+ e \frac{v_+}{2\sqrt{\pi}} \tag{C10}$$

Solving for n_+ and equating n_+ to N_e yields

$$N_e = \frac{2\sqrt{\pi} I_+}{Rev_+ A(1 + s^2)^{1/2}} = 3.40 \times 10^{10} \text{ cm}^{-3} \tag{C11}$$

APPENDIX C

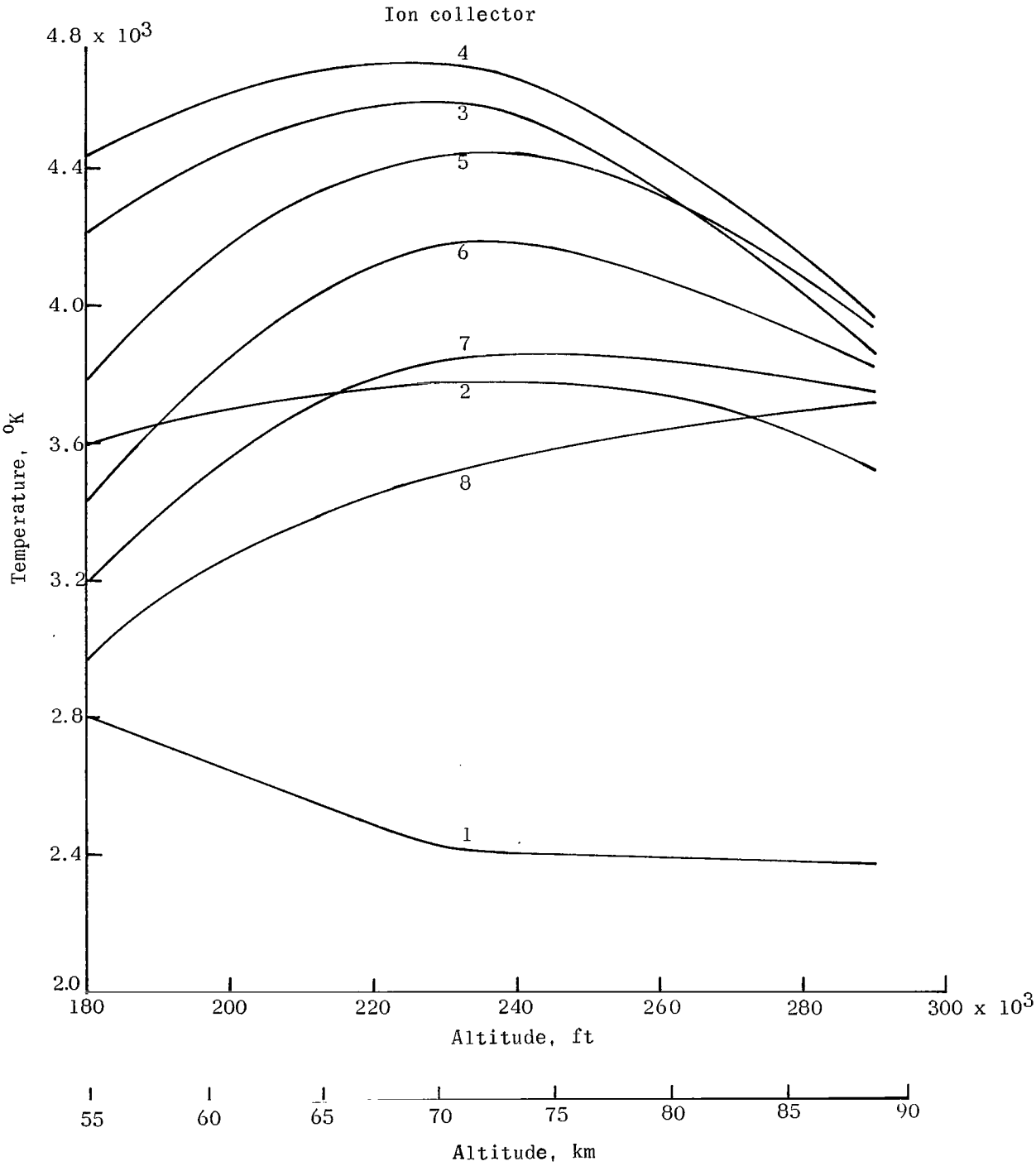

Figure C1.- Computed electron or gas temperature as a function of altitude for electrostatic probe locations.

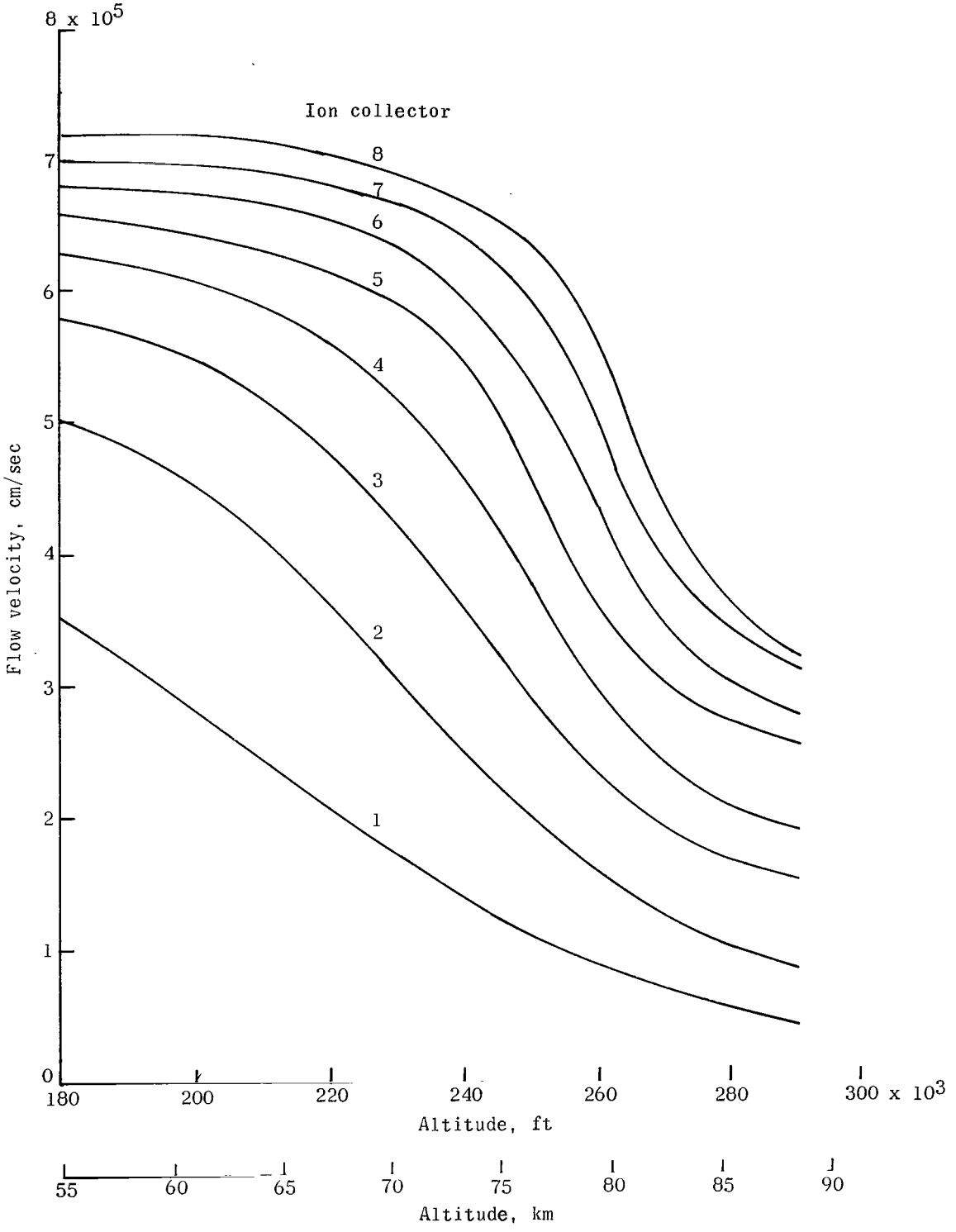

Figure C2.- Computed flow velocity as a function of altitude for electrostatic probe locations.

APPENDIX C

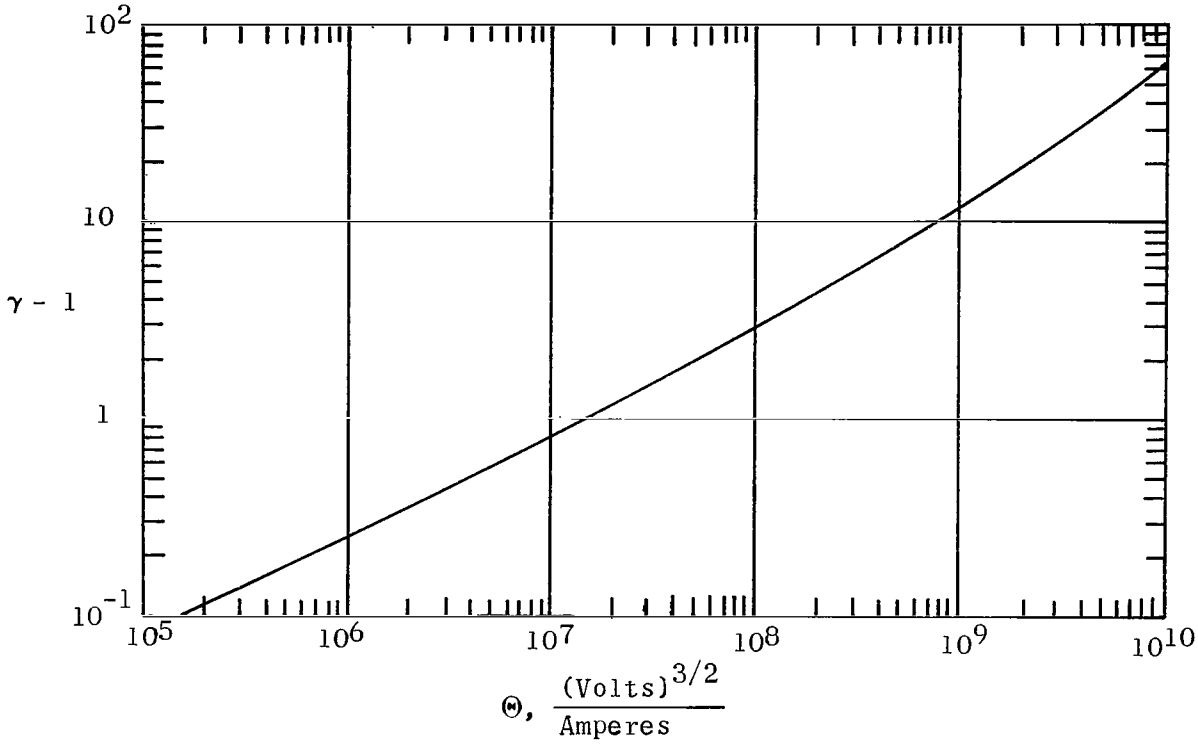

Figure C3.- $(\gamma - 1)$ as a function of Θ.

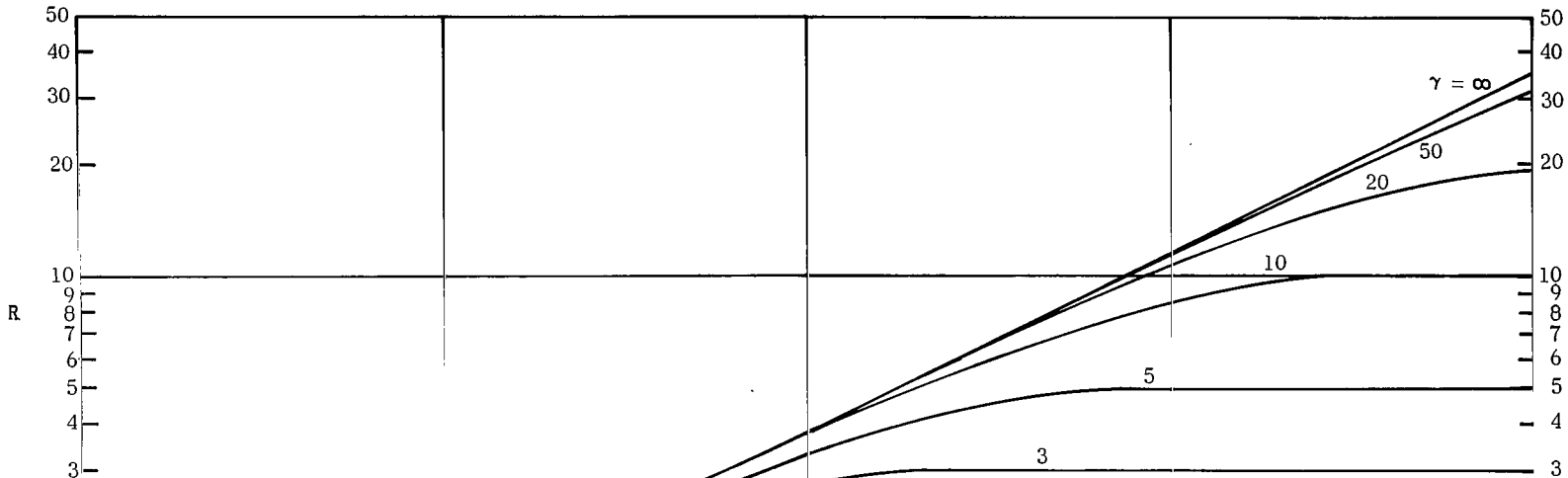

Figure C4.- Normalized probe current R as a function of modified potential-to-kinetic energy ratio H for various values of γ.

REFERENCES

1. Huber, Paul W.; and Sims, Theo E.: The Entry-Communications Problem. Astronaut. Aeronaut., vol. 2, no. 10, Oct. 1964, pp. 30-40.

2. Grantham, William L.: Analysis of Plasma-Sheath Electron Density Measurements at Entry Velocities. NASA paper presented at the Third Symposium on the Plasma Sheath (Boston, Mass.), Sept. 21-23, 1965.

3. Cuddihy, W. F.; and Hughes, J. Kenrick: Simulated Reentry Tests of a Method for Reducing Radio Blackout by Material Addition to Ionized Flow Field. NASA TM X-988, 1964.

4. Huber, Paul W.; and Evans, John S.: Theoretical Shock-Layer Plasma Flow Properties for the Slender Probe and Comparison With the Flight Results. NASA paper presented at Second Symposium on the Plasma Sheath (Boston, Mass.), Apr. 10-22, 1962.

5. Anon.: Proceedings of the NASA Conference on Communicating Through Plasmas of Atmospheric Entry and Rocket Exhaust. NASA SP-52, 1964.

6. McIver, Duncan E., Jr.; Jones, W. Linwood; and Cuddihy, William F.: Effects of External Material Injection on Radio-Signal Transmission Through a Rocket Exhaust. NASA TM X-1049, 1965.

7. Swift, Calvin T.: Radiation Patterns of a Slotted-Cylinder Antenna in the Presence of an Inhomogeneous Lossy Plasma. IEEE, Trans. Antennas Propagation, vol. AP-12, no. 6, Nov. 1964, pp. 728-738.

8. Sims, Theo E.; and Jones, Robert F.: Flight Measurements of VHF Signal Attenuation and Antenna Impedance for the RAM A1 Slender Probe at Velocities Up to 17,800 Feet Per Second. NASA TM X-760, 1963.

9. Sims, Theo E.: Communication Through Reentry Plasma. Conference Record – 1966 Winter Convention on Aerospace & Electronic Systems, Vol. I, IEEE, c.1966, pp. IB-21 – IB-28.

10. Evans, John S.: Charge Recombination on Water Droplets in a Plasma. NASA TM X-1186, 1965.

11. Cuddihy, William F.; Beckwith, Ivan E.; and Schroeder, Lyle C. (With appendix A by Ivan E. Beckwith, Dennis M. Bushnell, and James L. Hunt; appendix B by Ivan E. Beckwith and Sadie P. Livingston; appendix C by Ivan E. Beckwith): Flight Test and Analysis of a Method for Reducing Radio Attenuation During Hypersonic Flight. NASA TM X-1331, 1967.

12. Evans, John S.: Reduction of Free Electron Concentration in a Reentry Plasma by Injection of Liquids. Vol. III of Proceedings of the Third Symposium on the Plasma Sheath – Plasma Electromagnetics of Hypersonic Flight, W. Rotman, H. Moore, R. Papa, and J. Lennon, eds., AFCRL-67-0280 (Vol. III), U.S. Air Force, May 1967, pp. 343-361.

13. Beckwith, Ivan E.; and Huffman, Jarrett K.: Injection and Distribution of Liquids in the Flow Fields of Blunt Shapes at Hypersonic Speeds. NASA TM X-989, 1964.

14. Beckwith, Ivan E.; and Bushnell, Dennis M.: Depletion of Free Electrons by Water Injection Into the Flow Fields of Hypersonic Vehicles. NASA paper presented at Third Symposium on the Plasma Sheath (Boston, Mass.), Sept. 21-23, 1965.

15. Scharfman, W. E.; and Bredfeldt, H. R.: Use of the Langmuir Probe To Determine the Electron Density and Temperature Surrounding Re-Entry Vehicles. NASA CR-66275, 1966.

16. Oseroff, Donald J.; and Pitkethly, John K.: Radio Attenuation Measurements – Series C, Flight A. NASA CR-66726, 1969.

17. Schroeder, Lyle C.; and Russo, Francis P. (With appendix by Francis P. Russo and Aubrey E. Cross): Flight Investigation and Analysis of Alleviation of Communications Blackout by Water Injection During Gemini 3 Reentry. NASA TM X-1521, 1968.

18. Sisco, W.; and Fiskin, J. M.: Shock Ionization Changes EM Propagation Characteristics. Space/Aeronaut., vol. 31, no. 3, Mar. 1959, pp. 66-70.

19. Ellis, Macon C., Jr.; and Huber, Paul W.: Radio Transmission Through the Plasma Sheath Around a Lifting Reentry Vehicle. NASA TN D-507, 1961.

20. Huber, Paul W.; and Nelson, Clifford H.: Plasma Frequency and Radio Attenuation. Proceedings of the NASA-University Conference on the Science and Technology of Space Exploration, Vol. 2, NASA SP-11, 1962, pp. 347-360. (Also available as NASA SP-25.)

21. Spencer, Dwain F.: An Evaluation of the Communication Blackout Problem for a Blunt Mars-Entry Capsule and a Potential Method for the Elimination of Blackout. Tech. Rep. No. 32-594 (Contract No. NAS 7-100), Jet Propulsion Lab., California Inst. Technol., Apr. 15, 1964.

22. French, I. P.; and Bachynski, M. P.: The Radio Spectrum From 10 Gc to 300 Gc in Aerospace Communications. Volume V – Plasma Effects in Aerospace Communications. Res. Rep. No. 6-400-5(7-401-3)(ASD-TR-61-589, Vol. V), RCA Victor Co., Ltd. (Montreal), Mar. 1962.

23. Hodara, H.: The Use of Magnetic Fields in the Elimination of the Re-Entry Radio Blackout. Proc. IRE, vol. 49, no. 12, Dec. 1961, pp. 1825-1830.

24. Langberg, E.; Baldwin, K.; and Yos, J.: Radiation and Propagation of Telemetry Signals During Hypersonic Reentry. IRE Proceedings of the 1958 National Symposium on Telemetering, Section 3.2, Sept. 22-24, 1958, pp. 1-8.

25. Sutton, Kenneth; Zoby, Ernest V.; and Butler, David H.: An Evaluation Test of a Full-Scale Replica of the RAM-CA Flight Heat Shield in a Rocket-Engine Exhaust. NASA TM X-1841, 1969.

26. Kraus, John D.: Antennas. McGraw-Hill Book Co., Inc., 1950.

27. Elliott, Robert S.: Azimuthal Surface Waves On Circular Cylinders. J. Appl. Phys., vol. 26, no. 4, Apr. 1955, pp. 368-376.

28. Collin, Robert E.: Field Theory of Guided Waves. McGraw-Hill Book Co., Inc., 1960.

NATIONAL AERONAUTICS AND SPACE ADMINISTRATION
WASHINGTON, D. C. 20546

OFFICIAL BUSINESS

FIRST CLASS MAIL

POSTAGE AND FEES PAID
NATIONAL AERONAUTICS AN
SPACE ADMINISTRATION

POSTMASTER: If Undeliverable (Section 158 Postal Manual) Do Not Return

"The aeronautical and space activities of the United States shall be conducted so as to contribute . . . to the expansion of human knowledge of phenomena in the atmosphere and space. The Administration shall provide for the widest practicable and appropriate dissemination of information concerning its activities and the results thereof."

— NATIONAL AERONAUTICS AND SPACE ACT OF 1958

NASA SCIENTIFIC AND TECHNICAL PUBLICATIONS

TECHNICAL REPORTS: Scientific and technical information considered important, complete, and a lasting contribution to existing knowledge.

TECHNICAL NOTES: Information less broad in scope but nevertheless of importance as a contribution to existing knowledge.

TECHNICAL MEMORANDUMS: Information receiving limited distribution because of preliminary data, security classification, or other reasons.

CONTRACTOR REPORTS: Scientific and technical information generated under a NASA contract or grant and considered an important contribution to existing knowledge.

TECHNICAL TRANSLATIONS: Information published in a foreign language considered to merit NASA distribution in English.

SPECIAL PUBLICATIONS: Information derived from or of value to NASA activities. Publications include conference proceedings, monographs, data compilations, handbooks, sourcebooks, and special bibliographies.

TECHNOLOGY UTILIZATION PUBLICATIONS: Information on technology used by NASA that may be of particular interest in commercial and other non-aerospace applications. Publications include Tech Briefs, Technology Utilization Reports and Notes, and Technology Surveys.

Details on the availability of these publications may be obtained from:

SCIENTIFIC AND TECHNICAL INFORMATION DIVISION

NATIONAL AERONAUTICS AND SPACE ADMINISTRATION

Washington, D.C. 20546